Hemodynamic simulation of the heart using a 2D model and MR data

Pernille Thorup Adeler

ATV Erhvervsforskerprojekt EF 698

IMM-PHD-2001-86

IMM Math·Tech

ISSN 0909-3192
ISBN 87-88306-13-5

Printed by IMM, DTU
Bookbinder Hans Meyer

Hemodynamic simulation of the heart using a 2D model and MR data.

Pernille Thorup Adeler

August 2001

Preface

This thesis is submitted in partial fulfilment of the requirements for the Ph.D. degree at the Technical University of Denmark (DTU). The project took place as an industrial research Ph.D. project administered by the Danish Academy of Technical Sciences (ATV) and financially supported by the Danish Agency for Trade and Industry in the period August 1st 1997 – August 31st 2001 during which there was a total of 10.5 months leave. It was carried out with the following partners: Math-Tech Aps, Informatics and Mathematical Modelling (IMM) at DTU, and Skejby Sygehus, Århus University Hospital.

Acknowledgements

First of all I would like to thank my supervisors, who all in their various ways have made this project possible. Jacob M. Jacobsen, Roskilde University, has been a wonderful and inspiring supervisor and coworker. I would not have obtained as good a knowledge of the 2D model and its programming code without him. Jesper Larsen, Math-Tech, was the initiator of the project and has always given me very helpful guidance and ideas for further work. Vincent Allan Barker, formerly of IMM has given me very thorough and useful feedback on my written material. Writing the thesis would have been chaotic without his advice. Erik Morre Pedersen, Won Yong Kim and Kim Houlind, Skejby Sygehus, have helped me understand the MR technique and given me useful feedback on the model from a medical point of view. Kim Houlind must also be thanked for his suggestions concerning the investigation of the diastolic function of the ventricle.

I would like to express my special gratitude to Charles S. Peskin and David M. McQueen both of the Courant Institute of Mathematical Sciences, New York University. I am indebted to them for granting me access to the source code of their heart models but even more for the invaluable help, guidance and inspiration they have given me throughout the entire project and particularly during my stay at the Courant Institute in the fall of 1998.

I also want to thank all my colleagues at Math-Tech and IMM for giving me wonderful working environments throughout the past four years.

Finally, I want to give my warmest thanks to my family, especially my husband Ole and our son Magnus, for all their love and support.

Bagsværd, August 2001

Pernille Thorup Adeler

Abstract

Computational models of the blood flow in the heart are a useful tool for studying the functioning of the heart. The purpose of this thesis is to achieve a better understanding of hemodynamics of the normal and diseased hearts through the use of a computational model and magnetic resonance (MR) data.

We present a 2D computational model of the blood flow in the left side of the heart. The work is based on Peskin and McQueen's 2D model dimensioned to data on the dog heart, which we improve and adjust using physiological knowledge and MR velocity data to achieve a model of the human heart. The improvements require changing the geometry, the timing, the mechanical activation of the heart musculature, and the afterload. Furthermore, we introduce a tethering of the otherwise freely floating heart. We evaluate the model from a computational and modelling point of view and find a set of reasonable parameter values. This is our reference model, which gives representative simulation results.

We compare a simulation using our reference model with an MR velocity data set obtained from a healthy human. The comparison is carried out for the intraventricular velocity field and the velocity time curves over the mitral ring and across the aortic outflow tract. The comparison between velocity fields shows a reasonably fair agreement in the general flow pattern: a wide inflow jet, the formation of an anterior vortex during filling, and an outflow jet through the outflow tract. There are some disagreements in the detailed flow pattern, in particular with regard to the vortex patterns. The velocity time curves from the simulation show good agreement with MR data. The timing in the simulation is practically the same as in the MR data, while there are some differences between the shapes and maximum values of the velocity curves.

We use our 2D model to perform investigations of certain mechanisms involved in heart diseases affecting the diastolic functioning of the heart. To be able to simulate pathological conditions we improve the model for the mechanical activation of the heart muscle. We find that it is not possible to successfully

simulate an ischemic apical region by letting the relaxation be slower in the apical region. However, we are able to successfully model a global ischemic left ventricle through a slower relaxation of the entire ventricle and to model a myocardial infarction affecting the apex by letting the apical region be inactive. In both of these cases the simulation results compare well with clinically observed data on dogs and humans.

We present Peskin and McQueen's 3D model of the entire human heart and the nearby great vessels. We perform a simulation with the model, where we adjust the timing to be the same as in our reference 2D model. Unfortunately, the results do not compare very well with MR data. In particular, the flow and velocity over the mitral ring are not in good agreement, and the pressure in the ventricles is far too high. Furthermore, the 3D model is computationally very demanding. This, together with the disagreement with MR data, makes it unfeasible to use the 3D model as a tool for investigating the hemodynamics of the heart. However, the 3D model gives insight into the vortex pattern in the left ventricle. A clear vortex ring is formed below the mitral valve during filling, and in a cut-away view this ring is seen as two distinct vortices, similar to the vortices formed in our 2D model.

Resumé på dansk

Computermodeller af blodstrømningen i hjertet er et nyttigt værktøj til at studere hjertets funktion. Formålet med denne afhandling er at opnå en bedre forståelse for det raske og det syge hjertes hæmodynamik ved at anvende en computermodel og magnetisk resonans (MR) data.

Vi præsenterer en 2D computermodel af blodstrømningen i den venstre side af hjertet. Arbejdet er baseret på Peskin og McQueen's 2D model dimensioneret til data for hundehjertet. Denne model forbedrer og ændrer vi ved brug af fysiologisk viden og MR hastighedsdata for derved at opnå en model af det menneskelige hjerte. Forbedringerne kræver at geometrien, tidsforløbet, den mekaniske aktivering af hjertemuskulaturen og udløbsbetingelserne ændres. Ydermere introducerer vi en fastgørelse af det ellers frit flydende hjerte. Vi evaluerer modellen ud fra et beregnings- og modelleringsmæssigt synspunkt og finder herved et sæt af parameterværdier. Dette er vores referencemodel, der giver repræsentative simuleringsresultater.

Vi sammenligner en simulering med referencemodellen med et MR hastighedsdatasæt fra et rask menneske. Sammenligningen udføres for det intraventrikulære hastighedsfelt og for hastighedskurver over mitralringen og på tværs af udløbstragten ved aorta. Sammenligningen mellem hastighedsfelterne viser en fornuftig overensstemmelse i det generelle flowmønster: en bred indløbsjet, dannelsen af en anterior hvirvel ved fyldning og en udløbsjet gennem udløbstragten ved aorta. Der er dog visse uoverensstemmelser i det detaljerede flowmønster, specielt med hensyn til hvirvelmønstret. Hastighedskurverne fra simuleringen viser god overensstemmelse med MR data. Tidsforløbet i simuleringen er stort set det samme som i MR data, mens der er afvigelser mellem formen på og maximumværdierne af hastighedskurverne.

Vi benytter vores 2D model til at udføre en undersøgelse af bestemte mekanismer, der optræder ved hjertesygdomme, der påvirker den diastoliske funktion af hjertet. For at kunne simulere disse patologiske tilstande forbedrer vi modellen af

den mekaniske aktivering af hjertemuskulaturen. Vi finder, at det ikke er muligt succesfuldt at simulere en iskæmisk apikal region ved at lade den apikale region relaksere langsommere. Til gengæld kan vi med succes simulere en global iskæmisk venstre ventrikel ved at lade hele ventriklen relaksere langsommere, og vi kan simulere et myokardieinfarkt, der rammer apex, ved at lade den apikale region være inaktiv. I begge disse tilfælde er der god overensstemmelse mellem simuleringsresultater og klinisk observerede data fra både hunde og mennesker.

Vi præsenterer Peskin og McQueen's 3D model af hele det menneskelige hjerte og de nærmeste store kar. Vi udfører en simulering med modellen, hvor tidsforløbet er det samme som i vores 2D referencemodel. Desværre er der ikke en god overensstemmelse mellem simuleringsresultater og MR data. Specielt flowet og hastigheden over mitralringen passer ikke godt, og trykket i ventriklerne er alt for højt. Ydermere er 3D modellen meget beregningskrævende. Dette, sammenholdt med den dårlige sammenligning med MR data, gør det umuligt at anvende 3D modellen som et værktøj til undersøgelse af hjertets hæmodynamik. Til gengæld kan 3D modellen give indsigt i hvirvelmønstret i den venstre ventrikel. Der dannes en tydelig hvirvelring under mitralklappen ved fyldning, og i et snit gennem hjertet ses denne ring som to distinkte hvirvler, svarende til de to hvirvler, der dannes i 2D modellen.

Contents

List of Figures

Chapter 1

Introduction

Hemodynamic simulations of the heart based on computational models can be a useful tool for studying the normal and abnormal functioning of the heart. In this approach magnetic resonance imaging (MRI) can be used both as a means for obtaining input parameters and heart boundary conditions to the computational model and for evaluating the simulation results.

The purpose of the work presented in this thesis is to achieve a better understanding of the hemodynamics of the normal and diseased hearts using a computational model and MR measurements. The starting point is the existing two and three dimensional heart models developed by Charles S. Peskin and David M. McQueen.

1.1 Heart simulations

Peskin initiated his work on heart modelling in his Ph.D. thesis (Peskin, 1972a) with a two dimensional (2D) model of the blood flow in the left side of a dog's heart. He introduced a new method for fluid-structure coupling called the immersed boundary method. The idea of the immersed boundary method is that the heart is totally immersed in fluid, i.e. the heart boundary has fluid on both sides and the boundary is represented in terms of the forces it exerts on the fluid. Thus the boundary is simply a specialized region of the fluid where extra forces are applied. The fluid dynamical equations are solved using Chorin's projection method (Chorin, 1968). A drawback of this method is that all lengths and times have to be reduced to achieve numerical stability, with the result that the Reynolds number is reduced to an unphysiological value.

Peskin has developed and studied the 2D model in collaboration with others, in particular David M. McQueen. This work is documented by a series of papers: Peskin (1972b), Peskin (1975), Peskin (1977), Peskin and McQueen (1980), Peskin (1981), McQueen et al. (1982) and Peskin and Printz (1993). These papers, which describe the model of a dog's heart, form the background for our work with the 2D heart model.

Peskin and McQueen's original purpose in creating a heart model was to establish a computer tool for studying the functioning of the mitral valve (Yellin et al., 1981; Meisner et al., 1985) and for designing and investigating prosthetic heart valves for replacement of the natural mitral valve (McQueen and Peskin, 1983; McQueen and Peskin, 1985).

Together with others, Peskin has also studied various alternative numerical schemes for the solution of the flow equations or for the treatment of the coupling of the boundary forces to the fluid (McCracken and Peskin, 1980; Börgers and Peskin, 1987; Tu and Peskin, 1992; Mayo and Peskin, 1993). These alternative methods are not implemented in our version of the computational model.

The computational method of the 2D heart model has since been expanded to 3D (Greenberg et al., 1987; Peskin and McQueen, 1989; McQueen and Peskin, 1989), and the work of Peskin and McQueen has culminated in a 3D model of the entire human heart and nearby great vessels (Peskin, 1989; Peskin and McQueen, 1992; Peskin and McQueen, 1993b; Peskin and McQueen, 1993a; Peskin and McQueen, 1994; Peskin and McQueen, 1995; Peskin and McQueen, 1996; Davis, 1995; McQueen and Peskin, 2000). In the latest work with the 3D model (McQueen and Peskin, 1997; McQueen and Peskin, 2000) the numerical method for solving the fluid dynamical equations has been changed, eliminating the reduction of the Reynolds number. Since the introduction of the full 3D heart model, Peskin and McQueen have stopped work on the 2D model and are completely focused on the 3D model. The 3D model, however, is very demanding with respect to computational power (McQueen and Peskin, 1997). In fact, it would have been too demanding for the project reported in this thesis, and it was decided to use mainly the 2D model.

The immersed boundary method has been studied and used by others. Beyer and LeVeque (1992) studied the accuracy of various numerical approximations to the fluid boundary coupling in a one-dimensional model using the immersed boundary method, and in Beyer (1992) the method was used for a model of the cochlea (inner ear). Stockie and Wetton (1995) presented a stability analysis of the equations for the immersed boundary method.

Lemmon, Yoganathan and coworkers have used the principles of the immersed boundary method to construct their own 3D model of the left side of the heart. In

Vesier and Yoganathan (1992) the method is validated by comparison between the computational results for a model of the flow through a flexible tube and an approximate analytic solution. In Yoganathan et al. (1994) the 3D model of the flow in the left ventricle during part of systole is presented, and some comparisons with experimental results are reported. This model is used in Yoganathan et al. (1995) to study the systolic anterior mitral valve motion syndrome. In all of these papers the group uses the same numerical method as originally used by Peskin and McQueen. As mentioned above, this method is not able to compute at physiological Reynolds numbers. In Lemmon and Yoganathan (1998) the group changed the numerical method to reduce the computational demands of the model and to be able to compute at physiological Reynolds numbers. This was further exploited in Lemmon and Yoganathan (2000b) where a 3D model of the flow through the left heart during diastole was presented and evaluated by comparisons to clinical data. This diastolic 3D model is used in Lemmon and Yoganathan (2000a) to simulate pathological conditions and thereby investigate the diastolic function of the heart.

The immersed boundary method is special in the way it models the interaction between the fluid flow and the tissues of the heart. Another approach is to let the movement of the boundary be given in advance independently of the flow. In this approach only the resulting flow of the fluid has to be computed. The method of predetermined boundary motion was carried out in Georgiadis et al. (1992) for an idealized ventricular geometry in the form of a contracting ellipsoid. In Taylor et al. (1993), Taylor and Yamaguchi (1995b), Taylor and Yamaguchi (1995a) and Taylor et al. (1996) it was done for a 3D geometry constructed using a cast of a dog's heart taken in the diastolic phase with an assumed movement of the ventricular wall. Furthermore, Schoephoerster et al. (1993; 1994) used 2D cine-angiographic images to determine the heart wall boundary in both a healthy and a diseased (coronary artery disease) left ventricle and subsequently computed the flow during systole. They expanded their method to a simple spherical 3D ventricle in Gonzalez and Schoephoerster (1996), where they also investigated the effect of abnormal wall motion on the flow pattern. In Ding and Schoephoerster (1997) they used cine-angiograms to construct a 3D systolic model of the left ventricle assuming circular cross sections.

The method of predetermined boundary motion has also been used in combination with MR scanning data. Jones and Metaxas (1998) used MRI SPAMM to give the heart boundary configuration for a flow model of the left ventricle. MRI SPAMM allows tracking of material points on the heart and gives an accurate representation of the left ventricular motion from end-diastole to end-diastole (Park et al., 1996). Saber et al. (2001) used anatomical data obtained by MR scanning to construct a model of the left ventricle using moving meshes. Their model simulates the blood flow during a full cardiac cycle except for the late diastole.

1.2 MR scanning

The current state of the magnetic resonance (MR) technique allows the determination of 3D velocity fields for the flow in the human heart (e.g. Houlind et al., 1994; Kim et al., 1995; Walker et al., 1996). In Houlind et al. (1994) and Kim et al. (1995) the three components of the blood velocity field in a single slice (the long-axis plane) was obtained in patients with ischemic heart disease and in normal subjects, respectively. From these velocity data they extract velocity time curves at certain positions, e.g. over the mitral ring. Furthermore, Kim et al. (1995) quantified the left ventricle vortex seen during diastole. Walker et al. (1996) measured the three dimensional blood velocity field in multiple slices in the human heart. In all of these three papers qualitative descriptions of the blood flow are also given.

Recently, MR scanning has been used in the assessment of the diastolic functioning of the left ventricle. Houlind et al. (1999) investigated the age-dependent changes in the blood velocity distribution during early filling. Intraventricular flow has been correlated with disease and is of importance to cardiologist as a possible means of diagnosis (Walker et al., 1996).

In Houlind (2001b) the changes in early diastolic blood flow patterns in diseased hearts (e.g. from acute myocardial infarction) are investigated and so are the changes in velocity profiles obtained along transverse lines in the left ventricle at times just prior to and after the occurrence of the peak velocity at the mitral leaflet tips. Examining the peak velocity (the magnitude and the time of occurrence) at such lines gives insight into the diastolic functioning of the heart. Especially the relaxation of the left ventricle (which is reduced during certain heart conditions) influences the diastolic functioning of the heart, and this is reflected in the flow pattern during filling. However, at present not every mechanism responsible for the observed changes in the blood flow pattern is known.

1.3 Using simulations and MR data together

Computational models of the heart are very useful as simulation tools, where the user e.g. can test the natural and pathological functioning of the heart. In a computational model the effects of different parameters can be investigated independently and combined. But for these model to be trustworthy the results have to be validated. The type of MR measurements presented in e.g. Kim et al. (1995) are ideal for validation of models of the blood flow in the heart, since they are measurements of the blood velocity field which is the typical output from a computational model. Naturally, derived quantities, such as velocity time curves, can also be compared between model and MR measurements. Computational models of the blood flow in the heart have not, to our knowledge, previously been validated in detail by comparisons to MR velocity field data.

The possibility of combining MR measurements and computational heart models to obtain a computer tool for studying the functioning of the human heart is the motivation for our work. We start with Peskin and McQueen's 2D heart model of a dog's heart and through the use of MR data and general physiological and anatomical knowledge adjust it to represent a human heart. Then, the model and its simulation results are evaluated and compared with MR data. This 2D human heart model can then be used to study certain mechanisms affecting the diastolic functioning of the heart under pathological conditions.

1.4 Outline of thesis

The thesis is organized as follows:

Chapter 1 This introduction.

Chapter 2 Description of the physiology and anatomy of the heart. The chapter introduces the reader to the necessary physiological background knowledge and terms used in the subsequent chapters.

Chapter 3 Our 2D model of the left side of the human heart is described in both the continuous and the discrete case, and the computational procedure is given. The improvements and changes needed to transform Peskin and McQueen's original 2D model of a dog's heart to that of a human heart are argued for and described.

Chapter 4 Evaluation of the 2D model from Chapter 3. Certain computational and modelling aspects of the model are evaluated and the proper adjustment of model parameters is found.

Chapter 5 Comparison of the 2D model from Chapter 4 with an MR data set of the velocity field in the human heart. The intraventricular velocity field and velocity time curves at the mitral ring and at the aortic outflow tract are compared with corresponding MR data.

Chapter 6 The 2D model from Chapter 4 is used to simulate certain mechanisms of early filling of the left ventricle under pathological conditions. This requires improving the model for the relaxation and contraction of the heart wall. The improved model is then set up to simulate a healthy human, and pathological conditions are simulated by altering the relaxation and contraction of the ventricle.

Chapter 7 Description of Peskin and McQueen's 3D model of the entire heart. The results from a simulation with the model are briefly compared with MR data.

Chapter 8 The conclusions of the thesis are summarized and recommendations for future work are presented.

Appendix A Introduction to the magnetic resonance imaging technique. This appendix provides the reader with background information on how the MR data used in the thesis is obtained.

Chapter 2

Physiology and anatomy of the heart

This chapter provides an introduction to the physiology and anatomy of the heart essential for understanding the subsequent chapters of this thesis. It is partly based on Olufsen et al. (2001), and we use Ganong (1993), Tortora (1999) and Guyton (1991) as references.

The heart is the pump that drives the blood flow in the cardiovascular system by periodic contraction and relaxation of the heart muscles. The cardiovascular system consists of two parts, the systemic and pulmonary circuits, connected via the left and right heart chambers. From the left side of the heart blood is pumped into the systemic circuit through the aorta. The systemic circulation transports and distributes essential substances to the tissues and it removes byproducts of metabolism. In the muscles and tissues oxygen is partially exchanged with carbon dioxide. As a results the blood is partly deoxygenated when it returns to the right side of the heart through two big veins (the superior and inferior vena cava). The right side of the heart pumps the blood into the pulmonary circulation. Here the partly deoxygenated blood is carried to the lung tissues where carbon dioxide is exchanged with oxygen and the blood then returns to the left side of the heart through four pulmonary veins (two from each lung).

2.1 Internal anatomy

The heart consists of four chambers as shown in Figure 2.1. The left ventricle and left atrium constitute the left side of the heart and the right ventricle and right atrium constitute the right side of the heart.

The left and right sides of the heart are separated by a septum. The atria are divided by the interatrial septum and the ventricles are separated by the interventricular septum. The atrioventricular opening connects each atrium to its corresponding ventricle. This opening is surrounded by a ring of fibrosus tissue, the annulus fibrosus. The lower part of the heart is called the apex while the upper broad end of the heart is called the base, see Figure 2.2.

The heart walls consist of muscle tissue denoted the myocardium. The thickness of the myocardium varies over the heart and increases with workload. The atria do less work than the ventricles. Consequently the atrial walls are thinner, approximately 2 mm. The right ventricle is exposed to the pressure of the pulmonary circulation and has a wall thickness of about 5 mm. The greatest wall thickness, about 15 mm, belongs to the left ventricle which ejects blood into the entire systemic circulation.

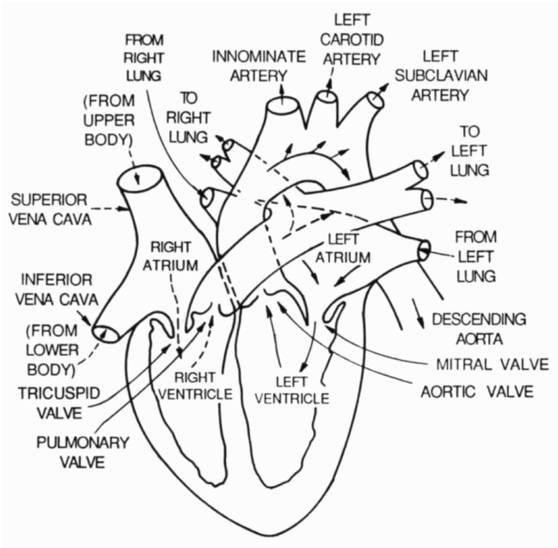

Figure 2.1: The four-chambered heart is divided into two parts, the left and right sides. Both parts consist of a ventricle and an atrium. The left side of the heart is anatomically larger than the right side. From Rideout (1991).

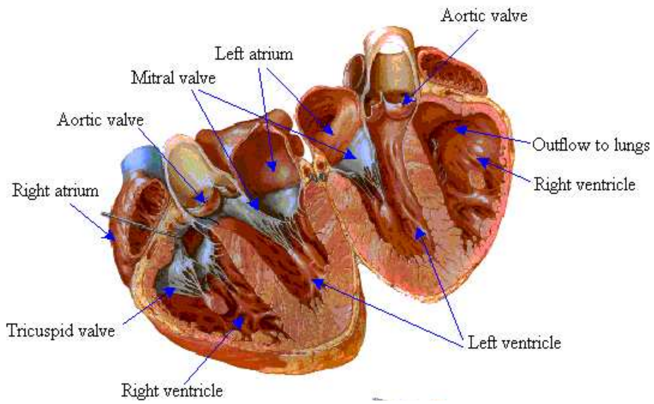

Figure 2.2: Drawing of a heart split perpendicular to the interventricular septum. Adapted from Netter (1991).

The blood flow in the heart is unidirectional due to two sets of valves, the atrioventricular valves and the semilunar valves. The atrioventricular valves are located between each atrium and ventricle. The semilunar valves are found in the opening between each ventricle and its corresponding outflow artery. Valves are not found at the venous inlets into the atria, see Figure 2.2.

The atrioventricular valves consist of leaflets (cusps) with a triangular shape. The right heart chamber contains three leaflets and consequently the valve is denoted the tricuspid valve. The valve in the left chamber contains two leaflets and is thus referred to as the bicuspid valve (or more commonly the mitral valve). Leaflet tendons, also called the chordae tendineae, are found under each valve. They originate from the papillary muscles that are located on the inner surface of each ventricle. When the atrium contracts the leaflets hang slack in the ventricle, but when the ventricle contracts the leaflets are pushed together closing the atrioventricular opening. The chordae tendineae secure the leaflets, preventing them from moving into the atrium during the contraction of the ventricle.

The semilunar valves prevent blood from flowing back into the heart after ejection into the arteries. Each of the semilunar valves consists of three crescent shaped leaflets. These leaflets have no chordae tendineae. They are dilated with blood and close the opening when the pressure in the artery exceeds the pressure in the ventricle. The right semilunar valve is called the pulmonary valve, while the left semilunar valve is called the aortic valve.

2.2 Functioning of the heart

The time course of a heart period can roughly be divided into an active phase and a relaxed phase, termed systole and diastole, respectively. The right and left sides of the heart work almost synchronously, meaning that they contract and relax almost at the same time.

When diastole begins the pulmonary and aortic valves are closed, because the pressure in the arteries exceeds the pressure in the ventricles. The tricuspid and mitral valve are open, and the venous blood flows through the atria and fills the relaxed ventricles.

Then the atria contract (atrial systole) thus increasing the flow to the ventricles and causing the pressure in the ventricles to rise. Shortly after, ventricular systole sets in resulting in a pressure rise that causes the tricuspid and mitral valves to close. Thus the ventricles contract isovolumically. This ends when the ventricular pressure equals the arterial pressure, at which point the pulmonary and aortic valves open and blood flows into the arterial system. The pulmonary and aortic valves do not open at the same time in the two sides of the heart. The pulmonary valve in the right side opens when the pressure in the right ventricle exceeds 10 mmHg and the aortic valve in the left side opens when the pressure in the left ventricle exceeds 80 mmHg. The opening of the pulmonary and aortic valves marks the onset of ejection.

The pulmonary and aortic valves close when ventricular pressure drops below arterial pressure and initiates the next isovolumical relaxation phase and a further fall in ventricular pressure. When the ventricular pressure falls below the atrial pressure, the tricuspid and mitral valves open and the blood that has entered the atrium during ventricular systole flows into the ventricles (this period is called the rapidly filling phase), and a new heart cycle starts.

The amount of blood ejected by each ventricle per stroke is about 70 ml. The ejection fraction (the percentage of the ventricular volume ejected at each stroke) is about 65% (Ganong, 1993). Cardiac output is defined as the amount of blood ejected from the left ventricle into the ascending aorta. In a resting adult this is approximately 5 l/min (70 ml $\times$ 72 beats/min)(Ganong, 1993).

The pumping heart repeats this course during each beat with a time period of approximately 0.8s in resting humans. Figure 2.3 shows ventricular pressure and flow curves that are representative for a normal human left ventricle.

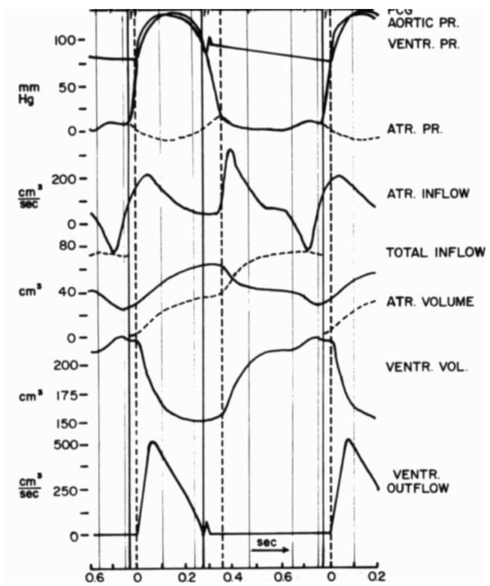

Figure 2.3: The root aortic pressure, ventricular pressure, atrial pressure, arterial inflow, total inflow to the heart, atrial volume, ventricular volume and ventricular outflow. The vertical fully drawn and dashed lines indicate valve closure and openings, respectively. From Noordergraaf (1978).

2.3 Conduction system of the heart

The contraction of the heart is initiated by electrical stimulation. These electrical impulses are spread to all parts of the myocardium by the conduction system. The conduction system consist of the sinoatrial (SA) node, the atrioventricular (AV) node, the atrioventricular bundle (or bundle of His), the bundle branches, and the conducting fibers called Purkinje fibers, see Figure 2.4. All parts of the conduction system are able to send out periodic impulses without neural stimulation. This is called automatism.

The SA node is a small mass of muscular fibers located in the myocardium of the right atrium near the inflow of the superior vena cava, see Figure 2.4. The SA

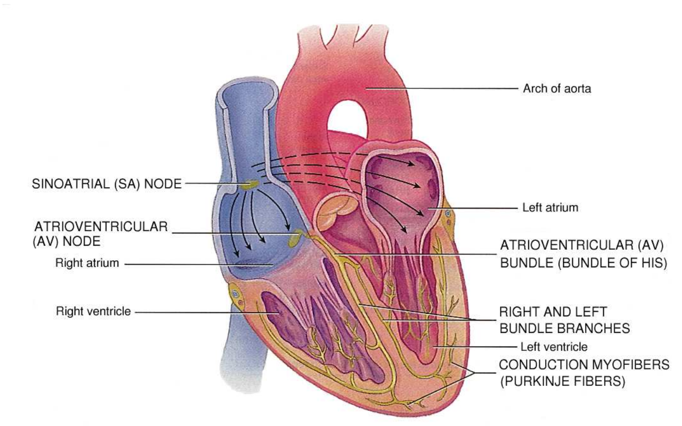

Figure 2.4: Schematic representation of the conduction system of the heart. From Tortora (1999).

node generates impulses faster than the other parts of the conduction system and thus initiates each heartbeat and controls the frequency of the heart rate.

The impulses from the SA node reach the atria first, causing them to contract. The velocity of conduction in the atrial muscle is between 0.3 m/s and 1.0 m/s (Guyton, 1991). Later the impulses reach the AV node. The AV node is located in the interatrial septum, see Figure 2.4. The AV node conducts slowly, i.e. the impulses are delayed (approximately 0.13 s, Guyton, 1991) in the AV node. This allows for the atria to empty their blood (by contraction) into the ventricles before the ventricles start to contract. From the AV node the impulses are sent through the bundle of His. The bundle of His is the only electrical connection between the atria and ventricles. The bundle of His branches into two, one branch going to the right ventricle and the other going to the left ventricle. Both branches go in the direction of the apex of the heart and subdivide into a complex network of Purkinje fibers, see Figure 2.4. The latter stimulates ventricular contraction. The contraction starts at the apex and then spreads superiorly toward the base of the heart. The conduction velocity in the Purkinje fibers is very fast (approximately 1.5–4.0 m/s) and the electrical impulses reach the entire inner surface of the ventricles almost simultaneously. Then the impulses move through the ventricular muscles toward the outer surface of the heart with a velocity of approximately 0.3-0.5 m/s.

2.4 Muscle physiology

The heart pumps by the contraction of its muscle fibers. The heart has a complex geometric structure with muscles lying in a complicated pattern. The cardiac muscle itself consists of individual muscle fibers, or myocytes, which are the smallest functional units in the muscle structure. Each muscle fiber is approximately $40 - 100\mu$m long with a diameter of $10 - 20\mu$m. The muscle fibers branch and interdigitate, but each fiber is a complete unit surrounded by a cell membrane.

Muscle fibers contain a number of fibrils placed in parallel, each of which is subdivided by the Z-lines into blocks called sarcomeres. The sarcomeres show alternating light and dark bands, due to parallel bundles of thick and thin filaments.

The top panel of Figure 2.5 shows a piece of a fibril with its characteristic striated pattern, and a sarcomere going from one Z line to another. At the Z

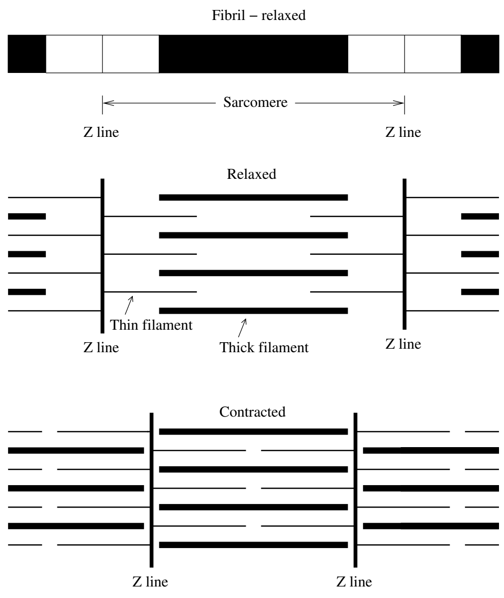

Figure 2.5: Top panel shows a section of a relaxed fibril with its characteristic striped pattern. The striped pattern follows from the bundles of interdigitating thick and thin filament shown in the middle panel. The lower panel shows the contracted state where the Z lines moves closer together.

lines the sarcotubular system is located. It consists of the sarcoplasmic reticulum (which contains a Ca^{2+} reservoir) and the T system. Both of these are essential for contraction of the muscle fibers, see below.

In the middle panel in Figure 2.5 the interdigitating thick and thin filaments are shown when the fiber is in a relaxed state. When a muscle fiber contracts the thin filaments slide over the thick filaments. The length of the thick filaments is constant, whereas the Z lines move closer together when the muscle contracts and farther apart when it is stretched. As the muscle shortens, the thin filaments from the opposite ends of the sarcomere approach each other and eventually overlap. The bottom panel of Figure 2.5 shows the slided thick and thin filaments in a contracted state, where the thin filaments are not yet overlapping.

Contraction of the muscle fibers is initiated by a change in the potential of the cell membrane surrounding the fiber. Cardiac cells respond to an electrical stimulus by producing changes in the ion conductances and in the potential of their membrane. If the stimulus is sufficiently strong an action potential is generated, which in a cardiac muscle is responsible for initiating contraction (Despopoulos and Silbernagl, 1991). Figure 2.6 shows a typical action potential of a cardiac muscle.

Cardiac cells have a resting potential of about -90 mV. A sufficiently strong

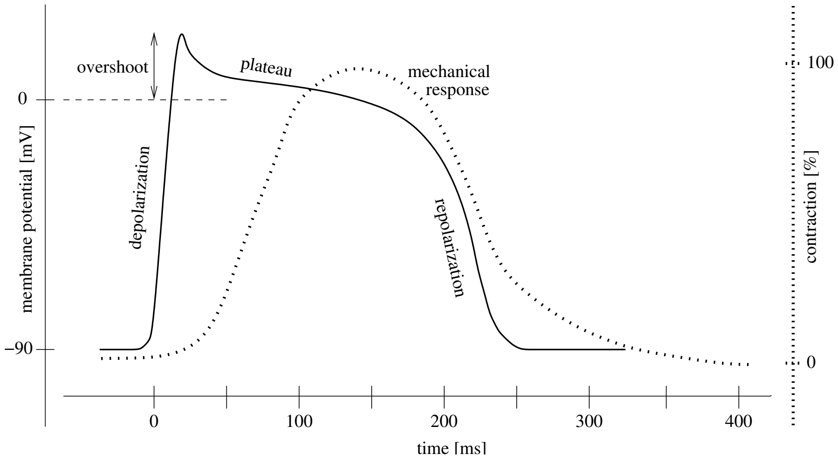

Figure 2.6: Action potential (solid curve) and contractile mechanical response (dotted curve) of a cardiac muscle fiber plotted on same time axis.

stimulus produces an action potential by first reducing the resting membrane potential to a less negative value (depolarization). Depolarization proceeds rapidly and exhibits an overshoot, see Figure 2.6. This is followed by a plateau before the membrane potential returns to the baseline. The depolarization last about 2 ms, but the plateau phase and repolarization last 200 ms or more, see Figure 2.6.

The process by which depolarization of the muscle fiber initiates contraction is called excitation-contraction coupling. The action potential is transmitted to all fibrils in the fiber via the T system and it triggers the release of Ca^{2+} from the sarcoplasmic reticulum. The Ca^{2+} initiates contraction. The contractile response of cardiac muscle begins just after the start of depolarization and lasts about 1.5 times as long as the action potential (Ganong, 1993). Figure 2.6 shows the action potential and the corresponding mechanical response plotted on the same time axis.

Chapter 3

2D heart model using the immersed boundary method

This chapter presents our 2 dimensional (2D) mathematical model of the blood flow in the heart. The original 2D model (Peskin, 1977) was dimensioned to data on the dog heart. In Jacobsen et al. (2001) and Adeler and Jacobsen (2001) the model was adapted to the human heart through the use of MR data, a procedure that required fitting parameters for geometry, timing, muscular contraction and afterload. Here we follow the presentation in Adeler and Jacobsen (2001) and, in addition, introduce modifications regarding tethering and the model of the papillary muscle and chords.

3.1 General description of the model

The model represents a 2D section of the left side of the heart. This section lies in a plane, the long axis plane, which passes through the apex of the heart, bisects the leaflets of the mitral valve and cuts the aortic outflow tract. The model describes the blood flow in and the movement of the left atrium and the left ventricle during a cardiac cycle, including the movement of the mitral valve connecting the two chambers.

The venous inflow to the left heart is modelled by a source placed at the centre of the atrium, and the aortic outflow is allowed through a sink placed at the outflow tract of the ventricle. The model represents the tissues of the heart, both active muscle tissues and passive valve tissues, as infinitely thin, massless elastic boundaries totally immersed in blood, i.e. with blood on both sides. These boundaries then manifest themselves to the fluid by exerting forces on it and are themselves moved by the fluid with the local fluid velocity. The beating of the model heart is induced by successive relaxation and contraction of the elastic boundaries representing the heart muscles.

The model uses a time-stepping procedure of the following type: From a known heart boundary configuration, the boundary forces are updated. On the basis of these forces and the forces in the fluid, the velocity and pressure fields are updated. Finally, the velocity field is used to update the heart boundary configuration.

3.2 Continuous formulation

In this model the heart is immersed in a box filled with a fluid of the same density and viscosity as blood. The heart boundary (muscular wall and valve leaflets) are treated as massless one-dimensional boundaries totally immersed in fluid (blood) and capable of exerting forces on the fluid. The fluid in the cavities confined by the heart boundaries represents blood in the heart chambers, while that outside represents surrounding tissue and mass of heart muscle. The heart model includes a source in the atrium to account for the pulmonary venous inflow and a sink at the aortic outflow tract to allow for ejection of blood during systole. Moreover, since the heart expands during diastole and contracts during systole, the model also includes an exterior sink/source, placed along the vertical boundaries of the domain, to make room for the variation in total heart volume during a heartbeat.

The point of departure for the continuous formulation is the Navier-Stokes equation for incompressible fluid flow and the continuity equation, in which the unknowns are the fluid velocity field $\boldsymbol{u}(\boldsymbol{x}, t)$ and the scalar pressure field $p(\boldsymbol{x}, t)$, with $\boldsymbol{x} = (x, y)$ denoting the position vector and t denoting the time variable:

$$\rho \left(\frac{\partial \boldsymbol{u}}{\partial t} + \boldsymbol{u} \cdot \nabla \boldsymbol{u} \right) = -\nabla p + \mu \nabla^2 \boldsymbol{u} + \boldsymbol{F} \tag{3.1}$$

$$\nabla \cdot \boldsymbol{u} = \psi(\boldsymbol{x}, t) \tag{3.2}$$

The constants ρ and μ denote the fluid density and viscosity, respectively. $\boldsymbol{F}(\boldsymbol{x}, t)$ denotes the force density (force per unit area in 2D) exerted on the fluid by the heart boundary, and $\psi(\boldsymbol{x}, t)$ represents the area flow rate density distribution of the sources and sinks. The force field $\boldsymbol{F}$ is the only representation of the heart boundary's influence on the fluid. The computational domain Ω is taken to be

a square in the model, and the boundary condition is the requirement that the velocity and pressure fields be periodic with this domain as a period.

Equations (3.1) and (3.2) are based on assumptions concerning the momentum of the fluid that enters or leaves the model at the sources and sinks. Fluid leaving the model at sinks takes its momentum with it as it leaves the model, while fluid entering the model at sources has the same velocity (i.e. same momentum) as the fluid at the point where it enters (Jakobsen and Niss, 2000). These assumptions concerning sources and sink will be discussed further in the evaluation of the model (see Section 4.6).

The external fluid force density $\boldsymbol{F}(\boldsymbol{x}, t)$ is a delta-function layer given by

$$\boldsymbol{F}(\boldsymbol{x}, t) = \int_0^L \boldsymbol{f}(s, t)\, \delta(\boldsymbol{x} - \boldsymbol{X}(s, t))\, ds \tag{3.3}$$

where the function $\boldsymbol{X}(s, t)$, $0 \leq s \leq L$, parameterizes the heart boundary (a closed curve) and $\boldsymbol{f}(s, t)$ denotes the boundary force density with respect to s, i.e. $\boldsymbol{f}(s, t)ds$ is the force exerted on the fluid by a piece of the boundary of length ds about s. From this equation it is seen that the force field $\boldsymbol{F}(\boldsymbol{x}, t)$ is zero everywhere except at the heart boundary where it is equal to the force density exerted on the fluid by the heart boundary.

Figure 3.1 shows the computational domain Ω with the initial heart boundary $\boldsymbol{X}(s, t_0)$ drawn. The choice of initial geometry will be discussed in Section 3.3.7. The heart boundary is simulated either as passive tissue following the fluid motion

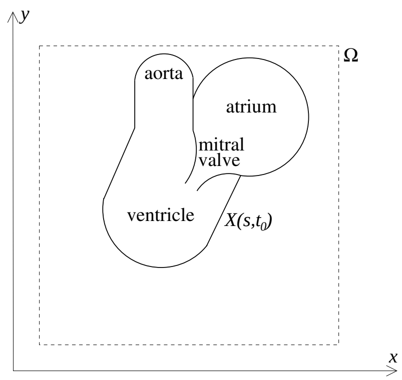

Figure 3.1: Computational domain Ω and initial heart boundary configuration $\boldsymbol{X}(s, t_0)$.

or as active muscle tissue. For the passive elastic parts of the boundary, the boundary force density $\boldsymbol{f}$ depends only on the current configuration $\boldsymbol{X}$, while for the active parts (simulating muscles) it also depends on the history of $\boldsymbol{X}$ through the time development of internal variables (variable resting lengths) which determine the contractile properties of the boundary. The time development of the internal variables is determined from a given function of time, the activation function α (see Sections 3.3.5 and 3.3.6). The specific form of the boundary force density $\boldsymbol{f}(s,t)$ will be specified in the discrete formulation of the model in Section 3.3.5.

The fluid is subject to the no-slip condition at the heart boundary and therefore the boundary moves with the local fluid velocity

$$\frac{\partial \boldsymbol{X}}{\partial t}(s,t) = \boldsymbol{u}(\boldsymbol{X}(s,t),t) = \int_\Omega \boldsymbol{u}(\boldsymbol{x},t)\,\delta(\boldsymbol{x} - \boldsymbol{X}(s,t))\,d\boldsymbol{x} \tag{3.4}$$

The motion of the heart boundary is not known in advance, and thus the above equation constitutes an equation of motion for the heart boundary. The velocity is assumed to be continuous across the boundary as a part of the no-slip condition.

The above equations describe the fluid velocity field (and related quantities) in an Eulerian way, while quantities related to the heart boundary are described in a Lagrangian way. It is seen that the $\delta-$function is used to couple Eulerian quantities with Lagrangian quantities. In equation (3.3) the $\delta-$function spreads the Lagrangian heart boundary force $\boldsymbol{f}$ to the Eulerian force field $\boldsymbol{F}$, while in equation (3.4) the $\delta-$function is used to compute the Lagrangian fluid velocity at the boundary $\boldsymbol{u}(\boldsymbol{X}(s,t),t)$ from the Eulerian fluid velocity field $\boldsymbol{u}(\boldsymbol{x},t)$. This coupling between fluid and boundary is the heart of the immersed boundary method. It allows for the interaction between a fluid and an immersed boundary, without knowing the motion of either in advance. Furthermore, by introducing this coupling it is possible to set up the equations of motion for the fluid (the Navier-Stokes equation 3.1 and the continuity equation 3.2) without distinguishing between Eulerian quantities and Lagrangian heart boundary quantities.

3.2.1 Sources and sinks

Venous inflow to the heart is modelled by a source in the atrium, while outflow during ejection is modelled by a sink at the aortic outflow tract. The heart changes area (defined as the area inside the closed heart boundary) during a heart cycle, and thus it is necessary to include a source/sink outside the heart boundary to accommodate the changes in area during a heart cycle. The source in the atrium and the sink at the aortic outflow are referred to as the interior sources and sinks, while the source/sink outside the heart boundary is referred to as the exterior source/sink.

Density distribution

The sources and sinks are defined as areas where fluid can enter or leave the model. They are incorporated in the model through the density distribution $\psi(\boldsymbol{x},t)$ in the continuity equation (3.2).

The density distribution is zero except in the areas at the sources and sinks. It is assumed to be of the form

$$\psi(\boldsymbol{x},t) = Q_{ex}(t)w_{ex}(\boldsymbol{x} - X_{ex}(t)) + \sum_{k=1}^{2} Q_k(t)w_k(\boldsymbol{x} - X_k(t))$$

where $k = 1$ corresponds to the source in the atrium and $k = 2$ corresponds to the sink in the aortic outflow tract. The index ex refers to the exterior source/sink. Further, $Q_k(t)$ and $Q_{ex}(t)$ denote the area flow rate through the source or sink, positive Q meaning inflow and negative Q meaning outflow. Conversion between area and volume is defined by specifying a 'thickness' of the otherwise 2 dimensional domain Ω. w_k and w_{ex} are weight functions (in dimension per unit area) representing the flow distribution across the sources and sinks (assumed to be time and flow independent), and $X_k(t)$ and $X_{ex}(t)$ denote the current positions of the centre of the sources and sinks (which move with the heart).

The mathematical requirement on w_k and w_{ex} is that they be continuous non-negative functions satisfying

$$\int_\Omega w_k(\boldsymbol{x})\,d\boldsymbol{x} = 1 \quad \text{and} \quad \int_\Omega w_{ex}(\boldsymbol{x})\,d\boldsymbol{x} = 1 \tag{3.5}$$

In the model the interior sources and sinks are defined on a quadratic domain of width a and the weight functions are chosen to be properly scaled 'cosine hat' functions of the form

$$w_k(x,y) = \begin{cases} \frac{1}{a^2}\left(1+\cos\left(\frac{\pi}{a/2}x\right)\right)\left(1+\cos\left(\frac{\pi}{a/2}y\right)\right) & \text{for } (x,y) \in [-\frac{a}{2},\frac{a}{2}]^2 \\ 0 & \text{otherwise} \end{cases}$$

The exterior weight function w_{ex} is defined on a rectangular domain of width a' and a height H equal to the height of the computational domain. w_{ex} is a 'cosine ridge' of the form

$$w_{ex}(x,y) = \begin{cases} \frac{1}{a'H}\left(1+\cos\left(\frac{\pi}{a'/2}x\right)\right) & \text{for } (x,y) \in [-\frac{a'}{2},\frac{a'}{2}] \times [0,H] \\ 0 & \text{otherwise} \end{cases}$$

Since the velocity field is required to be periodic there is no net inflow to the domain Ω through the boundaries, so the incompressibility of the fluid implies that the net inflow through the sources and sinks must also be zero, i.e.

$$0 = \int_{\Omega} \nabla \cdot \boldsymbol{u}\, d\boldsymbol{x} = \int_{\Omega} \psi(\boldsymbol{x}, t)\, d\boldsymbol{x} = Q_{ex}(t) + \sum_{k=1}^{2} Q_k(t)$$

By the above equation we have

$$Q_{ex}(t) = -\sum_{k=1}^{2} Q_k(t)$$

Thus we can write

$$\psi(\boldsymbol{x}, t) = \sum_{k=1}^{2} Q_k(t)\psi_k(\boldsymbol{x}, t) \tag{3.6}$$

where

$$\psi_k(\boldsymbol{x}, t) = w_k(\boldsymbol{x} - X_k(t)) - w_{ex}(\boldsymbol{x} - X_{ex}(t)) \tag{3.7}$$

The flow rate $Q_k(t)$ is assumed to be a function of the space average of the pressure $P_k(t)$ at the source or sink. The pressure can only be determined up to a constant, thus it only makes sense to discuss pressure differences rather than absolute pressure. The reference pressure is chosen to be the space average of the pressure at the exterior sink. The space average of the pressure with respect to the weight function w_k is then defined as follows:

$$\begin{aligned} P_k(t) &= \int_{\Omega} p(\boldsymbol{x}, t) w_k(\boldsymbol{x} - X_k(t))\, d\boldsymbol{x} - \int_{\Omega} p(\boldsymbol{x}, t) w_{ex}(\boldsymbol{x} - X_{ex}(t))\, d\boldsymbol{x} \\ &= \int_{\Omega} p(\boldsymbol{x}, t)\psi_k(\boldsymbol{x}, t)\, d\boldsymbol{x} \\ &= \langle p(t), \psi_k(t) \rangle \end{aligned}$$

For each source and sink a specific relation between $Q_k(t)$ and $P_k(t)$ is given, making the flow depend upon the pressure $Q_k(p(t), t)$. Hence introducing this in equation (3.6) the source/sink term ψ can now be expressed as a time varying function $\Psi(p, t)$ of the time varying pressure field $p(t)$ as follows:

$$\psi(\boldsymbol{x}, t) = \Psi(p(t), t)(\boldsymbol{x}) = \sum_{k=1}^{2} Q_k(p(t), t)\psi_k(\boldsymbol{x}, t) \tag{3.8}$$

Flow and pressure relation for atrial source

The specific relation between $Q_1(t)$ and $P_1(t)$ for the source in the atrium is chosen to be that of a linear resistance model pumping against a constant pressure reservoir. Figure 3.2 shows an electric analogue of a linear resistance model. The governing equation at the atrial source is

$$Q_1(t) = \frac{P_{src} - P_1(t)}{R_{src}} \tag{3.9}$$

where P_{src} denotes the load pressure at the source and R_{src} denotes the resistance against the flow through the source.

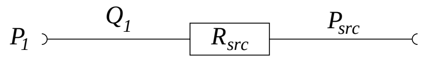

Figure 3.2: An electric analogue to the linear resistance model.

Flow and pressure relation for aortic sink

In the original model developed by Peskin the aortic sink was modelled by a linear resistance model pumping against a constant pressure reservoir combined with a diode-like valve, which opened the sink when the pressure at the sink exceeded a given value for the pressure in the aorta and closed it again when the pressure fell below that value.

We find that the linear resistance model with a constant pressure reservoir for the relation between the outflow rate and the pressure gives a rather unrealistic shape of the associated pressure versus time profile, with the pressure almost clamped at the prescribed constant pressure in the aorta (see Section 4.5). A more realistic curve form is obtained by combining the diode-like sink with a simple three-element Windkessel model of the arterial impedance. The Windkessel model is also a linear resistance model but with a time varying pressure reservoir. See Figure (3.3) for the electric analogue of the Windkessel model.

Let $P_2(t)$ denote the pressure at the aortic outflow tract and $Q_2(t)$ the outflow rate of the ventricle. The inflow to the Windkessel model is then $-Q_2(t)$, and we have

$$-Q_2(t) = \begin{cases} \dfrac{P_2(t) - P_{snk}(t)}{R_{snk1}} & \text{if } P_2(t) \geq P_{snk}(t) \\ 0 & \text{if } P_2(t) < P_{snk}(t) \end{cases} \tag{3.10}$$

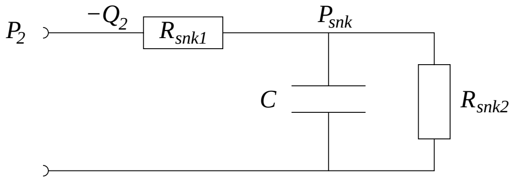

Figure 3.3: Diagram of three-element Windkessel model coupled to diode valve.

where R_{snk1} represents the proximal arterial resistance to the flow and where the pressure $P_{snk}(t)$ may be viewed as the pressure at a representative proximal location in the arterial system. This relation between flow and pressure is similar to the relation for the atrial source (see equation 3.9), except that the load pressure (P_{snk}) for the aortic sink is time dependent.

$P_{snk}(t)$ is governed by the differential equation

$$C\frac{dP_{snk}}{dt} = -Q_2(t) - \frac{P_{snk}(t)}{R_{snk2}} \tag{3.11}$$

where R_{snk2} represents the peripheral resistance and C represents the arterial compliance.

The computation of the boundary forces involves how active and passive tissue is modelled. This is not described on the continuous level but on the discrete level (see Section 3.3.5).

3.3 Discrete formulation

The solution of the continuous model described in the previous section is done by discretizing all quantities and equations of motion and then solving the discrete equations by a time-stepping procedure.

3.3.1 Discrete quantities

We discretize the square domain Ω using a square $N \times N$ grid of points with $h = \Delta x = \Delta y$ denoting the distance between neighbouring points. Time is divided into intervals of length Δt, and the parameter interval for the boundary is divided into subintervals of length Δs. Thus the independent variables are

restricted to the values $\boldsymbol{x} = \boldsymbol{x}_{i,j} = (ih, jh)$, $t = n\Delta t$ and $s = k\Delta s$, where i, j, n and k are integers.

Hence at each time level $t = n\Delta t$ we have the field quantities $\boldsymbol{u}^n$, p^n and $\boldsymbol{F}^n$ defined on the grid points, i.e.,

$$\begin{aligned} \boldsymbol{u}^n_{i,j} &= \boldsymbol{u}(ih, jh, n\Delta t) \\ p^n_{i,j} &= p(ih, jh, n\Delta t) \\ \boldsymbol{F}^n_{i,j} &= \boldsymbol{F}(ih, jh, n\Delta t) \end{aligned}$$

for $i, j = 1, \ldots, N$.

The boundary configuration $\boldsymbol{X}^n$ at time level $n\Delta t$ is defined as a finite sequence of points, not necessarily coinciding with the grid points, with associated boundary force densities. Thus

$$\begin{aligned} \boldsymbol{X}^n_k &= \boldsymbol{X}(k\Delta s, n\Delta t) \\ \boldsymbol{f}^n_k/\Delta s &= \boldsymbol{f}(k\Delta s, n\Delta t) \end{aligned}$$

for $k = 1, \ldots, N_b$, where N_b denotes the number of boundary points in the discretization and where $\boldsymbol{f}^n_k$ denotes a boundary force rather than a force density.

3.3.2 Difference operators and discrete $\delta-$function

The differential equations in the continuous formulation are discretized by replacing the differential operators by difference operators. The centered, forward and backward differences in the x and y directions are used. These are defined for a function ϕ on the domain grid as follows:

$$(D^0_x\phi)_{i,j} = \frac{\phi_{i+1,j} - \phi_{i-1,j}}{2h} \qquad (D^0_y\phi)_{i,j} = \frac{\phi_{i,j+1} - \phi_{i,j-1}}{2h}$$

$$(D^+_x\phi)_{i,j} = \frac{\phi_{i+1,j} - \phi_{i,j}}{h} \qquad (D^+_y\phi)_{i,j} = \frac{\phi_{i,j+1} - \phi_{i,j}}{h}$$

$$(D^-_x\phi)_{i,j} = \frac{\phi_{i,j} - \phi_{i-1,j}}{h} \qquad (D^-_y\phi)_{i,j} = \frac{\phi_{i,j} - \phi_{i,j-1}}{h}$$

In addition to these, a difference operator $\boldsymbol{D} = (D_x, D_y)$ approximating the continuous operator ∇ is needed. This difference operator is obtained through the use of the following approximation δ_h to the δ-function (Peskin and Printz, 1993):

$$\delta_h(\boldsymbol{x}) = \delta_h(x)\,\delta_h(y) \quad \text{for } \boldsymbol{x} = (x, y) \tag{3.12}$$

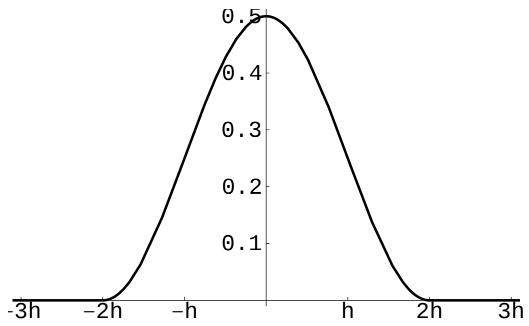

Figure 3.4: Plot of the function $\delta_h(x)$.

where

$$\delta_h(x) = \begin{cases} \dfrac{1}{4h}\left(1+\cos\dfrac{\pi x}{2h}\right) & \text{if } |x| \leq 2h \\ 0 & \text{if } |x| \geq 2h \end{cases} \tag{3.13}$$

Figure 3.4 shows a plot of the δ_h−function.

When the δ_h−function is used the argument is of the form $\boldsymbol{x} - \boldsymbol{X}$, where $\boldsymbol{X}$ is a boundary point that does not necessarily coincide with a grid point.

The virtues of this choice of δ_h−function are given in Peskin (1977). In Peskin and McQueen (1996), Beyer and LeVeque (1992) and Beyer (1992) various alternatives to this choice have been studied.

The vector difference operator $\boldsymbol{D} = (D_x, D_y)$ that approximates the continuous operator ∇ can be defined as follows (see Peskin and Printz (1993) and Thorup (1997)):

$$(D_x\phi)(x,y) = \sum_{x',y'} \phi(x',y')\,\gamma(x-x')\,\omega(y-y') \tag{3.14}$$

$$(D_y\phi)(x,y) = \sum_{x',y'} \phi(x',y')\,\omega(x-x')\,\gamma(y-y') \tag{3.15}$$

with

$$\gamma(x) = \delta_h(x+X)\big|_{X=-h/2}^{X=h/2}, \quad \omega(x) = \int_{-h/2}^{h/2} \delta_h(x+X)dX$$

$$\gamma(y) = \delta_h(y+Y)\big|_{Y=-h/2}^{Y=h/2}, \quad \omega(y) = \int_{-h/2}^{h/2} \delta_h(y+Y)dY$$

The operator works in the following way:

$$\boldsymbol{D}p^n = (D_xp^n, D_yp^n), \quad \boldsymbol{D}\cdot\boldsymbol{u}^n = D_xu_x^n + D_yu_y^n$$

where $\boldsymbol{u}^n = (u_x^n, u_y^n)$.

3.3.3 Discretization of equations of motion

The Navier-Stokes equation (3.1) and the continuity equation (3.2) are discretized following a scheme adapted from A. Chorin (1968; 1969), see Peskin (1972b), Peskin (1972a) and Peskin (1977). This introduces the fractional step velocity fields $\boldsymbol{u}^{n+1.0}$, $\boldsymbol{u}^{n+1.1}$ and $\boldsymbol{u}^{n+1.2}$ found for given $\boldsymbol{u}^n$ and $\boldsymbol{F}^n$ by solving in succession the equations

$$\rho\,\frac{\boldsymbol{u}^{n+1.0}-\boldsymbol{u}^n}{\Delta t} = \boldsymbol{F}^n \tag{3.16}$$

$$\rho\left(\frac{\boldsymbol{u}^{n+1.1}-\boldsymbol{u}^{n+1.0}}{\Delta t} + u_x^nD_x^0\boldsymbol{u}^{n+1.1}\right) = \mu D_x^+D_x^-\boldsymbol{u}^{n+1.1} \tag{3.17}$$

$$\rho\left(\frac{\boldsymbol{u}^{n+1.2}-\boldsymbol{u}^{n+1.1}}{\Delta t} + u_y^nD_y^0\boldsymbol{u}^{n+1.2}\right) = \mu D_y^+D_y^-\boldsymbol{u}^{n+1.2} \tag{3.18}$$

Then $\boldsymbol{u}^{n+1}$ and p^{n+1} are found by solving the system

$$\rho\left(\frac{\boldsymbol{u}^{n+1}-\boldsymbol{u}^{n+1.2}}{\Delta t}\right) + \boldsymbol{D}p^{n+1} = 0 \tag{3.19}$$

$$\boldsymbol{D}\cdot\boldsymbol{u}^{n+1} = \Psi^n(p^{n+1}) \tag{3.20}$$

Here $\boldsymbol{D}$ is the vector difference operator defined above, and $\Psi^n(p^{n+1})$ is obtained from a discretization of equation (3.8),

$$\Psi^n(p^{n+1}) = \sum_{k=1}^{2} Q_k^n(p^{n+1})\psi_k^n \tag{3.21}$$

where ψ_k^n is found by the discretization of equation (3.7)

$$\psi_k^n = w_k(\boldsymbol{X}_k^n) - w_{ex}(\boldsymbol{X}_{ex}^n) \tag{3.22}$$

For the source in the atrium we have according to equation (3.9)

$$Q_1^n(p^{n+1}) = \frac{P_{src}-P_1^n}{R_{src}} = \frac{P_{src}-\langle p^{n+1},\psi_1^n\rangle_h}{R_{src}} \tag{3.23}$$

based on the discrete inner product

$$\langle p, \psi \rangle_h = \sum_{i,j} h^2 \, p_{i,j} \psi_{i,j}$$

where the summation is over the grid points of the domain. We note that the source/sink function ψ is defined and continuous everywhere in Ω, while the pressure p is only defined on the grid points. We also note that the choice of weight functions w_k is such that the discrete analogue of the normalization condition (3.5) holds for all translates of w_k. For the treatment of the aortic sink see Section 3.3.4.

Equation (3.3) for the coupling of the boundary forces to the fluid is discretized using the approximation to the delta function given by (3.12) and (3.13). The discretized version of equation (3.3) then reads

$$\begin{aligned} \boldsymbol{F}^n_{i,j} &= \sum_k \boldsymbol{f}^n(k\Delta s)\, \delta_h(\boldsymbol{x}_{i,j} - \boldsymbol{X}^n(k\Delta s))\Delta s \\ &= \sum_k \boldsymbol{f}^n_k \, \delta_h(\boldsymbol{x}_{i,j} - \boldsymbol{X}^n_k) \end{aligned} \tag{3.24}$$

The calculation of the boundary forces $\boldsymbol{f}^n_k$ is discussed in Section 3.3.5.

Finally, equation (3.4) coupling the fluid motion to the boundary motion is discretized using the same approximation to the delta function, i.e.

$$\begin{aligned} \boldsymbol{X}^{n+1}_k &= \boldsymbol{X}^n_k + \Delta t \boldsymbol{u}^{n+1}_k \\ &= \boldsymbol{X}^n_k + \Delta t \sum_{i,j} \boldsymbol{u}^{n+1}_{i,j} \, \delta_h(\boldsymbol{x}_{i,j} - \boldsymbol{X}^n_k)\, h^2 \end{aligned} \tag{3.25}$$

In solving the discrete equations it is necessary to reduce all lengths and times by a factor γ ($0 < \gamma \leq 1$) to ensure numerical stability. The scaling reduces the Reynolds number, which is equivalent to raising the viscosity of the fluid by a factor of $1/\gamma$. Another effect of the scaling is that the boundary layer of the fluid is raised by a factor of $1/\sqrt{\gamma}$. The scaling is discussed in Section 4.2.

Further details of the solution of the discretized equations of motion can be found in Thorup (1997).

3.3.4 Discrete Windkessel model for the aortic sink

The relation between flow and pressure for the Windkessel model at the aortic outflow is found by discretizing the equations of this model in Section 3.2.1.

Equation (3.11) for the pressure P_{src} is discretized according to an implicit Euler method as follows:

$$\frac{P^n_{snk} - P^{n-1}_{snk}}{\Delta t} = -\frac{Q^n_2}{C} - \frac{P^n_{snk}}{CR_{snk2}}$$

We use $n-1$ and n here, because we need an expression for Q^n_2. This equation may be solved for P^n_{snk}:

$$P^n_{snk} = \frac{P^{n-1}_{snk}}{1 + \Delta t/(CR_{snk2})} - \frac{\Delta t/C}{1 + \Delta t/(CR_{snk2})} Q^n_2 \tag{3.26}$$

Inserting (3.10) into (3.26) and solving for P^n_{snk} we get

$$P^n_{snk} = \begin{cases} \dfrac{P^{n-1}_{snk} + \frac{\Delta t}{R_{snk1}C} P^n_2}{1 + \frac{\Delta t}{RC}} & \text{if } P^n_2 \geq P^n_{snk} \\[2ex] \dfrac{P^{n-1}_{snk}}{1 + \frac{\Delta t}{R_{snk2}C}} & \text{if } P^n_2 < P^n_{snk} \end{cases} \tag{3.27}$$

where $R^{-1} = R^{-1}_{snk1} + R^{-1}_{snk2}$ and $P^n_2 = \langle p^{n+1}, \psi^n_2 \rangle_h$. From relations (3.10) and (3.26) we deduce that

$$P^n_2 \geq P^n_{snk} \qquad \text{if and only if} \qquad P^n_2 \geq \frac{P^{n-1}_{snk}}{1 + \frac{\Delta t}{R_{snk2}C}} \tag{3.28}$$

Inserting (3.27) and (3.28) into (3.10) we obtain the following relation between Q^n_2 and P^n_2 at a given time level n:

$$-Q^n_2 = \begin{cases} \dfrac{P^n_2 - \dfrac{P^{n-1}_{snk}}{1 + \frac{\Delta t}{R_{snk2}C}}}{R_{snk1} \dfrac{1 + \frac{\Delta t}{RC}}{1 + \frac{\Delta t}{R_{snk2}C}}} & \text{if } P^n_2 \geq \dfrac{P^{n-1}_{snk}}{1 + \frac{\Delta t}{R_{snk2}C}} \\[4ex] 0 & \text{if } P^n_2 < \dfrac{P^{n-1}_{snk}}{1 + \frac{\Delta t}{R_{snk2}C}} \end{cases} \tag{3.29}$$

Hence at each time level n for which the valve is open, there is a linear pressure-flow relation between P^n_2 and Q^n_2 (compare with equation (3.23) for the source in the atrium). The apparent resistance to the flow (the denominator in the above expression) is constant in time, but the pressure P_{snk}^n against which the heart is pumping varies with time.

When the values of P_2^n and Q_2^n are computed from the interaction with the heart model then the pressure P_{snk} should be updated according to the following formula

$$P_{snk}^n = \begin{cases} P_2^n + R_{snk1}Q_2^n & \text{if } P_2^n \geq \dfrac{P_{snk}^{n-1}}{1+\frac{\Delta t}{R_{snk2}C}} \\ \dfrac{P_{snk}^{n-1}}{1+\frac{\Delta t}{R_{snk2}C}} & \text{if } P_2^n < \dfrac{P_{snk}^{n-1}}{1+\frac{\Delta t}{R_{snk2}C}} \end{cases} \tag{3.30}$$

The above model for the aortic sink gives rise to the following algorithm for updating the pressure and outflow rate from time level $n-1$ to time level n and for controlling the opening and closing of the valve

1. Compute a preliminary update of P_{snk} according to $P_{snk}^n = \dfrac{P_{snk}^{n-1}}{1+\frac{\Delta t}{R_{snk2}C}}$.
2. Compute the pressure P_2^n from the heart model using relationship (3.29) between pressure and flow in equation (3.21) for the source/sink term Ψ:
   If the valve is open use
   $$-Q_2^n = \frac{P_2^n - P_{snk}^n}{R_{snk1}(1+\Delta t/RC)/(1+\Delta t/R_{snk2}C)}$$
   otherwise
   $$Q_2^n = 0$$
3. If $P_2^n \geq P_{snk}^n$ and the valve is not open, then the valve should be open. Thus open the valve by obtaining the flow Q_2^n through a recomputing of the pressure P_2^n from the heart model using the first of the two pressure-flow relationships in (3.29).
4. If $P_2^n < P_{snk}^n$ and the valve is open, then the valve should be closed. Close the valve by recomputing the pressure P_2^n using the second pressure-flow relationship in (3.29).

5. Compute the correct value of P_{snk}^n according to (3.30):
   If the valve is open then
   $$P_{snk}^n = P_2^n + R_{snk1}Q_2^n$$
   Otherwise no further updating is needed.

The actual choice of Windkessel parameters (C, R_{snk1} and R_{snk2}) are discussed in Section 4.5.

3.3.5 Boundary forces

Now we turn to the description of the boundary forces at the discrete level.

The link formalism

The position of the heart boundary is defined by its configuration vector

$$\boldsymbol{X} = (\boldsymbol{X}_1, \dots, \boldsymbol{X}_{N_b})$$

consisting of the position vectors $\boldsymbol{X}_k$ for the boundary points. The boundary forces are modelled as arising from elastic springs, called links, connecting these boundary points.

The set of all links is denoted I. Let i denote a link connecting boundary point k which has position vector $\boldsymbol{X}_k$ with boundary point l which has position vector $\boldsymbol{X}_l$. Then it is a property of the model that the force $\boldsymbol{f}_k^i$ on the point k due to the link i, at any given time level, is of the form

$$\boldsymbol{f}_k^i = \boldsymbol{f}_k^i(\boldsymbol{X}) = T\left(|\boldsymbol{X}_l - \boldsymbol{X}_k|\right)\frac{\boldsymbol{X}_l - \boldsymbol{X}_k}{|\boldsymbol{X}_l - \boldsymbol{X}_k|} \tag{3.31}$$

where the function T gives the tension in link i versus its length $L = |\boldsymbol{X}_l - \boldsymbol{X}_k|$. Note that superscript i does not denote a time step. The elastic properties of the boundary are thus defined at each time level by a set of length-tension relations $T = T(L)$, one for each link. The model for these length-tension relations is given below.

The total boundary force $\boldsymbol{f}_k^n$ on boundary point k is now given by

$$\boldsymbol{f}_k^n = \boldsymbol{f}_k(\boldsymbol{X}^n) = \sum_{\{i\in I_k\}} \boldsymbol{f}_k^i(\boldsymbol{X}^n) \tag{3.32}$$

where I_k denotes the set of all links which have the boundary point k as one of its end points. More than one link can connect a given pair of points.

However, the boundary forces actually applied to the fluid are not computed directly by evaluating equation (3.32). Instead an implicit method, actually an implicit fractional step method, is used to ensure numerical stability. The forces are not computed from the final boundary configuration $\boldsymbol{X}^{n+1}$ but from a configuration $\boldsymbol{X}^*$ defined implicitly as follows:

$$\boldsymbol{X}_k^* = \boldsymbol{X}_k^n + \Delta t \boldsymbol{u}_k^*$$
$$\boldsymbol{u}_{i,j}^* = \boldsymbol{u}_{i,j}^n + \Delta t \boldsymbol{F}_{i,j}^*$$

where

$$\boldsymbol{u}_k^* = \sum_{i,j} \boldsymbol{u}_{i,j}^* \, \delta_h(\boldsymbol{x}_{i,j} - \boldsymbol{X}_k^n)\, h^2 \tag{3.33}$$

$$\boldsymbol{F}_{i,j}^* = \sum_{k} \boldsymbol{f}_k^* \, \delta_h(\boldsymbol{x}_{i,j} - \boldsymbol{X}_k^n) \tag{3.34}$$

$$\boldsymbol{f}_k^* = \boldsymbol{f}_k(\boldsymbol{X}_1^*, \ldots, \boldsymbol{X}_{N_b}^*)$$

Note that equation (3.33) is of the same form as the last term in equation (3.25) and equation (3.34) is of the same form as equation (3.24).

By substitution in the above five equations we find the following non-linear system (Peskin, 1977; Thorup, 1997)

$$\boldsymbol{X}_k^* = \boldsymbol{X}_k' + \lambda \boldsymbol{f}_k(\boldsymbol{X}_1^*, \ldots, \boldsymbol{X}_{N_b}^*), \quad k = 1, 2, \ldots, N_b \tag{3.35}$$

where $\boldsymbol{X}_k' = \boldsymbol{X}_k^n + \Delta t \boldsymbol{u}_k^n$ (which is known at time level $n+1$) and where λ is chosen so that $\boldsymbol{X}_k^*$ is an approximation to $\boldsymbol{X}_k^{n+1}$. In Peskin (1981) λ is chosen to be $2 \cdot (9/(64h^2))\Delta t^2$. Finally, equation (3.35) can be solved by Newton's method for $\boldsymbol{X}_k^*$ (Peskin and McQueen, 1980; Thorup, 1997), and the forces applied to the fluid are given by $\boldsymbol{f}_k^* = \boldsymbol{f}_k(\boldsymbol{X}_1^*, \ldots, \boldsymbol{X}_{N_b}^*)$, i.e. in equation (3.24) insert $\boldsymbol{f}_k^*$ instead of $\boldsymbol{f}_k^n$.

Passive tissue model

The heart valves and the outflow tract are essentially elastic tissue and these parts of the heart boundary are therefore modelled by linear springs. The length-tension relation in the links modelling the valves is (Peskin, 1977)

$$T(L) = \begin{cases} S_P\,(L - L_0)\,, & L \geq L_0 \\ 0, & L < L_0 \end{cases}$$

where S_P is the stiffness and L_0 is the resting length. It is seen that the tension is never negative, so the element is slack when its length is less than the resting length. This means that the leaflets can resist tension but not compression (McQueen et al., 1982). In Peskin and McQueen (1980) prosthetic heart valves were modelled by changing the length tension relation to allow for resistance to compression.

The tension T^* in a link between the boundary points $\boldsymbol{X}_k^*$ and $\boldsymbol{X}_l^*$ in the boundary configuration $\boldsymbol{X}^*$ is

$$T^* = \begin{cases} S_P\,(L^* - L_0)\,, & L^* \geq L_0 \\ 0, & L^* < L_0 \end{cases} \tag{3.36}$$

where the instantaneous length of the link is $L^* = |\boldsymbol{X}_l^* - \boldsymbol{X}_k^*|$. The resting length L_0 is computed as the length of the link at the initial time.

Muscular model

A link representing a muscular fiber is modelled as two linear springs in parallel, one of which, the active part, has a variable resting length, see Figure 3.5. The variable resting length is modelled by a contractile element in series with the linear spring. This resting length is controlled in a specific way by the length of the link L, its tension T, and a given function of time $\alpha(t)$ modelling the activation level of the muscle. The spring in the active part is denoted the series element. The spring in parallel with the active part, and which constitutes the passive part, is called the parallel element.

The tension T^* in a muscular link in the boundary configuration $\boldsymbol{X}^*$ is the sum of the passive and the active part

$$T^* = T_p^* + T_a^* \tag{3.37}$$

The tension in the passive part is found similarly to the passive tissue model above. Thus

$$T_p^* = \begin{cases} S_{pe}(L^* - L_{pe}^0) & \text{if } L^* \geq L_{pe}^0 \\ 0 & \text{if } L^* < L_{pe}^0 \end{cases} \tag{3.38}$$

where S_{pe} is the stiffness, L^* is the length of the muscular link and L_{pe}^0 is the resting length of the parallel element. S_{pe} and L_{pe}^0 are fixed in time.

The tension in the active part is given by

$$T_a^* = \begin{cases} S_{se}(L^* - L_{ce}^{n+1}) & \text{if } L^* \geq L_{ce}^{n+1} \\ 0 & \text{if } L^* < L_{ce}^{n+1} \end{cases} \tag{3.39}$$

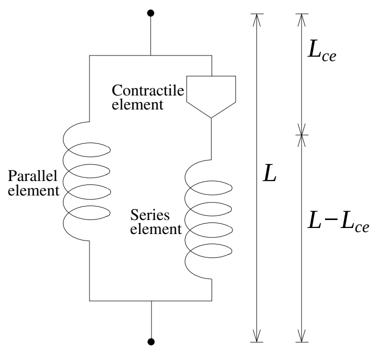

Figure 3.5: Sketch of the muscular model with two linear springs in parallel, one of which is connected in series to a contractile element.

where S_{se} is the stiffness of the series element and L_{ce} is the length of the contractile element. When we compare this expression with the expression for the tension in the passive part above, we see that the length of the contractile element L_{ce} has the function of a resting length. Since L_{ce} varies in time, we can think of the active part as a linear spring with a variable resting length given by L_{ce}.

In the continuous formulation of the model the velocity of contraction of the contractile element is governed by the following combination of a differential equation and an algebraic equation

$$\begin{cases} -\dfrac{dL_{ce}}{dt} = \dfrac{V_{max}}{\alpha(t)} \cdot \dfrac{\alpha(t)S_0L - T_a}{S_0L + T_a} & \text{if } \alpha(t) > 0 \\ L_{ce} = L & \text{if } \alpha(t) = 0 \end{cases} \tag{3.40}$$

where V_{max} and S_0 are muscle parameters and $\alpha(t)$ is a given function of time called the activation function. For details on the activation function see Section 3.3.6.

At constant activation α and length L the equilibrium value of the active tension is $T_a = \alpha S_0 L = S_{se}(L - L_{ce}$, so the maximum value of α compatible with non-negative resting length L_{ce} is $\alpha = S_{se}/S_0$. Characteristic of the model is that the approach to this equilibrium is faster at smaller activation levels due to the α in the denominator in the expression in (3.40).

Equation (3.40), with the activation dependence, is a generalization of Hill's equation for the velocity of contraction of a tetanized muscle. The model above

is known as Hill's three element model, see chapters 9 and 10 of Fung (1993).

In the case of $\alpha^{n+1} > 0$ the tension T_a^* in the link can be found from the system

$$\begin{aligned} T_a^* &= S_{se}(L^* - L_{ce}^{n+1}) \\ L_{ce}^{n+1} &= L_{ce}^n - \Delta t \frac{V_{max}}{\alpha^{n+1}} \frac{\alpha^{n+1} S_0 L^* - T_a^*}{S_0 L^* + T_a^*} \end{aligned}$$

Combining these equations and solving for T_a^* gives

$$T_a^* = \frac{1}{2} S_{se} \left(C - A - B - \sqrt{(A+B+C)^2 - 4AC} \right) \tag{3.41}$$

where

$$\begin{aligned} A &= \Delta t V_{max} \left(\frac{1}{\alpha^{n+1}} + 1 \right) \\ B &= \frac{S_0 L^*}{S_{se}} \\ C &= L^* - L_{ce}^n + \Delta t V_{max} \end{aligned}$$

Since both A and B are positive, it is seen that for $C \le 0$ the tension $T_a^* \le 0$. This corresponds to $L_{ce}^{n+1} \ge L^*$ in which case the tension T_a^* should be zero (see equation (3.39)). Thus we can set $T_a^* = 0$ if $C \le 0$ without having to compute L_{ce}^{n+1} directly.

3.3.6 The activation function

The activation function $\alpha(t)$ which was introduced for the muscular link above is the driving force of the heart model. The activation function models the release of Ca^{2+} (Peskin, 2001), which initiates the contraction of heart muscle as mentioned in Section 2.4. Thus the activation function determines the time course in the model, i.e. the contraction and relaxation of the heart muscle.

We describe here the form of the activation function as it was in the original model by Peskin and McQueen. We have also implemented a new form of the activation function, but this is the topic of Chapter 6 and will not be discussed here.

The time course of the heart cycle is determined by the following parameters: heart rate, onset and duration times of atrial and ventricular systole relative to heart period, and excitation and relaxation rate constants (see below). The model sets the initial time of the simulation in the early ventricular diastole during the isovolumic relaxation phase of the ventricle. The activation function $\alpha(t)$ is defined in separate ways in diastole and systole and is different for the links in the atrium, the ventricle and the papillary muscle.

During diastole the activation function $\alpha(t)$ is defined as a solution to a differential equation of the form

$$\frac{d\alpha}{dt} = -K_r\alpha$$

where K_r denotes a relaxation rate constant. During systole $\alpha(t)$ is defined as a solution to a cascaded set of differential equations of the form

$$\frac{d\alpha_*}{dt} = K_e(\alpha_{max} - \alpha_*), \qquad \frac{d\alpha}{dt} = K_e(\alpha_* - \alpha)$$

where K_e denotes an excitation rate constant and α_{max} denotes the limiting value of the activation function.

The activation function α in systole is chosen as the solution to a second order equation because it gives a smooth transition to the systolic phase, whereas the auxiliary function α_* has a more abrupt upstroke. In addition, the activation function is required to be continuous for the whole heart period. There is a different set of constants for the atrium and the ventricle, but the same set is used for the ventricle and the papillary muscle. The initial values of the activation function are different for all three types of links.

In Peskin and McQueen's original model the constants for the activation function were set to match a dog's heart. Since it is our aim to make a simulation of the model resemble the MR data of a human we change the timing parameters for the activation function. We choose one specific set of MR measurements and use it as the basis for our modification of the model. The length of the heart cycle, 0.936 ms, is found as the peak to peak time (26 intervals of 36 ms duration

	t_s [ms]	$t_{s,end}$ [ms]	K_r [ms^{-1}]	K_e [ms^{-1}]	α_{max}	$\alpha^0 = \alpha(t=0)$
atrium	0.362	0.466	1/55	1/75	1.5	0
ventricle	0.545	0.851	1/55	1/21	4.9	1.07
pap. musc.	0.545	0.851	1/55	1/21	4.9	0.107

Table 3.1: Timings (onset time of systole t_s and end time of systole $t_{s,end}$), rate constants, limiting values, and initial values for the activation functions. Initial time for model is $t = 0$.

each) in the MR recording of the aortic outflow velocity at a central region in the outflow jet at the level of the aortic valve. The MR data does not directly give the timing for the contraction of the heart, but by comparing velocity profiles at the mitral ring and the aortic outflow tract from the simulation and from the MR recording, the constants can be determined by trial and error. These are as listed in Table 3.1. Figure 3.6 shows the activation functions for the ventricle, atrium and papillary muscle for one heart cycle.

The differential equations have analytic solutions (see Section 6.2.1), but in the program the differential equations are solved with sufficient accuracy by an implicit Euler method. In diastole we have

$$\frac{\alpha^{n+1} - \alpha^n}{\Delta t} = -K_r\alpha^{n+1}$$

and in systole

$$\begin{aligned} \frac{\alpha_*^{n+1} - \alpha_*^n}{\Delta t} &= -K_e(\alpha_{max} - \alpha_*^{n+1}) \\ \frac{\alpha^{n+1} - \alpha^n}{\Delta t} &= -K_e(\alpha_*^{n+1} - \alpha^{n+1}) \end{aligned}$$

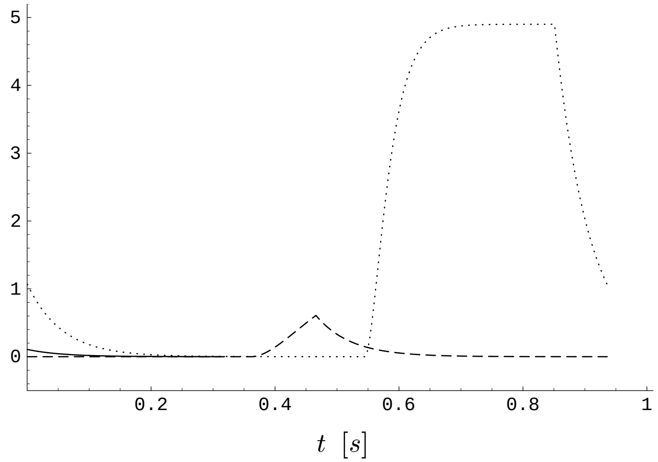

Figure 3.6: Activation as function of time for the ventricle (dotted), atrium (dashed) and papillary muscle (solid), the latter is indistinguishable from the ventricular curve in systole.

3.3.7 Topology and initial geometry of the heart

The geometric parameters determine the size and shape of the model heart at the initial time of simulation. The initial geometry is somewhat idealized, being composed of straight-line segments and circular arcs. This geometry is of course changed during a simulation of a cardiac cycle.

We use four key parameters for the geometry: the diameter of the mitral ring (2.97 cm), the diameter of the aortic outflow tract (2.58 cm), the angle between these two (45°), and the length of the ventricle (5.42 cm). The diameter values are read off from the widths of the inflow and outflow jets in the MR recordings and then increased by 10% so that the widths of the measured and simulated in/outflow jets appear approximately the same during their initial phases. Such increase is necessary in order to compensate for the increased thickness of the boundary layer. The increased thickness is due to the scaling of the viscosity mentioned in Section 3.3.3 and to the size of the region of influence of the boundary layer on the fluid resulting from the chosen spatial resolution. The angular value, which is slightly on the high side, is chosen to make the simulated inflow jet direction fit the measured one at the time of early peak inflow. The length of the ventricle is chosen large enough so that it can withstand contraction until the end of systole. Figure 3.7 shows the final modified initial geometry.

The boundary points are connected by links representing muscles and connective tissues. This link structure, the topology of the model heart, is fixed throughout the cycle. In addition to the so-called physical boundary points, the boundary includes one virtual point which is not moved directly by the fluid but is used as an interconnection point between physical points.

Links connecting the boundary points may be either active or passive, see section 3.3.5. A given pair of points may be connected by more than one link. The boundary points are connected along the wall and in addition by cross links. Cross links are needed to simulate circumferential stresses in the model heart since the model is only 2D. The links themselves do not interfere with the fluid, except through the forces they exert on their end points.

In the original model cross links connect the straight parts of the ventricle to each other. Also connected by cross links are the straight parts of the outflow tract. To accommodate the model to a realistic human left ventricle we increase the stiffness parameters of the cross links in the straight part of the ventricle and introduce cross links in the circular part of the ventricle, see Figure 3.7.

Cross links emanate from a point at the bottom of the ventricle to the virtual point and from the virtual point to the end points of the valve leaflets. The link from the ventricle wall to the virtual point represents the two papillary muscles

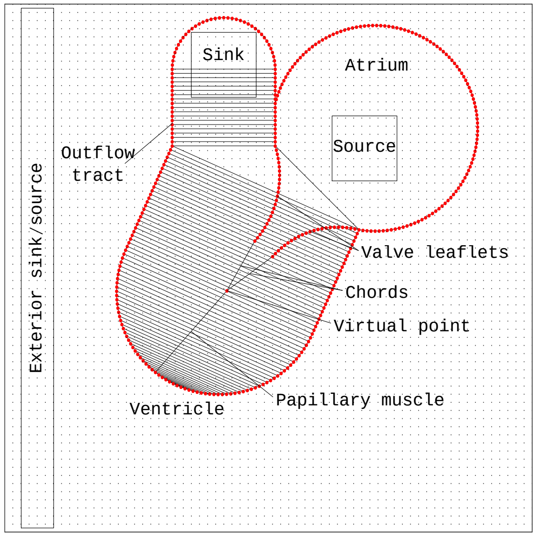

Figure 3.7: Modified initial heart geometry with cross links and links along heart wall shown as full lines.

(see Figure 3.7), which in the real heart protrude from the heart wall at points above and below the plane in which the model resides. They are represented in the model by their common projection onto this plane. In the original model the papillary muscle was connected to the apex of the heart (Peskin, 1977). To improve the movement of the mitral valve we move the point to which the papillary muscle is connected up along the anterior wall. The links from the virtual points to the tips of the leaflet represent the chords, chordae tendineae, which are passive tissue.

All active links are doubled by a corresponding passive link, but some pairs of points are connected only by a passive link, cf. Section 3.3.5 on boundary forces. The links in the outflow tract and the associated cross links are all passive. Also the links in the valve leaflets and the links representing the chords are passive.

In the original model the heart was freely floating in the surrounding domain, which resulted in excessive (non-physiological) movements during the ejection phase. Due to a recoil effect from the ejection the heart would start a rotation changing its alignment in space and begin a translation eventually moving it through the boundary. To overcome this problem we tether the heart by linear springs (passive links) to a set of fixed points. After trying different arrangements we choose to tether the straight part of the outflow tract to fixed points situated at the initial position of the outflow tract. This improves the motion of the heart during a heart cycle considerably, even though it is still more than that of a natural human heart (see Chapter 4).

3.4 Outline of algorithm

The previous sections have described different parts of the 2D heart model. The overall aim of the model is to compute the velocity field $\boldsymbol{u}^{n+1}$, the pressure field p^{n+1} and the heart boundary configuration $\boldsymbol{X}^{n+1}$ at time level $n+1$ based on the same quantities at the previous time level n. The algorithm is as follows:

1. Compute the boundary force $\boldsymbol{f}_k^*$ as follows:

   (a) Compute the fractional step boundary configuration $\boldsymbol{X}^*$ by solving

   $$\boldsymbol{X}_k^* = \boldsymbol{X}_k' + \lambda \boldsymbol{f}_k(\boldsymbol{X}_1^*, \ldots, \boldsymbol{X}_{N_b}^*), \quad k = 1, 2, \ldots, N_b \tag{3.35}$$

   where $\boldsymbol{X}_k' = \boldsymbol{X}_k^n + \Delta t \boldsymbol{u}_k^n$.

   (b) Compute the tension T^* in the boundary based on the configuration $\boldsymbol{X}^*$ as described in Section 3.3.5 for the passive tissue using equation (3.36) and for the muscular tissue using equations (3.37)–(3.41).

   (c) Compute $\boldsymbol{f}_k^*$ using

   $$\boldsymbol{f}_k^* = \boldsymbol{f}_k^*(\boldsymbol{X}^*) = \sum_{\{i \in I_k\}} \boldsymbol{f}_k^i(\boldsymbol{X}^*) \tag{3.32}$$

   where

   $$\boldsymbol{f}_k^i(\boldsymbol{X}^*) = T^*\left(|\boldsymbol{X}_l^* - \boldsymbol{X}_k^*|\right) \frac{\boldsymbol{X}_l^* - \boldsymbol{X}_k^*}{|\boldsymbol{X}_l^* - \boldsymbol{X}_k^*|} \tag{3.31}$$

2. Distribute the boundary force $\boldsymbol{f}_k^*$ to the Eulerian grid, i.e. compute the force field $\boldsymbol{F}^n$ using

   $$\boldsymbol{F}_{i,j}^n = \sum_k \boldsymbol{f}_k^* \, \delta_h(\boldsymbol{x}_{i,j} - \boldsymbol{X}_k^n) \tag{3.24}$$

3. Compute the velocity field $\boldsymbol{u}^{n+1}$ and the pressure field p^{n+1} by solving the Navier-Stokes equation and the continuity equation as follows:

   (a) Successively solve for the fractional step velocities $\boldsymbol{u}^{n+1.0}$, $\boldsymbol{u}^{n+1.1}$ and $\boldsymbol{u}^{n+1.2}$ using

   $$\rho \, \frac{\boldsymbol{u}^{n+1.0} - \boldsymbol{u}^n}{\Delta t} = \boldsymbol{F}^n \tag{3.16}$$

   $$\rho \left(\frac{\boldsymbol{u}^{n+1.1} - \boldsymbol{u}^{n+1.0}}{\Delta t} + u_x^n D_x^0 \boldsymbol{u}^{n+1.1} \right) = \mu D_x^+ D_x^- \boldsymbol{u}^{n+1.1} \tag{3.17}$$

   $$\rho \left(\frac{\boldsymbol{u}^{n+1.2} - \boldsymbol{u}^{n+1.1}}{\Delta t} + u_y^n D_y^0 \boldsymbol{u}^{n+1.2} \right) = \mu D_y^+ D_y^- \boldsymbol{u}^{n+1.2} \tag{3.18}$$

   (b) Solve

   $$\rho \left(\frac{\boldsymbol{u}^{n+1} - \boldsymbol{u}^{n+1.2}}{\Delta t} \right) + \boldsymbol{D} p^{n+1} = 0 \tag{3.19}$$

   $$\boldsymbol{D} \cdot \boldsymbol{u}^{n+1} = \Psi^n(p^{n+1}) \tag{3.20}$$

   for $\boldsymbol{u}^{n+1}$ and p^{n+1} using

   $$\Psi^n(p^{n+1}) = \sum_{k=1}^{2} Q_k^n(p^{n+1}) \psi_k^n \tag{3.21}$$

   $$\psi_k^n = w_k(\boldsymbol{X}_k^n) - w_{ex}(\boldsymbol{X}_{ex}^n) \tag{3.22}$$

   Here $Q_1^n(p^{n+1})$ is given by equation (3.23) for the atrial source, while the computation of Q_2^n for the aortic sink is as described on pp. 30–31 Section 3.3.4.

4. Compute the heart boundary configuration

   $$\boldsymbol{X}_k^{n+1} = \boldsymbol{X}_k^n + \Delta t \sum_{i,j} \boldsymbol{u}_{i,j}^{n+1} \delta_h(\boldsymbol{x}_{i,j} - \boldsymbol{X}_k^n) \, h^2 \tag{3.25}$$

Chapter 4

Evaluation of the 2D model

This chapter presents the evaluation of the 2D heart model. First we present the typical output from a simulation with the model. We evaluate two general aspects of the immersed boundary method (as it is presented in this thesis): the influence of the scaling factor γ and the influence of the periodic boundary conditions. Furthermore, some aspects of the model related specifically to the simulation of the heart are evaluated, e.g. the tethering of the heart, the Windkessel model and the modelling of distributed sources and sinks.

4.1 Simulation output

The main output from a simulation consists of three variables: the heart boundary configuration $\boldsymbol{X}$, the velocity field $\boldsymbol{u}$ and the pressure field p. From each of these several other variables can be derived.

The results presented in this chapter are from a simulation of the model described in Chapter 3, with the following settings: 128×128 grid, 29952 time steps per heart cycle , the length of a heart cycle is 0.936 s, $\gamma = 0.1$, and the total simulation time is 2 heart cycles (i.e. 1.872 s). We will refer to this as our reference simulation. This choice of parameter settings will be discussed in the following sections. In this section we only present the results, leaving the discussion of them to later sections.

4.1.1 Heart boundary configuration and fluid markers

At each time step the heart boundary configuration $\boldsymbol{X}$ is known and can be plotted. We also compute the motion of some fluid markers. These are placed initially at each grid point in the interior of the heart and moved according to the velocity field at each time step. No new markers are introduced as fluid enters the model through the sources, nor are markers removed as fluid leaves through the sinks. The markers do not affect the fluid motion and are only used for output.

An animation of the heart boundary configuration and fluid markers together is a very helpful tool in the investigation of a simulation. Since it is not possible to show this here, we show instead in Figure 4.1 a plot of the heart boundary configuration and the fluid markers at six equidistant times during the second heart cycle.

From the heart boundary configuration the length of the mitral ring and the distance between mitral valve leaflet tips are computed. Furthermore, we compute the area of the atrium and of the ventricle. The time variation of these four quantities can be used in the investigation of a simulation.

4.1.2 Velocity field

The velocity field is visualized through a velocity vector field plot. To simplify the plot, only a subset of the full velocity field is plotted. More precisely, regardless of the spatial discretization used for a simulation, the velocity field is plotted only on a 32×32 grid. In the upper left corner of each velocity field plot a unit size vector corresponding to a length of 1.25 cm and a velocity of 1 m/s is plotted. Furthermore, the heart boundary configuration is plotted. Figure 4.2 shows a plot of the velocity field and the heart boundary configuration at the same six equidistant times as in Figure 4.1. Even though velocity vectors are seen to cross the heart boundary, this does not mean that fluid is leaking through the walls. Rather, this is a consequence of the heart boundary moving with the fluid velocity.

From the velocity field we can compute velocity time profiles at given positions; this is the time variation of the velocity over a given line segment or at a given point. We have focused on velocity time profiles at the mitral ring, between the mitral leaflet tips, and across the aortic outflow tract below the aortic sink.

We compute the mean velocity time profiles as the mean velocity (with respect to space) over a line segment relative to the heart boundary, i.e. in a reference frame moving with the heart. E.g. the velocity time profile over the mitral ring is the spatial mean velocity over the mitral ring relative to the moving mitral ring. Furthermore, we look at the velocity time profile of the centre velocity, which is simply the velocity component normal to the line segment at the centre point of

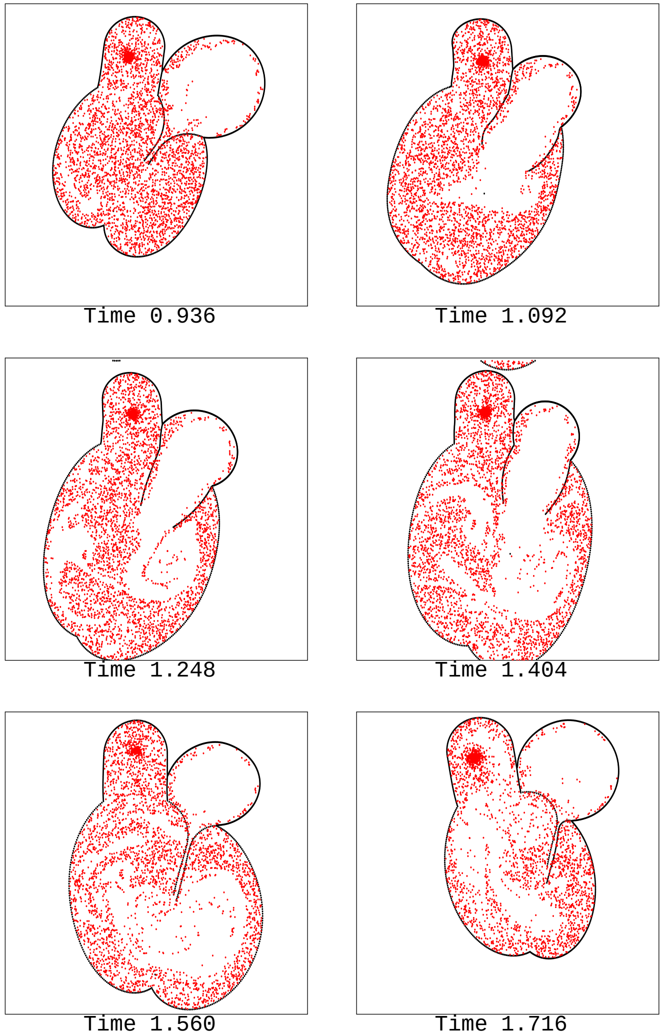

Figure 4.1: Heart boundary and fluid markers at six equidistant times during the second heart cycle. The first time (0.936 s) is at the onset of the second heart cycle in early diastole, while the last time (1.716 s) is at the end of the second heart cycle during ventricular systole.

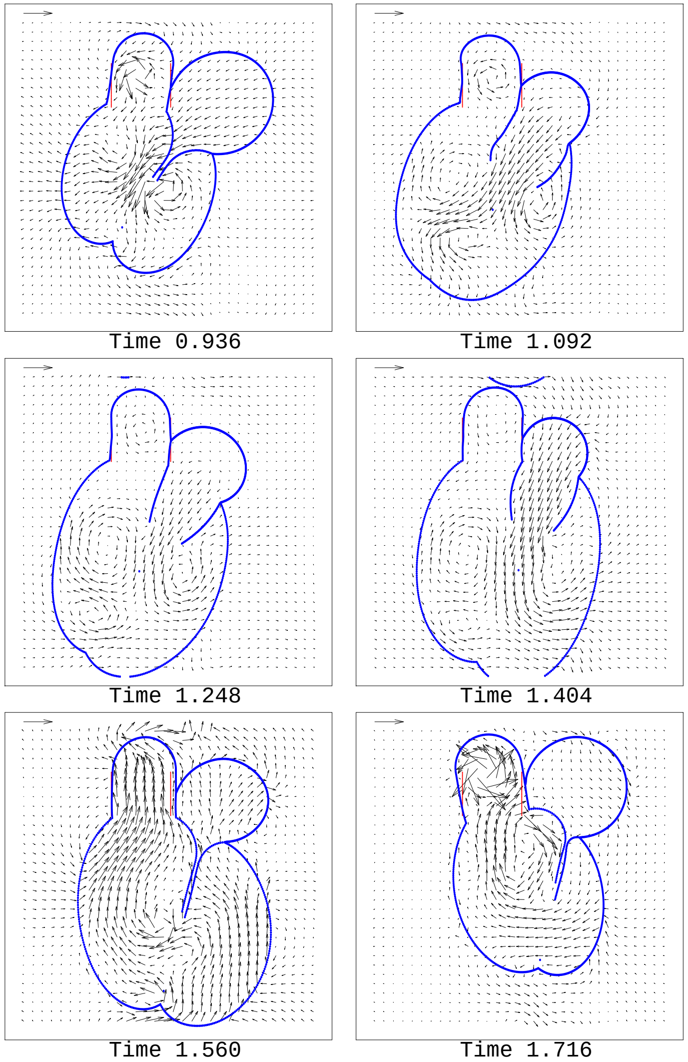

Figure 4.2: Velocity field and heart boundary configuration at six equidistant times during the second heart cycle. The first time (0.936 s) is at the onset of the second heart cycle in early diastole, while the last time (1.716 s) is at the end of the second heart cycle during ventricular systole.

the line segment. The centre velocity is reported as the velocity relative to the computational grid, i.e. in a reference frame fixed in space. In all the plots of velocity time profiles we draw vertical dashed lines at the end time of each heart cycle, i.e. in our reference simulation the lines are drawn at $t = 0.936$ s and at $t = 1.872$ s.

Figure 4.3 shows the velocity time profile of the mean velocity over the mitral ring and between the mitral leaflet tips during 2 heart cycles. Figure 4.4 shows the velocity time profile of the mean velocity across the aortic outflow tract (below the aortic sink) during 2 heart cycles.

From the velocity field we can also obtain flow data over a given line segment. Flow is computed by the mean velocity over the line segment multiplied by the length of the line segment. This gives a flow in the dimension of area per time, which is the natural dimension of flow in a 2D model. To convert area flow to volume flow we multiply by a uniform thickness corresponding to 1/4 of the computational domain. We compute the time variation of the volume flow over the mitral ring, between the leaflet tips, and across the aortic outflow tract (below the aortic sink).

The model naturally gives the volume flow through the sources and sinks in the model, see e.g. equation (3.9) for the flow through the atrial source. The time variation of the flow through the atrial source and the aortic sink are plotted in

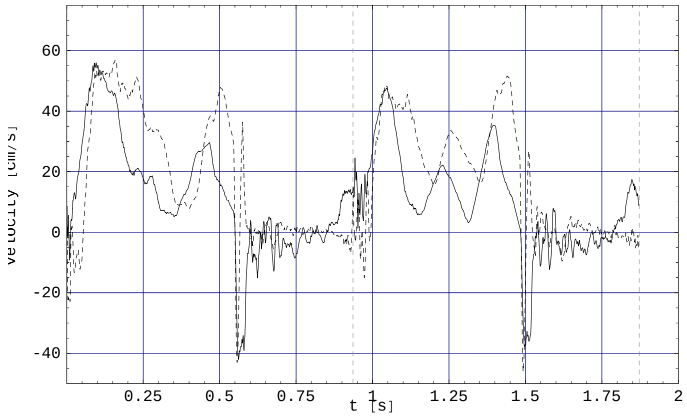

Figure 4.3: Velocity time profile of the mean velocity (cm/s) over the mitral ring (solid) and between the leaflet tips (dashed).

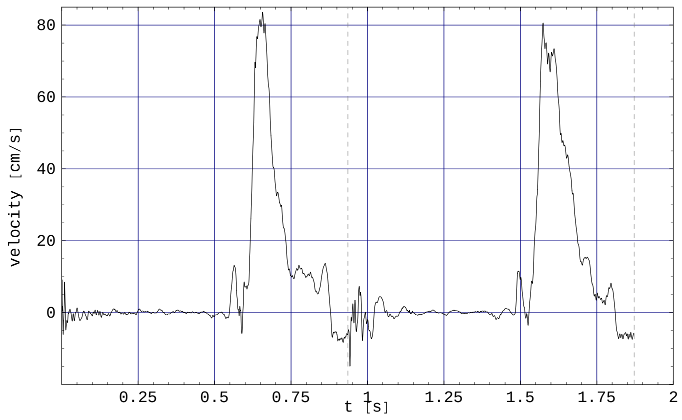

Figure 4.4: Velocity time profile of the mean velocity (cm/s) across the aortic outflow tract (below the aortic sink).

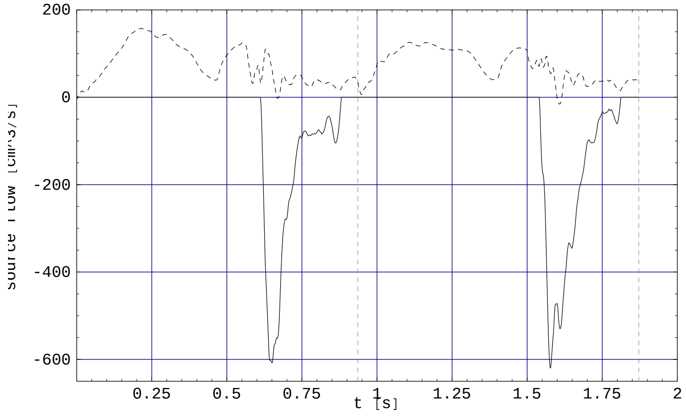

Figure 4.5: Flow time profile for the flow (cm^3/s) through the mitral source (dashed) and the aortic sink (solid).

Figure 4.5. In the figure vertical dashed lines at the end time of each heart cycle are also included.

4.1.3 Pressure field

The model gives the pressure field $p(\boldsymbol{x})$ as output, and this can be plotted as a surface plot, a contour plot, or a density plot, where the colour of a cell corresponds to the value of the pressure field at in that cell. The pressure field is not smooth due to the numerical methods used (Peskin, 2001). Thus an averaging procedure is necessary before it can be plotted. The non-smooth pressure field does not affect the computation of the velocity field, since only the gradient of the pressure field is used in the computations and this is smooth.

Plots of the pressure field is not very useful, since the pressure field inside the heart is rarely known. It is more useful to compute the time variation of the pressure at a given position, e.g. over a small square in the atrium or the ventricle, similarly to the computation of the pressure at a source as described in Section 3.2.1.

Figure 4.6 depicts the time variation of the pressure at a square in the ventricle, in the atrium, and at the aortic sink. The pressure at the aortic sink corresponds to $P_2(t)$ in equation (3.10). In the figure vertical dashed lines are drawn at the end

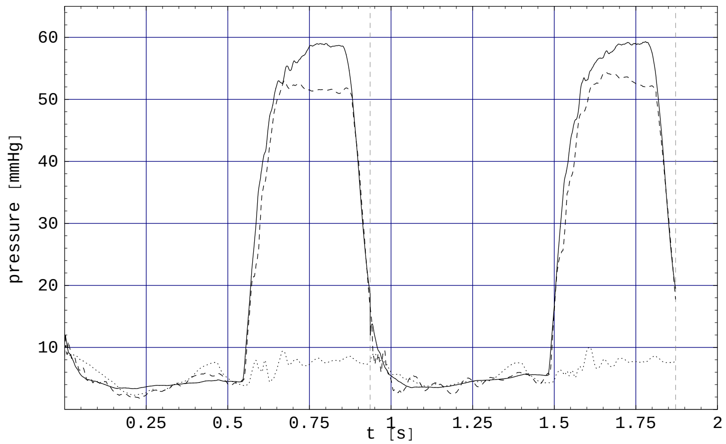

Figure 4.6: Pressure time profile for the pressure (mmHg) in the ventricle (solid), atrium (dotted) and at the aortic sink (dashed).

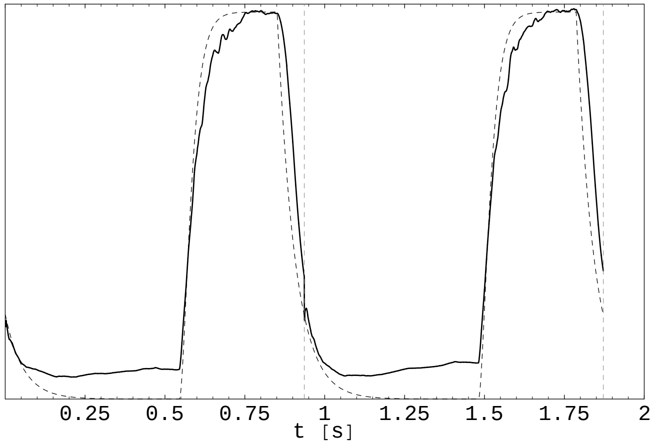

Figure 4.7: Time variation of ventricular pressure (solid) and ventricular activation (dashed) shown on same time axis and scaled to achieve the same maximum level.

time of each heart cycle.

The ventricular pressure variation follows closely the ventricular activation curve. This is illustrated in Figure 4.7 where both the time variation of the ventricular pressure and the ventricular activation are shown on the same time axis and scaled to achieve the same maximum level. We exploit this feature in Chapter 6.

4.2 The scaling factor γ

The scaling factor γ is used to scale all times and lengths to achieve numerical stability of the fluid solver at a reasonable computational time. Peskin introduced the scaling factor γ in his original 2D model (Peskin, 1972a). He later changed the fluid solver in a subsequent 3D model and thus removed the need for scaling (Lai and Peskin, 2000; McQueen and Peskin, 2000). But since the 2D model still uses the old fluid solver, the need for γ is still present, and it is important to investigate the influence of γ on the simulation results.

We believe that the scaling with γ does have an influence on the flow, since scaling all lengths and times by γ $(0 < \gamma \leq 1)$ corresponds to scaling the viscosity

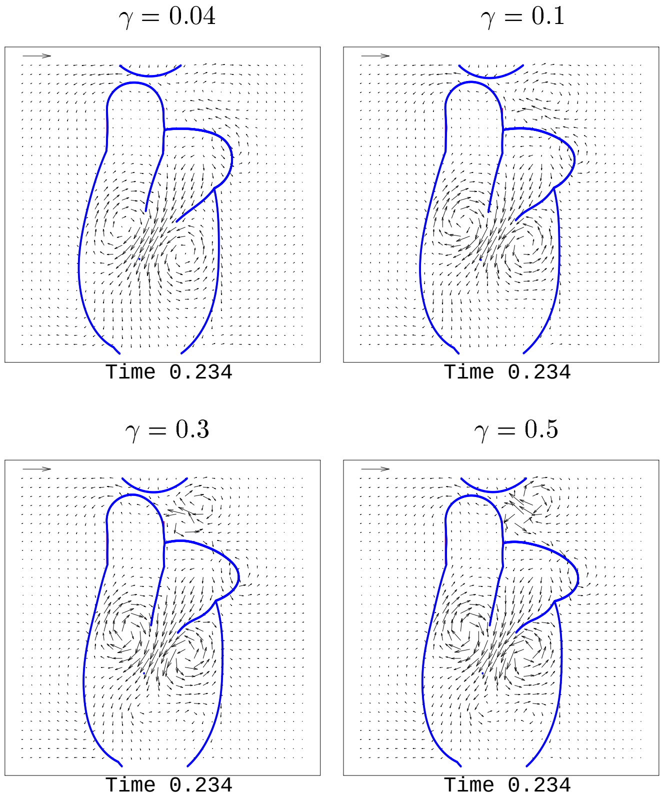

Figure 4.8: Velocity field and heart boundary at $t = 0.234$ s, with $\gamma = 0.04$, 0.1, 0.3 and 0.5.

with $1/\gamma$, thus effectively lowering the Reynolds number. Peskin (1977) justified the introduction of γ by the comparative physiology of the heart of different mammals: hearts of different mammals are roughly scaled models of each other. This is the argument for Peskin's hypothesis that essential features of the blood flow in the heart are not very sensitive to the Reynolds number (Peskin, 1977).

To investigate the influence of γ we make 6 simulations varying only the value of γ. The simulations are performed on a 256 grid with 29952 time steps per heart cycle and a total computation time of 1 heart cycle. The γ values are: 0.04, 0.1, 0.2, 0.3, 0.4 and 0.5. $\gamma = 0.04$ was the original value in the code we received

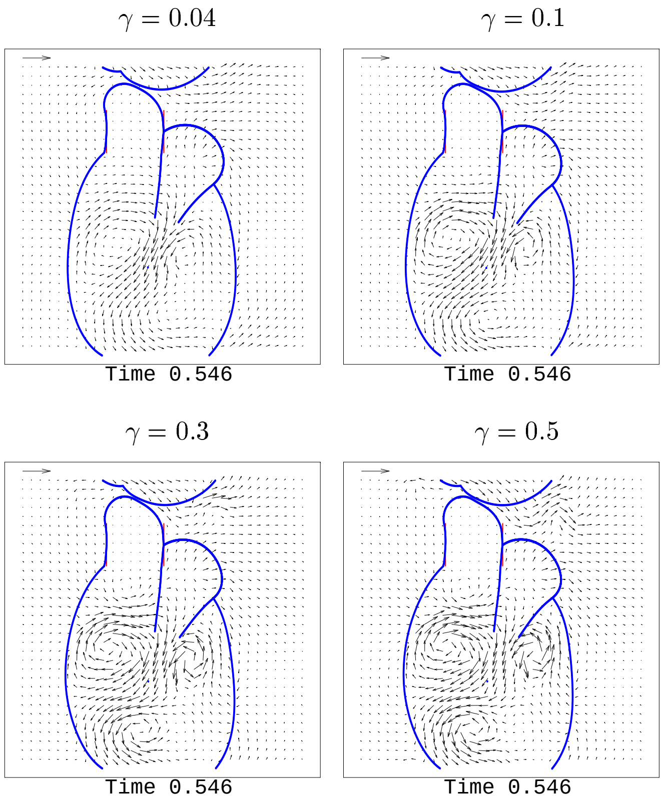

Figure 4.9: Velocity field and heart boundary at $t = 0.546$ s, with $\gamma = 0.04$, 0.1, 0.3 and 0.5.

from Peskin.

To compute at γ values closer to 1 it is necessary to compute on a finer grid. Unfortunately, we could not compute a full heart cycle with $\gamma = 1$. On a 512 grid we can compute approximately 2/3 of a heart cycle. We believe that a $\gamma = 1$ simulation can be accomplished only on a 1064 grid, and unfortunately we did not have sufficient time for this. It is our experience that it is not possible to compute a full heart cycle on a 256 grid with a γ value higher than 0.5. Note though, that it is not possible to complete 2 heart cycles on a 256 grid.

We plot the velocity field from the 6 simulations to compare the overall picture

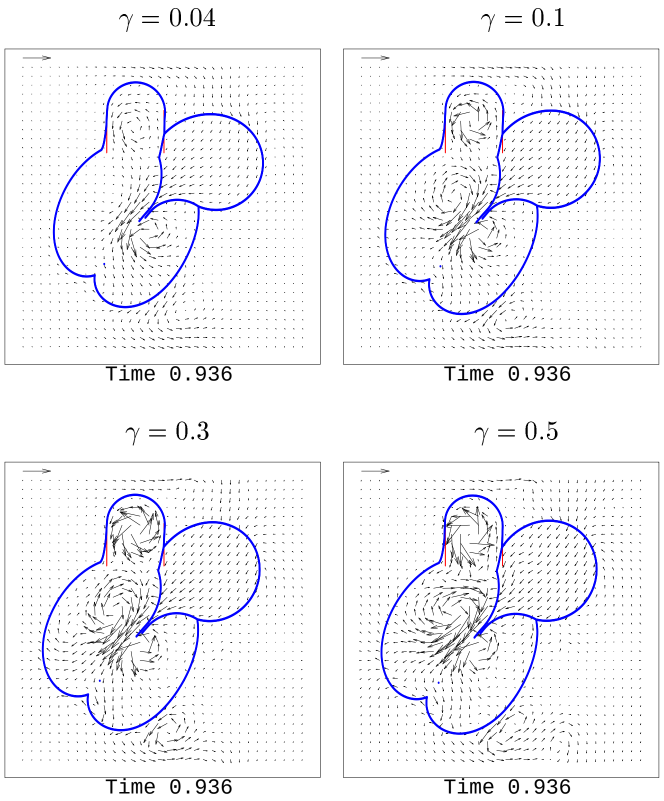

Figure 4.10: Velocity field and heart boundary at $t = 0.936$ s, with $\gamma = 0.04$, 0.1, 0.3 and 0.5.

of the velocity field. Figures 4.8–4.10 show the velocity field at $t = 0.234$ s, $t = 0.546$ s and $t = 0.926$ s, respectively. Each figure contains plots from the simulations with $\gamma = 0.04$, 0.1, 0.3 and 0.5.

The flow in Figure 4.8 occurs during the filling of the ventricle, and it is seen that the flow pattern is generally the same, though the vortices become more distinct as γ increases. The heart boundary configuration is practically the same at all 4 γ values. The flow in Figure 4.9 occurs during atrial systole just before ventricular systole. Also here it is seen that the vortices are more distinct with increasing γ, and the intraventricular velocity increases with γ. Furthermore, we see that as

γ increases, three vortices are present in the ventricle. This is very difficult to see at $\gamma = 0.04$. Even though the velocity field is different inside the heart, the heart boundary is practically the same for all 4 γ values.

The flow in Figure 4.10 occurs at the end of the heart cycle. We see that at $\gamma = 0.04$ it is possible to see one intraventricular vortex, while at $\gamma = 0.1$, 0.3 and 0.5 two vortices are present. Note that a vortex is formed at the aortic outflow tract as a consequence of the simple geometry of this tract.

The comparison of velocity fields indicates that the original choice of $\gamma = 0.04$ is not optimal, since at $\gamma = 0.04$ the vortex structure is not captured very well. To further elucidate the influence of γ we plot pressure time profiles, velocity time profiles and source flow time profiles from the simulations with $\gamma = 0.04$, 0.1 and 0.5.

Figure 4.11 shows the pressure time profile for the ventricle, atrium and aortic sink. The velocity curves for $\gamma = 0.1$ and 0.5 are quite similar, while for $\gamma = 0.04$ the maximum level for the ventricular curve is too low and the maximum level at the aortic sink is too high. We believe that the lower maximum level of the aortic sink pressure is related to the formation of the vortex in the aortic outflow tract as seen in Figure 4.10.

Figure 4.12 shows the velocity time profile at the mitral ring and between the mitral leaflet tips, while Figure 4.13 shows the velocity time profile across the aortic sink. From Figure 4.12 we see that the velocity over the mitral ring is not

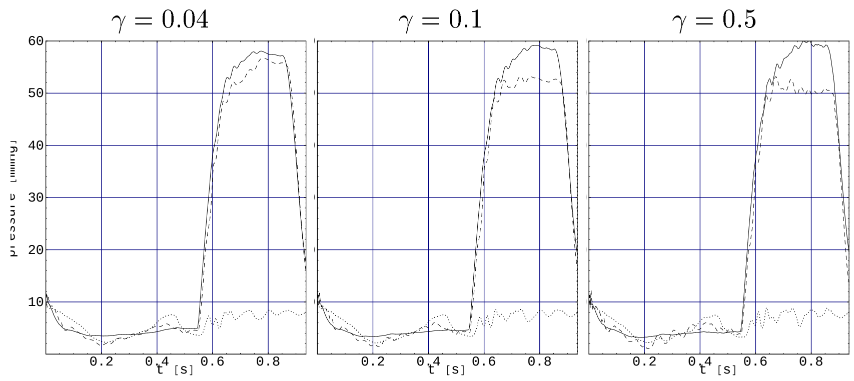

Figure 4.11: Pressure time profile for the pressure (mmHg) in the ventricle (solid), atrium (dotted) and at the aortic sink (dashed), with $\gamma = 0.04$ (left), $\gamma = 0.1$ (middle) and $\gamma = 0.5$ (right).

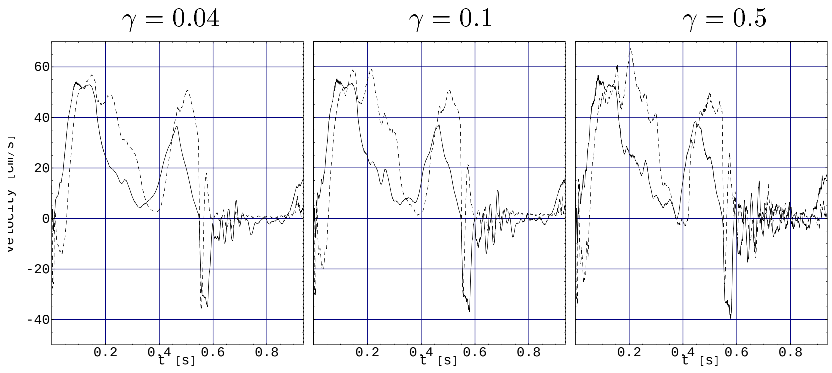

Figure 4.12: Velocity time profile of the mean velocity (cm/s) over the mitral ring (solid) and between the leaflet tips (dashed), with $\gamma = 0.04$ (left), $\gamma = 0.1$ (middle) and $\gamma = 0.5$ (right).

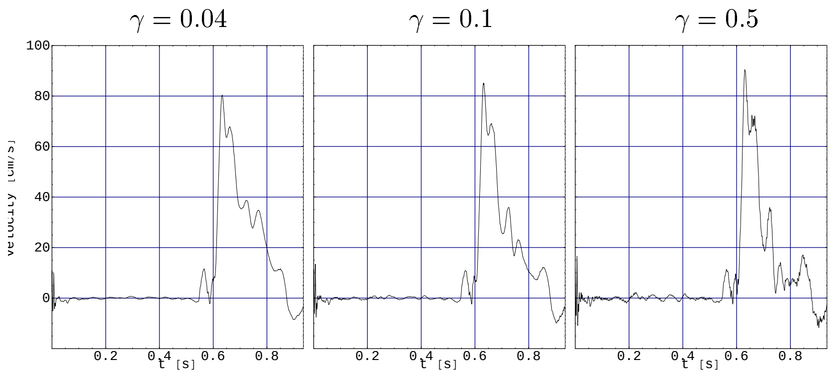

Figure 4.13: Velocity time profile of the mean velocity (cm/s) across the aortic outflow tract below the aortic sink, with $\gamma = 0.04$ (left), $\gamma = 0.1$ (middle) and $\gamma = 0.5$ (right).

affected very much by increasing γ value: peak values are almost the same and the time variation is similar, though more oscillations are seen as γ increases. Note that for $\gamma = 0.5$ the velocity over the mitral ring is zero at approximately $t = 0.375$ s between the two forward peaks. As we shall see in the comparison between the model and MR measurements in Chapter 5, this is a desirable feature. For the velocity between the leaflet tips the time variation is similar, while the forward peak velocities are higher with increasing γ value. For $\gamma = 0.5$ we see a negative velocity between the two forward peaks, and for all γ values we see a negative velocity peak following the second forward peak. The latter is related to the closure of the mitral valve.

Figure 4.13 shows that the general aortic velocity profile is similar for different γ values. As seen for the mitral velocity the oscillations are more pronounced with increasing γ value and the peak value increases.

Generally, we see that the scaling factor γ does have an influence on the flow pattern. It does not change the overall flow pattern, but local differences are seen. The intraventricular velocity increases with increasing γ value and the vortex formation is more distinct. Furthermore, the maximum pressures achieved in the ventricle and at the aortic sink are also affected.

When the model is used for physiological investigations the user is interested in as short a simulation time as possible while still obtaining reasonably correct results. A short simulation time requires a small value of γ. A simulation with $\gamma = 0.5$ is possible on a 256 (or finer) grid, while a simulation with $\gamma = 0.1$ can run on a 128 grid with 29952 time step per heart cycle, and a simulation with $\gamma = 0.04$ can run on a 64 grid with 2808 time steps per heart cycle.

Based on our comparisons between simulations with different γ values and considering simulation times, we believe that $\gamma = 0.1$ is a good choice. At $\gamma = 0.1$ the pressure time variation and the velocity time profiles are close to those at $\gamma = 0.5$, and the flow pattern inside the heart is similar to the flow pattern seen at $\gamma = 0.5$. In Thorup (1997) it was concluded that $\gamma = 0.04$ was a good choice, but the investigation there was performed with the model before the tethering of the heart was implemented. It turns out that the tethering decreases the stability of the model.

4.3 Periodic boundary conditions

In the model the heart is placed in a computational domain with periodic boundary conditions. This means that if the heart moves past one boundary it will appear at the opposite boundary. An example of such a situation can be seen in Figure 4.1

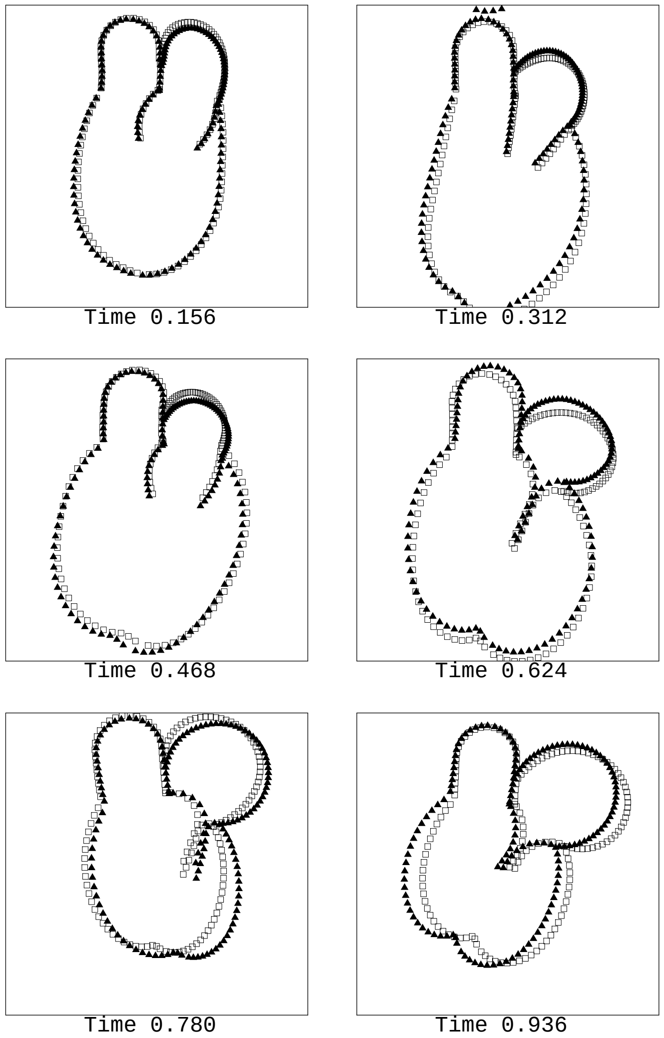

Figure 4.14: Heart boundary at six equidistant times during a heart cycle from the reference simulation (▲) and from a simulation with a large computational domain (□). Field of view is identical to the computational domain of the reference simulation.

at $t = 1.404$ s. Furthermore, if the dimension of the heart exceeds the domain dimension the heart will overlap itself.

To determine the influence of the periodic boundary conditions we make a simulation where the heart is immersed in a large computational domain (on a 512 grid), but where all parameter values determining the initial set up of the heart (including the size) are identical to our reference simulation.

In Figure 4.14 the heart boundary configuration from the simulation with the large computational domain and from the reference simulation is depicted. We see a small deviation between the two heart boundary configuration. There is hardly any difference between the pressure time profiles seen in Figure 4.15 or between the velocity time profiles at the mitral ring and between the leaflets depicted in Figure 4.16.

Figure 4.17 shows the velocity time profile for the aortic outflow tract, while Figure 4.18 shows the flow time profiles for the mitral source flow and the aortic sink flow. In both of these figures we find small discrepancies between the results from the reference simulation and from the simulation with a large computational domain. From Figure 4.18 we see that the aortic sink opens and closes at the same time in the two simulations and that the peak inflow through the source and the

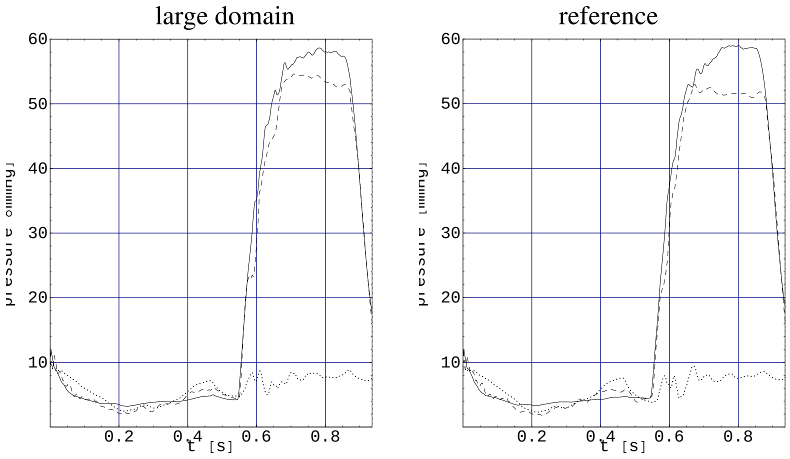

Figure 4.15: Pressure time profiles for the pressure (mmHg) in the ventricle (solid), atrium (dotted) and at the aortic sink (dashed) from a simulation with a large computational domain (left) and from the reference simulation (right).

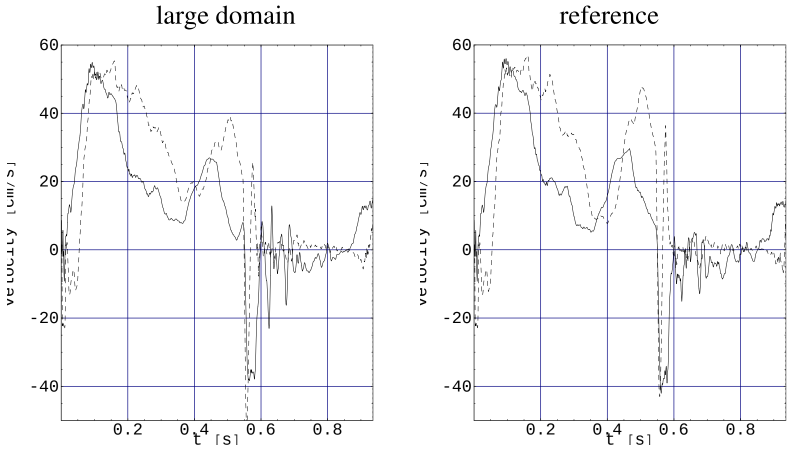

Figure 4.16: Velocity time profile for the mean velocity (cm/s) over the mitral ring and between the leaflet tips from a simulation with a large computational domain (left) and from the reference simulation (right).

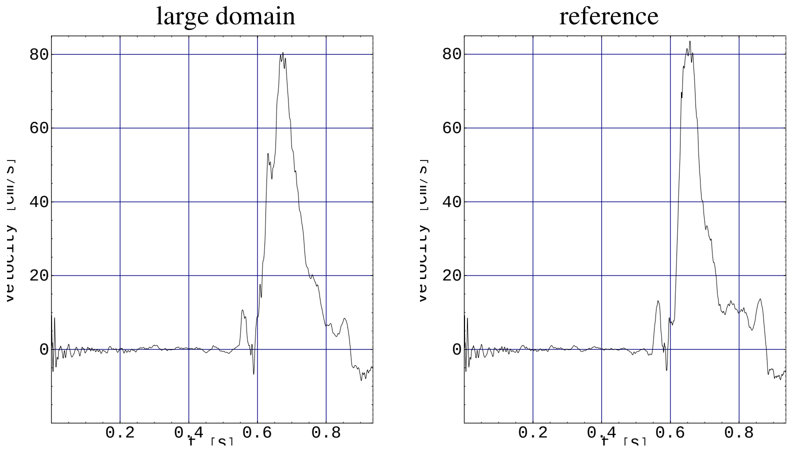

Figure 4.17: Velocity time profile for the mean velocity (cm/s) across the aortic outflow tract below the aortic sink from a simulation with a large computational domain (left) and from the reference simulation (right).

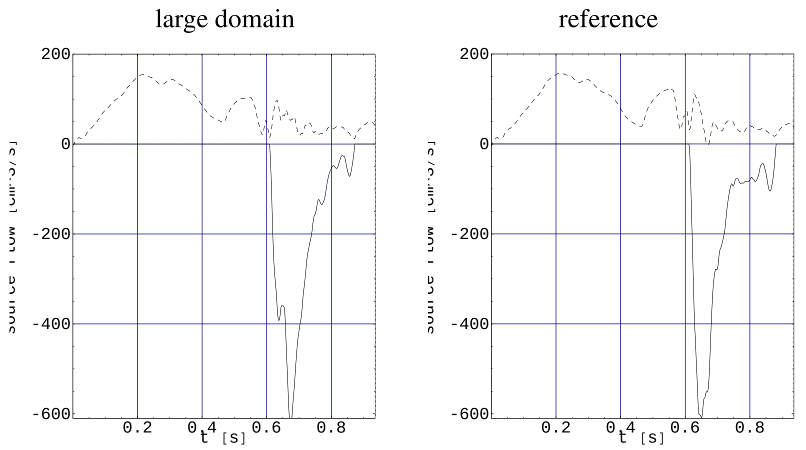

Figure 4.18: Flow time profiles for the flow (cm^3/s) through the mitral source and aortic sink from a simulation with a large computational domain and from the reference simulation.

peak outflow from the sink is the same.

We conclude that results from the heart model are not influenced significantly by the periodic boundary conditions. However, for visual reasons it would be desirable if the computational domain was a little bit larger to allow the heart to stay inside the domain during a full simulation. This would mean that the computations should be performed either on the same grid size but with a slightly smaller heart (giving a coarser resolution of the heart) or on a finer grid with the heart size identical to the size at the coarse grid (giving approximately 2^2 times as much computational time, because the number of grid points N has to be a power of 2). Since the results are not affected by the periodic boundary conditions, we have chosen not to change the grid size or the heart dimension.

4.4 Tethering of the heart

In the original model the heart floated freely in the computational domain, and this resulted in non-physiological movements, especially during the ejection phase when a translation would begin and eventually move the heart through the boundary. Figure 4.19 shows the velocity field and heart boundary configuration at 4

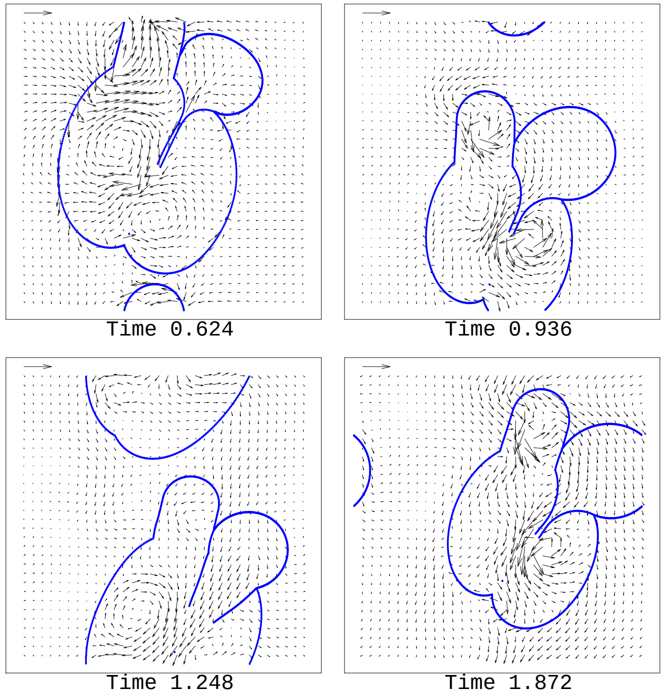

Figure 4.19: Velocity field and heart boundary configuration at four times during two heart cycles from a simulation with no tethering of the heart.

times during 2 heart cycles of a simulation where the heart is not tethered.

In the first frame in Figure 4.19 it is seen that the heart moves through the upper boundary. While from the second frame (at $t = 0.936$ s), which is at the end of the first heart cycle, it is seen that the heart has begun to move through the lower boundary. This development is even clearer in the third frame. In the last frame, at the end of the second heart cycle, the heart is again intact inside the field of view. Thus during two heart cycles the heart moves a distance corresponding to the size of the computational domain.

To restrain the heart from moving, we tethered it to a set of fixed points as described in Section 3.3.7. In Figure 4.20 the velocity field and heart boundary configuration from a simulation where the heart is tethered are shown for the same

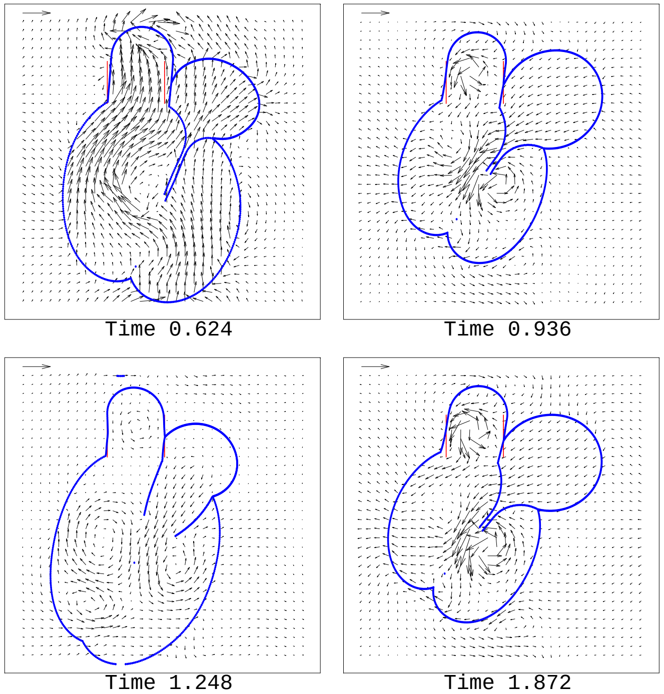

Figure 4.20: Velocity field and heart boundary configuration at four times during two heart cycles from the reference simulation.

times as in Figure 4.19

Figure 4.20 shows that the tethering works efficiently in keeping the heart in place. The heart is allowed to move a little, but not too much. Furthermore, we see that the flow field in the heart is not very different from that in a heart with no tethering, except during outflow through the aortic sink (the first frame at $t = 0.624$ s). In the same frame we see that with the tethering the intraventricular flow field is dominated by an outflow jet from the ventricle toward the aortic sink, while in the simulation without tethering the intraventricular flow field seems calmer and exhibits a vortex between the anterior wall and the mitral leaflets. The tethering has also introduced oscillations in both the atrium and the ventricle. The oscillations of the atrium can be seen when comparing successive plots of the

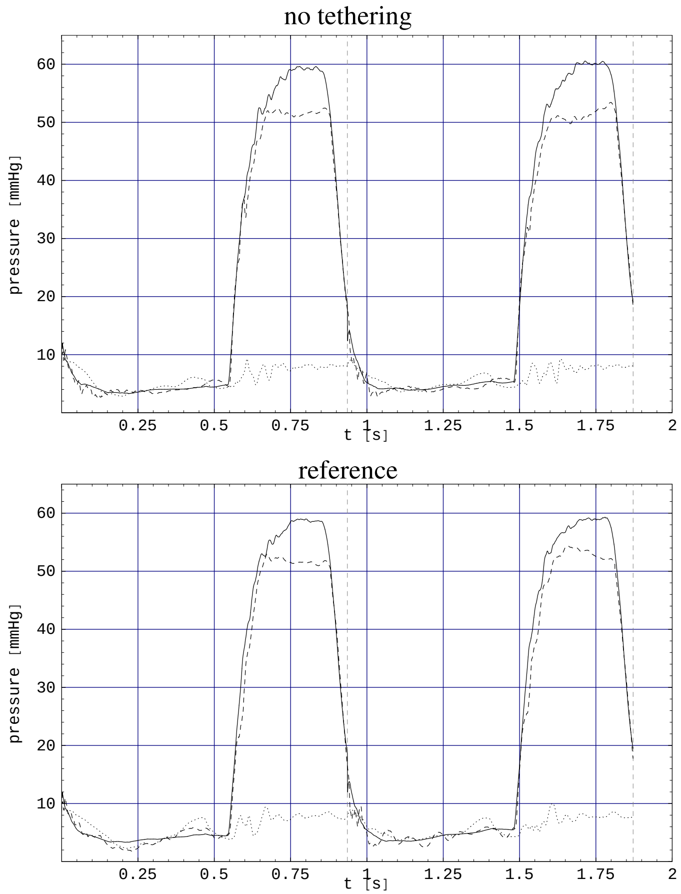

Figure 4.21: Pressure time profile for the pressure (mmHg) in the ventricle (solid), atrium (dotted) and at the aortic sink (dashed) from a simulation with no tethering of the heart (top) and from the reference simulation (bottom).

heart wall. This is not seen in the plots shown here because they are too far apart in time. The oscillations of the ventricle are best seen when an animation of the pictures is performed.

To further examine the influence of the tethering we compared the time variation of the pressure, velocity and flow from the two simulations.

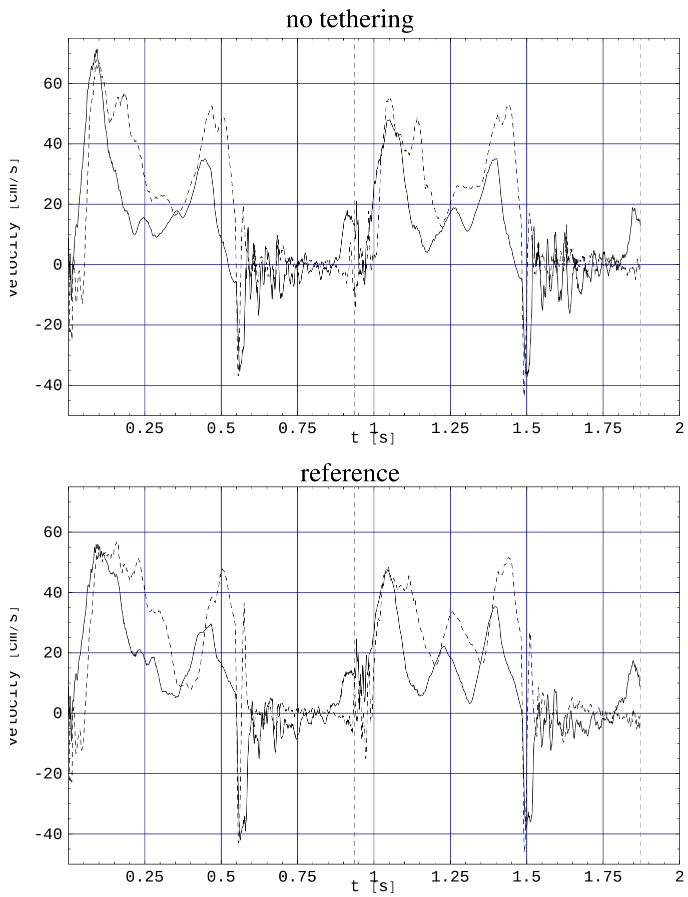

Figure 4.22: Velocity time profile for the mean velocity (cm/s) at the mitral ring (solid) and between the leaflet tips (dashed) from a simulation with no tethering of the heart (top) and from the reference simulation (bottom).

Figure 4.21 shows the time variation of the pressure. It is seen that the maximum level for the ventricular pressure is slightly higher without the tethering, while the maximum pressure level for the aortic sink is higher in the second cycle with tethering. Apart from that, the time variation of the pressures are very similar.

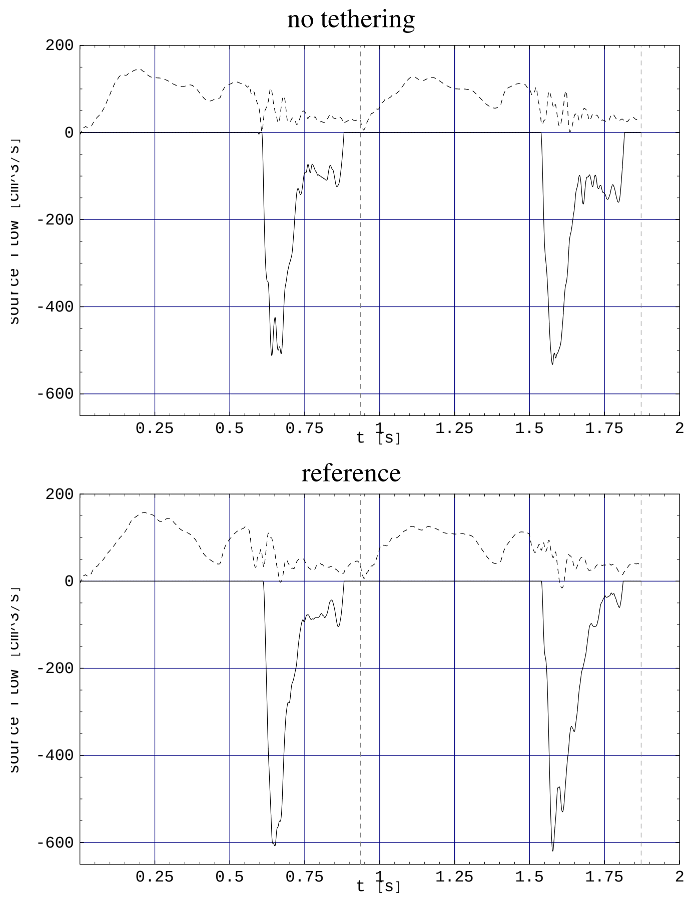

Figure 4.23: Flow time profile for the flow (cm^3/s) through the mitral source (dashed) and the aortic sink (solid) from a simulation with no tethering of the heart (top) and from the reference simulation (bottom).

In Figure 4.22 the velocity time profiles for the mitral ring and between the leaflet tips are shown. Especially in the first cycle differences between the velocity profiles exist: the peak forward velocity in the profiles in the simulation with no tethering is clearly higher than in the simulation with tethering. Furthermore, the shape of the velocity profile during the first peak is wider with tethering than without. In the second cycle the velocity profiles from the two simulations are much more similar.

Figure 4.23 shows the time variation of the flow through the mitral source and aortic sink. The peak outflow is slightly larger in the simulation with tethering than in the simulation with no tethering, but the shapes of the profiles are similar. In the simulation with tethering the flow through the mitral source becomes negative, indicating that blood is flowing back through the mitral source. This is not an unphysiological feature, since the pressure inside the heart can be such that blood leaves through the pulmonary veins (the pulmonary veins have no valves to prevent this).

The introduction of tethering prevents the heart from moving too much without significantly changing the flow pattern. The time variation of the pressure is almost the same, while some differences are seen in the velocity and source flow profiles. For the velocity profiles the main differences are in the first heart cycle. Since preventing the heart from moving around in the computational domain is a major improvement, we conclude that the tethering of the heart is successful, even though some changes are introduced in the results we have made this part of the model.

4.5 The Windkessel model

The Windkessel model for the afterload of the heart was introduced in Jacobsen (1999) and evaluated in both Jacobsen (1999) and Adeler and Jacobsen (2001). We include here a summary of that evaluation to complete the description and evaluation of our 2D model.

The Windkessel model was introduced to improve the outflow conditions at the aortic sink. Originally, the outflow was determined by a linear resistance model (similar to the one for the atrial source), but this gave an unrealistic pressure

	onset syst. [ms]	end syst. [ms]	K_r [ms^{-1}]	K_e [ms^{-1}]	α_{max}	$\alpha^0 = \alpha(t=0)$
atrium	0.347	0.422	1/60	1/54	2.0	0
ventricle	0.447	0.547	1/60	1/15	4.9	1.07
pap. musc.	0.447	0.547	1/60	1/15	4.9	0.107

Table 4.1: Timings, rate constants, limiting values and initial values for the activation functions for the dog heart (McQueen et al., 1982).

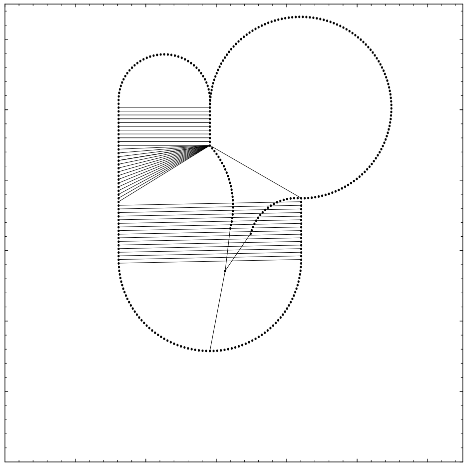

Figure 4.24: Initial geometry of the dog heart, compare with Figure 3.7. Note that the heart is not tethered to any fixed points.

time profile at the sink, where the pressure was almost clamped at the prescribed constant pressure in the aorta. To investigate the influence of the Windkessel model connected to the aortic sink, we made a comparison between a simulation with Peskin's original model and a simulation where the only modification introduced is the Windkessel model. Peskin's original model is based on a dog's heart, i.e. none of the improvements presented earlier in this thesis to make the model human were implemented. The length of a dog's heart cycle was taken to be 0.675 s.

The parameters for the activation function are listed in Table 4.1 and the initial geometry for the dog's heart is shown in Figure 4.24 (compare these with Table 3.1 and Figure 3.7 for the modified model). Note that the length scales are not the same in the model of a dog's heart (Figure 3.7) and in the modified model (Figure 4.24): for the dog's heart the length of the computational domain corresponds to 7.35 cm, while in our modified model it corresponds to 13 cm.

Figure 4.25 shows pressures from a simulation of a dog's heart without the Windkessel model over 3 cycles. It is apparent that the model operates at a pressure which is only about 1/2 of that of the physiologically correct pressure for a dog, which corresponds to approximately 1/3 of the human case. Note that the pressure at the aortic sink is held at an almost constant level when the sink is open.

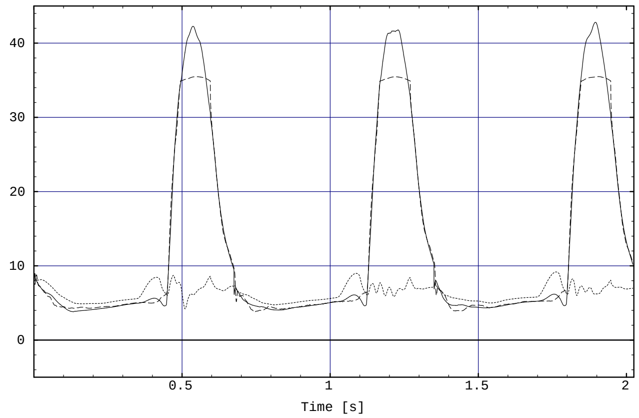

Figure 4.25: Pressure time profile during three heart cycles for the pressure (mmHg) in the ventricle (solid), atrium (dotted) and at the aortic sink (dashed) from a simulation without the Windkessel model.

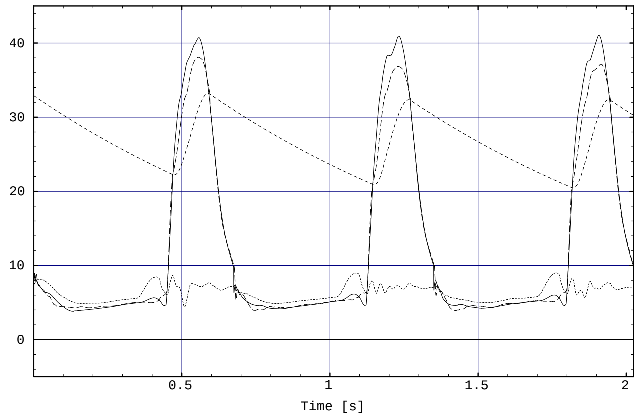

Figure 4.26: Pressure time profile during three heart cycles for the pressure (mmHg) in the ventricle (solid), atrium (dotted), at the aortic sink (long dashed) and the load pressure P_{snk} (short dashed) from a simulation with the Windkessel model.

However, the atrial pressure is approximately at the physiological level.

Figure 4.26 shows the pressure profiles corresponding to those in Figure 4.25, but with the outflow through the aortic sink determined by the Windkessel model. The figure also includes the time variation of the load pressure P_{snk} introduced in equation (3.10). The values of the Windkessel parameters are adapted from Cappello et al. (1995) as follows: Since the model operates at a pressure of 1/3 of the physiological levels used in Cappello et al. (1995), the values for the resistances are divided by 3 while the compliance is multiplied by 3. Thus the Windkessel parameters are: $R_{snk1} = 0.033$, $R_{snk2} = 0.8$ mmHg/(cm^3/s) and $C = 1.5$ cm^3/mmHg.

The introduction of the Windkessel model does not change the ventricular pressure significantly, but the pressure at the aortic sink is no longer clamped to an almost constant value. Rather, it varies in a more physiological realistic way. The time interval during which the aortic sink is open is larger when the Windkessel model is introduced.

The results presented here show that the pressure profile at the aortic outflow tract is considerably improved through the use of a Windkessel model rather than a linear resistance model coupled to a constant pressure reservoir. Jacobsen (1999) also reports that it does not make a significant difference whether a non-linear compliance (i.e. a pressure dependent compliance) is used. Based on these investigations we therefore chose to implement a Windkessel model with a constant compliance in the heart model. After implementing all of our modifications in the model, we adjusted the Windkessel parameters based on a comparison of simulations and MR data. We ended with the following parameter choice: $R_{snk1} = 0.014$ mm Hg/(cm^3/s), $R_{snk2} = 0.69$ mm Hg/(cm^3/s) and $C = 2.63$ cm^3/mm Hg.

4.6 Distributed sources and sinks

The work presented in this section was performed by Jakobsen and Niss (2000) based on an unpublished note by Peskin (1998). We include here a brief summary of Jakobsen and Niss's (2000) work.

When distributed sources and sinks were introduced in the heart model (Peskin, 1977) the standard continuity equation expressing incompressibility

$$\nabla \cdot \boldsymbol{u} = 0$$

was modified to

$$\nabla \cdot \boldsymbol{u} = \psi$$

where ψ (depending on both time and space) expresses the distribution of the sources and sinks, as described in Section 3.2.1. This was done without modifying the momentum equation (the Navier-Stokes equation)

$$\rho\left(\frac{\partial \boldsymbol{u}}{\partial t}+(\boldsymbol{u}\cdot\nabla)\boldsymbol{u}\right)u=-\nabla p-\mu\nabla^2\boldsymbol{u}+\boldsymbol{F}$$

even though the derivation of the Navier-Stokes equation is based on the continuity equation.

Assumptions about the momentum at the sources and sinks have to be made to correctly derive the momentum equation with the modified form of the continuity equation. At a sink it is assumed that fluid leaving the model takes its momentum with it. At a source one can either assume that fluid enters the model with no velocity (and thus with no momentum because the fluid is incompressible and homogeneous) or that fluid enters with the same velocity as the fluid at the source. The former assumption was proposed by Peskin (1998), while Jakobsen and Niss (2000) proposed the latter. The difference between deriving the momentum equation based on the former or the latter assumption concerning fluid entering the model is in the term describing the change in momentum caused by the sources and sinks. This difference is described below, we refer to Jakobsen and Niss (2000) for details.

To be able describe inflow and outflow separately the following are defined

$$\psi^+=\begin{cases}\psi & \text{if } \psi>0\\ 0 & \text{if } \psi\le 0\end{cases}\qquad \psi^-=\begin{cases}0 & \text{if } \psi\ge 0\\ \psi & \text{if } \psi<0\end{cases}$$

Thus ψ^+ describes the distribution of inflow through sources, and ψ^- describes the distribution of outflow through sinks.

With the assumptions that fluid entering the model has no momentum and fluid leaving the model takes its momentum with it, the change in momentum related to the sources and sinks is

$$\int_A u_i\rho\psi^-\,dA$$

where A is a fixed area. Using this in the derivation of the momentum equation gives

$$\rho\left(\frac{\partial \boldsymbol{u}}{\partial t}+(\boldsymbol{u}\cdot\nabla)\boldsymbol{u}\right)u=-\nabla p-\mu\nabla^2\boldsymbol{u}+\boldsymbol{F}-\psi^+\boldsymbol{u}$$

Thus the momentum equations is not the standard Navier-Stokes equation.

With the assumptions that fluid enters the model with the same velocity (i.e. same momentum) as the fluid at the source and fluid leaving the model takes its momentum with it, the change in momentum related to the sources and sinks becomes

$$\int_A u_i\rho\psi\,dA$$

Using this term in the derivation of the momentum equation leads to the following equation:

$$\rho\left(\frac{\partial \boldsymbol{u}}{\partial t}+(\boldsymbol{u}\cdot\nabla)\boldsymbol{u}\right)u=-\nabla p-\mu\nabla^2\boldsymbol{u}+\boldsymbol{F}$$

This is the standard Navier-Stokes equation, even though the continuity equation was not in standard form.

This shows that the use of the standard Navier-Stokes equation together with the non-standard continuity equation does not lead to inconsistencies in the model, but is based on sensible assumptions concerning the fluid entering the model.

These derivations are not specific to the heart model, but are valid for an arbitrary fluid dynamical model with distributed sources and sinks. In the case of the heart model, it is necessary to discuss which of the two assumptions concerning the fluid entering the model is correct. Since blood enters the atrium during both diastole and systole, we believe it would be unphysiological to assume that blood enters the heart with the same velocity as the blood already in the atrium has. It is more correct to assume that blood enters with a lower velocity. Thus we believe that none of the stated assumptions about fluid entering the model are correct, but the assumption that the fluid entering the model has no velocity might be closer to the physiologically correct situation.

Jakobsen and Niss (2000) examine the differences in simulation results (particularly the velocity field) between the two equations of momentum described above. They find that there are only minor differences in the velocity field, probably due to the fact that the velocity of the fluid at the sources, where fluid enters the model, is small. We conclude that even though different assumptions about the fluid entering the model lead to different momentum equations, this does not lead to major differences in the simulation results. Thus we do not find it necessary to include the new form of the momentum equation in the model.

4.7 Simulation over several heart cycles

When the model is used for physiological experiments and comparisons it is important to determine at which point the model becomes periodic. This can be determined by making a simulation over many heart cycles and examining at which point the model becomes (practically) periodic from one heart cycle to the next.

When determining the appropriate heart cycle number, it is also necessary to consider the computation time. For our reference simulation two heart cycles take approximately 3 1/2 hours to compute on a 700 MHz Pentium III processor. When performing physiological experiments it is our experience that, because of the complexity of the model, many simulations are needed before the correct setting of the model is achieved. Thus a short computation time is very important.

We make a run with the reference model over 15 heart cycles. It is evident from the results that the output becomes (practically) periodic within the first 4 heart cycles. We do not see that the output becomes perfectly periodic, not even within 15 heart cycles, e.g. the amplitudes of especially the velocity and flow time profiles vary a little.

Figure 4.27 shows the pressure time profiles, Figure 4.28 the velocity time profile at the mitral ring, Figure 4.29 the velocity time profile across the aortic outflow tract and Figure 4.30 the sources flow profile, in all cases for the first 4 heart cycles of our reference simulation.

From Figure 4.27 it is seen that the pressure in the atrium is slightly different in the first cycle than in the following, the ventricular pressure is practically the same, while the maximum level of the pressure at the aortic sink increases slightly during the four heart cycles. The shape of the mitral velocity profile (Figure 4.28) is different in the first cycle than in the following ones: the first peak is higher and the shape during that peak is wider. Furthermore, from the second cycle and onward three forward peaks are present. The first peak slightly decreases during the last three cycles plotted. The difference between the first cycle and the following cycles are closely related to the fact that the model begins with the fluid being at rest.

In Figure 4.29 it is seen that the velocity profile across the aortic tract from the third and fourth heart cycles are very similar. In the first two cycles the peak velocity is higher, and the shape of the curve is slightly different in the first cycle compared to the following cycles. The flow through the atrial source from the second, third and fourth heart cycle is very similar, while minor differences exist between the first cycle and the following cycles. For the flow through the aortic sink we see the same tendencies as for the velocity across the aortic outflow tract: the third and fourth heart cycles are very similar. The shape of the curve in the second cycle is similar to the shape in the third and fourth, but the peak outflow is larger and for the first cycle the shape shows small differences compared to the following cycles and the peak outflow is larger than in the third and fourth cycles.

We conclude that it is reasonable to take the results from the second heart

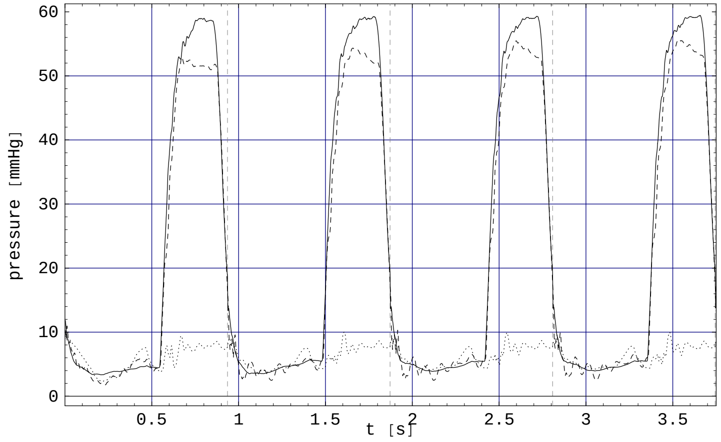

Figure 4.27: Pressure time profile during 4 heart cycles for the pressure (mmHg) in the ventricle (solid), atrium (dotted) and at the aortic sink (dashed).

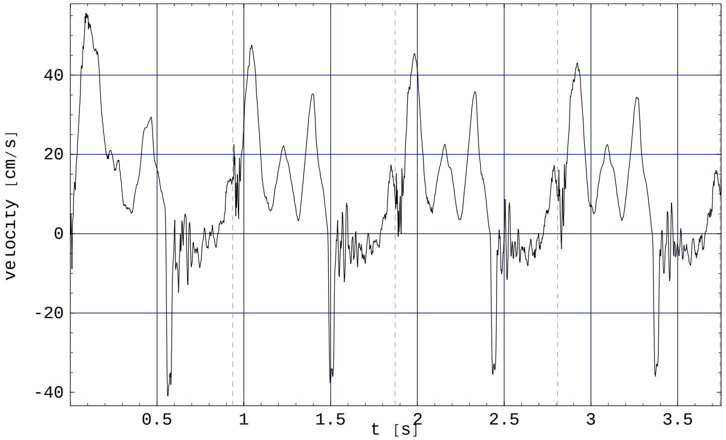

Figure 4.28: Velocity time profile during 4 heart cycles for the mean velocity (cm/s) at the mitral ring.

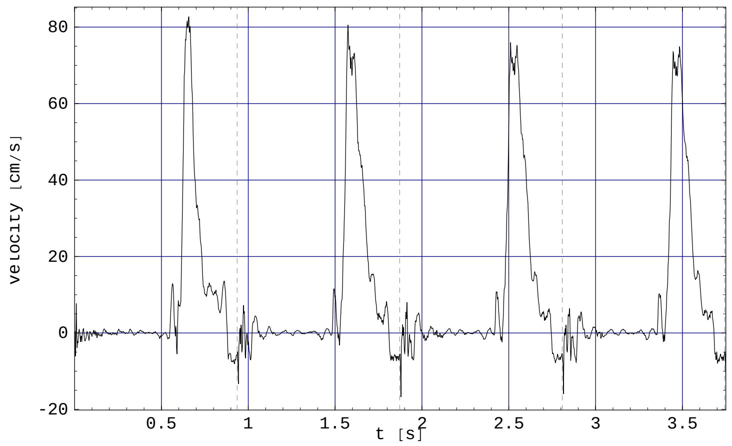

Figure 4.29: Velocity time profile during 4 heart cycles for the mean velocity (cm/s) across the aortic outflow tract below the aortic sink.

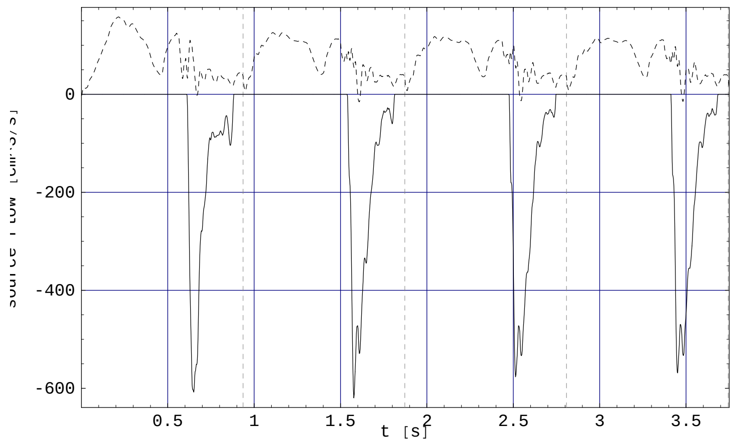

Figure 4.30: Flow time profile during 4 heart cycles for the flow (cm^3/s) through the mitral source (dashed) and the aortic sink (solid).

cycle when physiological experiments are carried out with the model. This is based on the good comparison between the results from the second heart cycle and the following third and fourth cycles and on the need to run many simulations when experiments are carried out. Thus choosing the second and not the third cycle reduces the computational time.

4.8 Conclusions

We have seen that the scaling factor γ has an influence on the flow pattern inside the heart. It does not change the overall flow pattern, but local differences are seen. Comparing the simulation results from simulations with different γ values and taking the computational time into account, we have chosen $\gamma = 0.1$ as a good choice. The flow pattern resembles well the flow pattern seen in the $\gamma = 0.5$ simulation and the time variation of pressure and mean velocities are similar to those obtained at $\gamma = 0.5$.

We have investigated the influence of the periodic boundary conditions by embedding the heart in a larger computational domain and comparing it with our reference simulation. This comparison showed only minor differences between the simulations. Thus we conclude that the periodic boundary conditions do not influence the results and the size of the computational domain in relation to the chosen heart dimension is reasonable.

We examined the consequences of tethering the heart to a set of fixed points as described in Section 3.3.7 by comparing simulations with and without tethering. We found that the tethering successfully prevented the unphysiological movement of the heart and only introduced a few changes in the results.

We have showed that the implemented Windkessel model for the outflow through the aortic sink improves the shape of the pressure curve for the pressure at the aortic sink without introducing significant changes in the velocity field.

We have compared the results from the first 15 heart cycles of our reference simulation and found that it is acceptable to use the results from the second cycle in experiments with the model. The first cycle is considerably different from the following cycles, while the results from the second cycle are close to those from the following cycles.

The investigations performed in this chapter show that the results from the second heart cycle of a reference simulation computed on a 128 grid with 29952 time steps per heart cycle, with $\gamma = 0.1$, and with all other parameters as described in Chapter 3, are the results from the 2D heart model that should be taken as representative.

Chapter 5

Comparing the 2D model with an MR data set

The ultimate evaluation of the heart model is a comparison between model results and measurements performed on a human, which in our case are MR measurements. This chapter is partly based on Jacobsen et al. (2001) and Adeler and Jacobsen (2001). However, we have changed the initial geometry and the tethering since the results presented in the mentioned papers, and here we compare our new model results with the same MR data set. The new initial geometry and tethering are those described in Section 3.3.7.

The comparison falls into two parts, each represented by its type of data:

- Velocity fields and heart wall boundary.
- Velocity profiles at the mitral ring and at the aortic outflow tract.

5.1 The MR data

We use MR data from a study in Kim et al. (1995) conducted on 26 healthy volunteers, 18 men and 8 women. Their mean age was 25 years (in a range from 21 to 30 years). The volunteers had no known cardiac or systemic diseases. For the comparison with our simulated heart model, one of the 26 sets of MR data was chosen. See Appendix A for an explanation of the technicalities of the MR method.

In the MR data collecting process, a conventional spin echo sequence was used for a coronal image of the heart followed by a single angulation through the aortic valve and the apex of the heart to yield a long axis view of the left ventricle. In Kim et al. (1995) the long axis plane of the left ventricle was chosen because it contains both the aortic outflow and the mitral inflow, as well as the left ventricle and left atrium. For the comparison between MR data and model, the long axis plane is well suited since it is consistent with the computational plane of the 2D model.

Image acquisition was prospectively triggered by the R wave of the electrocardiogram, so the first recorded frame was 8 ms after the R wave. This corresponds approximately to the time of closure of the mitral valve.

The intracardiac flow velocity measurements were obtained using the standard FLAG (Flow Adjusted Gradients) sequence, which is described in Groen and Dijk (1987). The recordings were conducted in a square 40 cm field of view with an in-plane resolution of 3.125 mm $\times$ 3.125 mm giving an imaged slice of 128 $\times$ 128 voxels (volume elements). The following parameter settings were used for the flow measurements: 45 degrees flip angle, 9.5 ms echo time, 7.1 ms acquisition time, and 10 mm slice thickness. The velocity sensitivity was set to produce a maximum phase shift at a velocity of ± 1.25 m/s to ± 1.67 m/s to avoid aliasing. Velocity encoding was performed in all three spatial directions to produce three-dimensional velocity information from each voxel inside the field of view. The time needed for the quantitative velocity acquisitions (using ECG gating to avoid motion artifacts) was 15 to 20 min for each subject, depending on the heart rate. The procedure resulted in the recorded MR data being averaged over 768 heart beats. For the 26 examined persons the temporal resolution was 28 ms$\pm$3.8 ms (mean$\pm$standard deviation (SD)) with 25-32 frames per cardiac cycle. For the specific MR set with which the comparison was carried out, the temporal resolution was 36 ms with 26 frames per cardiac cycle giving a total length of the heart cycle of 936 ms. The total recording time was 1152 ms, i.e. approximately $1\frac{1}{4}$ heart cycles.

The accuracy of quantitative flow measurements by the MR phase technique depends on the suppression of artifacts. The velocity maps were corrected for possible linear phase errors resulting from eddy currents in the magnetic field. In addition, masking of random noise in the stationary tissue was done. Both procedures were performed by a semi-automated software program, which is described in detail in Walker et al. (1993).

An MR data set consists of the three-dimensional velocity information in each voxel and the modulus image at each time frame. The modulus image contains information on the MR signal amplitude, which depends e.g. on the specific tissue

and the velocity of the flow in the voxel. The modulus image is displayed as a grey-scale picture and can, as such, be used to roughly determine the internal anatomy and also the magnitude of the flow. For the comparison with the 2D heart model we were only interested in the in-plane components of the velocity. The in-plane velocity components can be displayed as velocity field vectors. Presenting the velocity field plot superimposed on the corresponding modulus image shows both the magnitude and the direction of the blood. It is also possible at each time frame to extract velocity information from one or several voxels, and this can be used to plot a velocity profile (velocity as function of time) at a specific place in the imaged slice. In the velocity field plot we show below we have indicated the voxels from which velocity information is extracted to calculate velocity time profiles.

5.2 Velocity fields

The starting time of the MR data is different from that of the simulation. The natural start of the MR data is at the closure of the mitral valve, while the simulation starts in early ventricular diastole. We have chosen to show all results according to the time course of the simulation, i.e. starting with early ventricular diastole, and have shifted the velocities of the MR measurements from the first cycle, accordingly. The matching was done by synchronizing the time of the early peak velocity (also called the E peak) in the first heart cycle in the velocity time profile of the centre velocity at the mitral ring in the model with the time of the E peak in the velocity time profile at the mitral ring in the MR data.

In Figures 5.1–5.3 the velocity field is shown at 8 different times during a heart cycle as velocity vectors along with the heart wall boundary. We have used the results from the second heart cycle of the model, so the simulation time runs from $t = 0.936$ s to $t = 1.872$ s. In the model, the heart wall boundary is computed and is therefore easily plotted. In the MR data, the interior of the heart boundary (not the valve leaflets) was manually traced from plots of the velocity field superimposed on the modulus image. The boundary is given a width equal to the spatial resolution of the MR measurements, i.e. 3.125 mm. We emphasize that the determination of the interior boundary from the MR data is rather uncertain and that it should be only taken as an indication of its position.

We begin with a description of the results in Figures 5.1–5.3. This will give an introduction to the time sequence of a heart cycle and provide the basis for our comparison.

Early mitral inflow. The results start with the early mitral inflow. The mitral

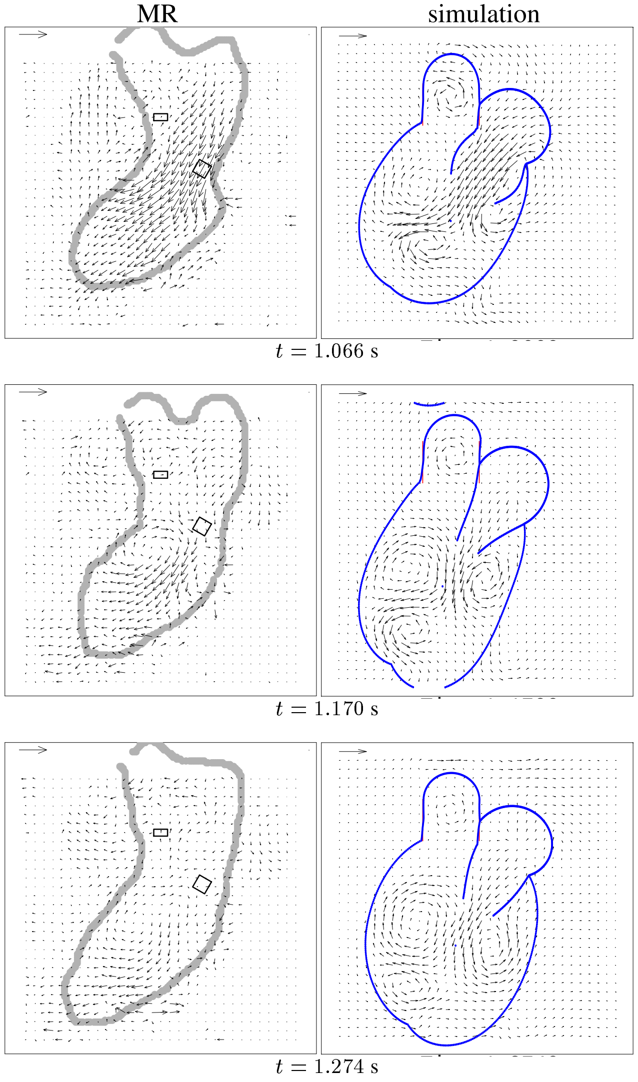

Figure 5.1: Velocity field and heart boundary from MR measurements (left) and reference simulation (right) at three times during a heart cycle characterized by: early peak mitral inflow (top), temporary maximal anterior vortex in the MR data (middle) and a decline in inflow (bottom).

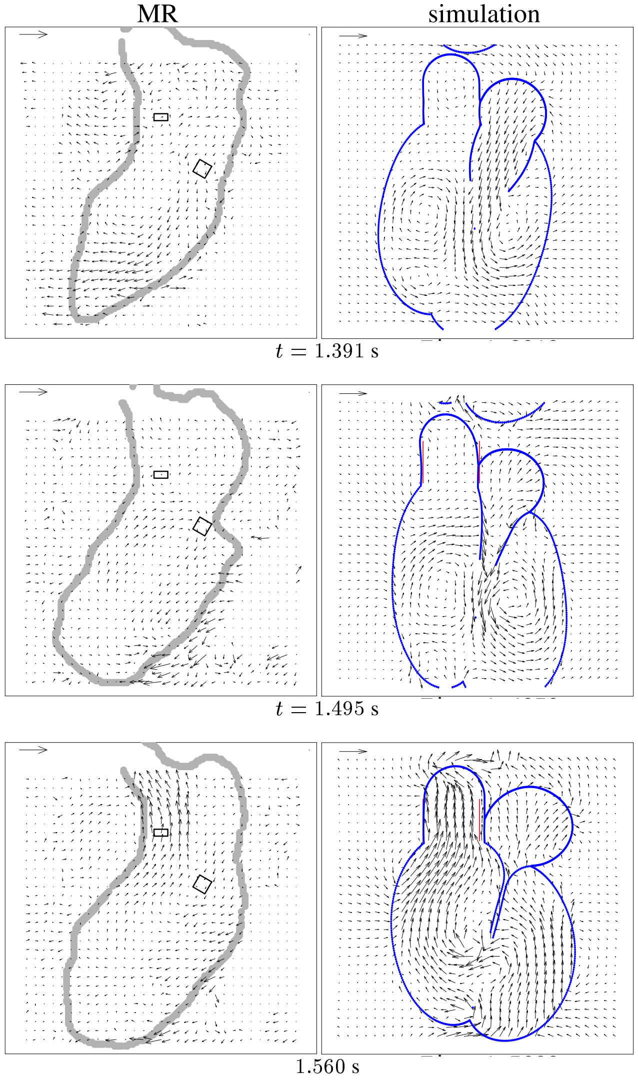

Figure 5.2: Velocity field and heart boundary from MR measurements (left) and reference simulation (right) at three times during a heart cycle characterized by: atrial systole in simulation (top), closure of mitral valve (middle) and early aortic outflow (bottom).

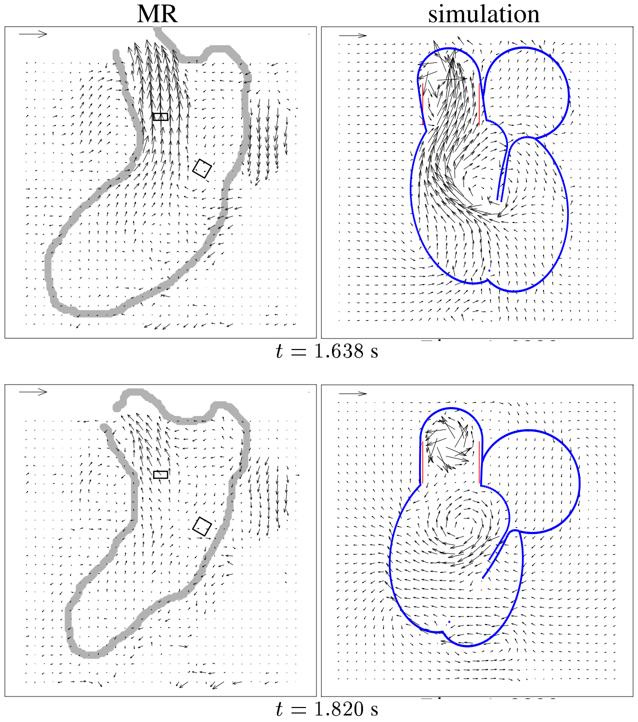

Figure 5.3: Velocity field and heart boundary from MR measurements (left) and reference simulation (right) at two times during a heart cycle characterized by: peak aortic outflow in MR data (top) and the time just before closure of aortic valve in MR data and just after aortic sink closure in simulation (bottom).

inflow typically has two peaks during a heart cycle, the early peak, also referred to as the E peak, and the late atrial peak, referred to as the A peak. (In the second heart cycle of the simulation, though, three peaks are seen. We discuss this below). In Figure 5.1 at the time of the E peak (1.066 s), a wide inflow jet is seen in both MR data and simulation. In the MR data the jet is wider and reaches deeper into the ventricle compared to that of the simulation. In both the MR data and simulation, the beginning of formation of a vortex is seen at the leaflet tips, the anterior vortex is clearly seen in the simulation. (The leaflets are not shown in the MR data). In the simulation a vortex is already present deeper in the ventricle,

this vortex was formed in the first heart cycle and not destroyed.

Mid diastole. In the MR data and simulation at 1.170 s (Figure 5.1), the inflow has decreased and in the simulation semi-closure of the mitral valve is seen. Also, the flow pattern in the MR data suggests that the mitral valve is in a semi closed position. In the MR data a large vortex has developed in the anterior part of the ventricle, while there is only a hint of a posterior vortex. The flow pattern is similar in the upper part of the ventricle in the simulation: two vortices are clearly seen, a large anterior vortex and a smaller posterior one. But in the lower part of the ventricle, close to the apex, a third ventricle is also present. At 1.274 s (Figure 5.1) the inflow has further declined in both MR data and simulation, but the vortices are still present at lower angular velocity. In the MR data the posterior vortex is hardly detectable.

Late filling. At 1.391 s (Figure 5.2) the inflow through the mitral ring in the simulation has increased, and the third peak (the A peak) of the mitral inflow is on its way. This, of course, should have been the second peak, a point that is discussed in Section 5.3. In contrast, only a hint of the A peak is seen in the MR data. The presence of the anterior vortex in the MR data is rather vague at this time, while it is still clear in the simulation, along with both the posterior and apical vortices. No posterior vortex is detectable in the MR data.

Mitral valve closure. In both the MR data and simulation, the mitral valve is closing at 1.495 s (Figure 5.2). The mitral valve is not shown explicitly in the MR data, but the flow pattern reveals that the valve is closing. In the MR data a rotational flow pattern filling up the ventricle is discernible, but it is not a clear vortex, while in the simulation both the anterior and posterior vortices are still present. The apical vortex is hardly detectable.

Ventricular systole. The early aortic outflow pattern near the outflow tract at 1.560 s (Figure 5.2) is similar in the MR data and the simulation. Deeper in the ventricle the velocities are higher in the simulation than is apparent from the MR data. Furthermore, the flow from most of the ventricle in the simulation converges toward the outflow tract. Based on the position of the heart wall of the ventricle in the simulation (when compared to the previous time frame), it is seen that the ventricular systole has set in. This is not clear from the heart wall position in the MR data, but since aortic outflow is present the ventricular systole must have started. In Figure 5.3 at 1.638 s the aortic outflow velocity has increased in both MR data and simulation. From the velocity profiles shown in the following section it can be seen that this is the time of peak aortic outflow velocity according to the MR data and just after peak velocity according to simulation. The converging of the ventricular flow toward the outflow tract from most parts of the ventricle is still most clearly seen in the simulation. In the simulated flow field the artificial termination of the outflow tract causes a backflow along the anterior side of the tract and the formation of a vortex.

End of systole. The flow pattern at 1.820 s (Figure 5.3) shows that the aortic valve is still open in the MR data, but the aortic sink is closed in the simulation. From the velocity profiles in the following section it is seen that this is just before valve closure according to the MR data and just after valve closure in the simulation. The vortex seen in the outflow tract of the simulation is of course an artifact of the model, and the ventricular vortex seen in the simulation will affect the flow pattern of the following heart cycle, as we saw in the first time frames (Figure 5.1) of this heart cycle.

The above comparison between the velocity fields from the MR measurements and the simulation shows a reasonable agreement in the general flow pattern. A difference in velocity fields is seen in the width of the inflow jet (from atrium to ventricle). The flow patterns also differ with respect to the size of the ventricle, the ventricle in the simulation being larger than in the MR data. This is a consequence of the model being 2D. The entire expansion takes place in the considered plane, and to produce the right outflow the ventricle has to expand more. The larger ventricle might be an explanation for the clearer formation of a posterior vortex and the more prominent anterior vortex in the simulation.

The flow fields from the simulation are affected by the simple aortic valve (sink coupled through a diode to a Windkessel model). Together with the termination of the outflow tract, the aortic sink results in the formation of a vortex at the sink, which of course is not seen in the MR data. Furthermore, the tethering of the model heart has eliminated the excessive movement of the heart, but it has also introduced oscillations in both the atrium and the ventricle (see Section 4.4) and this affects the flow field in an unphysiological way. The oscillations of the atrium can be seen when comparing successive plots of the heart wall. This is not seen in the plots shown here because they are too far apart in time. The oscillations of the ventricle are best seen when an animation of the pictures is performed. In addition, the tethering restricts the model to movements along the axis of the outflow tract. Together with the dynamics of the mitral ring (variation in length), the restriction due to the tethering results in the ventricle axis being almost aligned with the axis of the outflow tract instead of having the angle we introduced in the initial geometry.

The papillary muscle (modelled by a link between a virtual point inside the left ventricle and a point on the posterior heart wall) results in an unphysiological shape of the apex of the left ventricle (see Figure 5.2 at $t = 1.560$ s). This distortion affects the flow pattern and makes the agreement less good.

In our earlier reported comparisons between model and MR data (Adeler and Jacobsen, 2001; Jacobsen et al., 2001) we moved the tethering point of the papillary muscle to the ventricular wall up along the posterior wall to prevent the formation of the posterior vortex. But this resulted in a very strong (and unphysiological) contraction of the posterior wall and in a very asymmetric movement of the mitral valve. Regarding the work described in this thesis, it was decided that the mitral valve movement and the contraction of the ventricle were more important than the formation of the posterior vortex. Therefore we now tether the papillary muscle to a point a little bit up along the anterior wall, as described in Section 3.3.7. This decision was particularly made with the simulations for Chapter 6 in mind.

Generally, we have obtained a geometry which is more correct compared to a human left ventricle than that in the original model, but the geometry is still simplified. We have achieved a correct length scale of the left ventricle by changing the diameter of the mitral ring and the diameter of the outflow tract.

The changes of the cross links improved the control of the movement of the ventricle wall during the heart cycle, thus changing the almost circular form of the ventricle in the original model to the more realistic elongated form in the present model.

With this set of modifications, which must be considered as minimal, we of course did not obtain (nor did we expect to) a close match between the simulated and measured heart wall geometries during the various phases of the heart cycle.

5.3 Velocity time profiles

From the velocity fields of both the MR data and simulation we can extract velocities at chosen spatial positions. For the MR data we only have 26 times over a heart cycle where we can extract velocity information, whereas for the simulation we have 29952 times.

Apart from the purpose of comparing the velocity at chosen spatial positions, the velocity profiles can also be used to evaluate the timing of the simulation compared to MR measurements. We have no exact measurements of the time of onset and the duration of ventricular and atrial systole (see Section 3.3.6) due to the limited quality of the ECG during the MR scan, but by comparing the velocity profiles the timing parameters can be evaluated.

The in- and outflow velocity profiles from the MR data are obtained by averaging the velocity over 2 fixed voxels at the centre of the left ventricular outflow tract at the level of the aortic valve, and over a square of 4 fixed voxels near the centre of the mitral ring. These voxel are indicated in the velocity field plots in

Figures 5.1–5.3. At the outflow tract the vertical component is recorded (see reference frame in Figure 5.1), while at the mitral ring it is the component making an angle of 30° with the vertical. Because of the small movement of the heart wall, no attempt is made to trace the movements of the heart in choosing these voxels and thus the velocities are computed with respect to a reference frame fixed in space. The extracted velocities are 'mean centre' velocities, which are a combination of a mean velocity over and a centre velocity at the relevant position. It would be difficult to compute the mean velocity over the entire outflow tract or over the entire mitral ring because the posterior wall is not known for the aortic outflow tract and the anterior border is not known for the mitral ring. It is also difficult to report the centre velocity (at one voxel) because the velocity oscillates from one voxel to the next over the aortic outflow tract. These are our reasons for reporting a mean centre velocity for the MR data.

For the simulation we report both a mean and a centre velocity (as described in Section 4.1) to be able to compare the mean centre velocity of the MR data with both types of velocities.

Figure 5.4 shows the time course of the inflow velocity at the mitral ring extracted from both the MR measurements and the simulation. Outflow velocities at the aortic outflow tract are shown in Figure 5.5. The matching of the simulation and MR data placed the R-peak in the ECG of the MR data at 1.486 s and this is indicated by a vertical dashed line in Figures 5.4 and 5.5.

Figure 5.4 shows that at the mitral ring there is a reasonable agreement between MR data and simulation results for both the centre and the mean velocity in the beginning of the heart cycle during early filling, but the early maximum (peak E) velocity is higher in the MR data than in the simulation (for both mean and centre values). It is obtained at the same time because of the matching of simulation and MR data. The upstroke of the E peak of the simulation results is very similar, while the downstroke is faster for the mean than the centre velocity, but both the upstroke and the downstroke match the MR data fairly well. The MR data shows negative flow velocity between the E peak and the A peak, and this is not seen in the simulation. On the contrary, the simulation shows a forward peak. This could be due to an incorrect movement of the mitral valve leaflets in the simulation, which might be caused by the three ventricular vortices, because the vortices affect the mitral valve movement. But the mitral valve movement is difficult to judge since it is not detected in the MR measurements. Alternatively, the peak could be caused by an incorrect activation level of the muscle model (see Section 3.3.6).

The A peak in the mitral inflow is caused by the onset of atrial systole. Atrial systole can be hard to detect in the MR measurements, because it occurs at the end

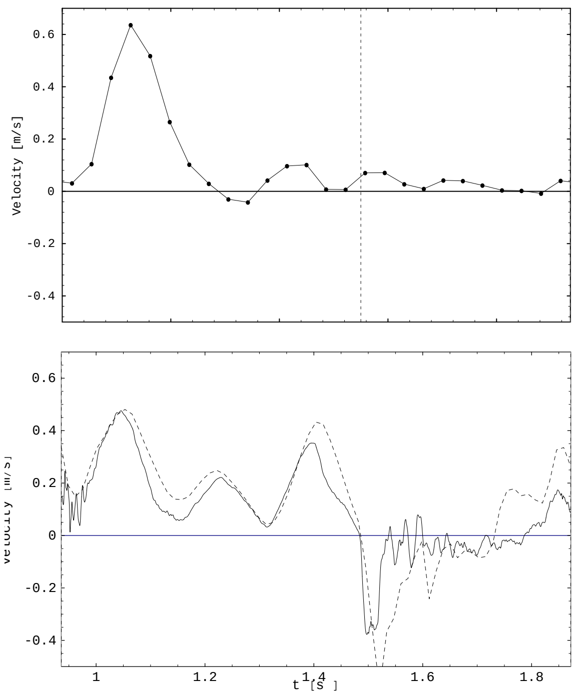

Figure 5.4: Velocity time profile for velocity (m/s) over the mitral ring from MR data (top) and from simulation (bottom). From the simulation both centre (dashed) and mean (solid) velocity is included.

of each MR recording. The last part of an MR recording will be smeared out because the final measurement is an average over 768 heart beats which each might vary in heart cycle length. This can explain why the peak A velocity (third peak in the simulation curves) is much higher in the simulation than in the MR data. As seen in Figure 5.4, the simulation shows a clear atrial systole. Although the measurements show only a very vague atrial systole, this occurs at approximately the same time in the simulation and MR measurements, confirming the timing of the atrial systole in the model. The MR data show no backflow at the time of closure of the mitral valve (between 1.494 and 1.530 s), in contrast to both velocities from the simulation. This could be a consequence of the averaging of the MR data, or it could be caused by the coarse time resolution in the MR measurements. In other

MR measurements (not shown) this displacement backflow has been clearly seen.

Figure 5.5 shows the velocity time profile across the aortic outflow tract from both the MR data and the simulation. It is seen that the outflow through the aortic tract starts at approximately the same time in the MR data and the simulation (for both velocities reported). Thus we can conclude that the onset of ventricular systole in the simulation is correct. The form of the curve is much wider for the MR data, but the outflow through the tract ends at approximately the same time in both the MR data and the simulation. The maximum outflow velocity is obtained earlier in the simulation than in the MR data, suggesting that the onset of ventricular diastole could be further improved.

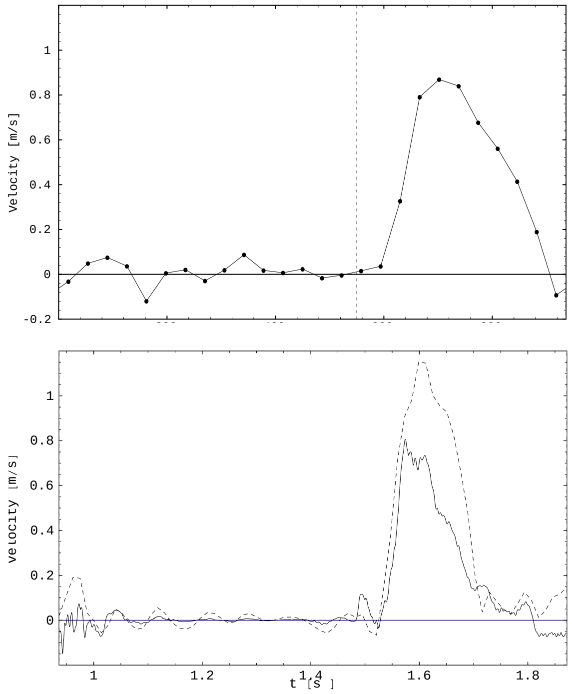

Figure 5.5: Velocity time profile for velocity (m/s) across the aortic outflow tract from MR data (top) and from simulation (bottom). From the simulation both centre (dashed) and mean (solid) velocity is included.

A primary effect of the use of the Windkessel model is that we obtain a simulated aortic outflow profile which reproduces a characteristic feature of the measured one, namely that the upstroke has a duration of about one half of that of the downstroke. As mentioned above, the actual shape of the simulated outflow curve does not exactly match the measured one. Further adjustment of the load parameters might achieve a better agreement, but the muscular model behind the heart model is also involved in the simulated profile and therefore should be involved in the tuning process as well. It was also found that the shape of the outflow profile was sensitive to the strength and geometry of the tethering.

It should be noted that in the previously reported comparisons between model and MR data (Jacobsen et al., 2001; Adeler and Jacobsen, 2001) results from the first heart cycle were compared with the MR data and several of the parameters were adjusted to achieve a good comparison between the first heart cycle and the MR data. When we later investigated which heart cycle best represents a periodic result from the model (see Section 4.7), we did not change the parameter settings for the model, and this explains why the comparison presented here is not as good as the one we have previously reported. The model could be further adjusted to make the second heart cycle better compared to MR data. Unfortunately, time has not allowed us to do this.

5.4 Discussion and conclusions

The comparison of the velocity fields from the MR measurements and the simulation shows a fair qualitative agreement in the general flow pattern: a wide inflow jet, the formation of a dominant anterior vortex filling the ventricle, and an outflow jet in the aortic outflow tract. A difference in velocity fields is seen in the width of the inflow jet (from atrium to ventricle) and in the size of the ventricle. Comparison of the vortex patterns in the middiastolic phase could indicate that a more complex 3D flow pattern is present in the measured ventricle than that predicted from the simple 2D model. This is supported by results from the 3D model presented in Chapter 7. In the 3D model we see that a vortex ring is formed during filling (see Figure 7.6), and when looking at this vortex ring in a cut-away view (Figure 7.7) it has the shape of two vortices, similar to those seen in the 2D model. Further, the simulation shows three vortices in the ventricle, whereas the MR data shows at most two. The third vortex is a result of the vortex in the previous heart cycle not being destroyed before the onset of diastole. In the MR data no vortex is present at the end of a heart cycle. The third vortex in the simulation is unphysiological, and it would improve the model considerably if it could be removed. Removing this vortex might improve the movement of the mitral valve and consequently also remove the third peak in mitral velocity profile.

Generally, we see that the vortex pattern is more distinct in the simulation and the velocities in the vortices are larger. This is partly related to the form of the ventricle and the mitral valve motion in the simulation. Because the model is 2D, ventricular expansion has to take place in the considered plane, resulting in an oversize ventricle. Furthermore, the ventricle is still too circular in form, even though we have improved this by adjusting the cross links. The motion of the mitral valve is not completely correct; it should open up more and the posterior leaflet should actually touch the posterior ventricular wall. The latter would probably prevent the formation of the posterior vortex.

The flow fields from the simulation are affected by the simple aortic valve (diode coupled to sink), resulting in the formation of a vortex at the sink, which of course is not seen in the MR data. Furthermore, the tethering of the model heart introduces oscillations in both the atrium and the ventricle and this affects the flow field in an unphysiological way.

The time of atrial systole seems to be set reasonably well in the model, but this is difficult to judge because of the very vague atrial systole in the MR data. The onset of ventricular systole seems to be right, while it would probably improve the model if the duration of ventricular systole was extended, thus leading to a later onset of ventricular diastole.

The velocity profiles at the mitral ring and aortic outflow tract from simulation and MR measurements match reasonably well. The timing of the velocity profiles is in good agreement, whereas the shape and maximum values of the velocity curves show some difference. The best agreement for the mitral velocity profile is in the beginning of the heart cycle, while the best agreement for the aortic profile is from the beginning until maximum outflow velocity.

The dependence of the simulated results on the various parameters in the model is very complex, and we are sure that a further adjustment of the parameters could lead to an even better agreement between simulated and measured velocity data. Parameters of particular importance in this regard are the duration of ventricular systole, the excitation and relaxation parameters, and the Windkessel and muscle parameters. However, the comparison shows that despite the geometrical constraints posed by the 2D modelling of a 3D phenomenon, a reasonable agreement is obtained between simulated and measured results.

The comparison supports the concept of combined simulation and MR studies to investigate the flow in the heart and its interaction with the structure and function of heart muscles and heart valves, provided that the limits of the model are kept in mind. The detailed flow inside the heart should not be used for investigations before the model is improved, especially with respect to the vortex pattern. Based on the comparison between the mitral velocity profiles, it is justified to use the model to investigate the early filling of the ventricle, particularly the influence on the mitral velocity profile. Investigations involving the aortic outflow velocity profiles would also be justified. Experiments involving the overall response of the heart to different scenarios is yet another possibility, e.g. how does the heart react to an increased resistance in the outflow, what happens if part of the ventricular wall grows stiffer or what are the consequences of a decrease in papillary muscle tension? In answering these questions one should not expect to obtain the complete flow field inside the heart, but rather such quantities as the cardiac output, the form of the outflow velocity profile, or the influence on the filling of the ventricle.

Chapter 6

Simulating pathological heart conditions

An important purpose of our work with the 2D model is to use it to study the influence of pathological conditions in the heart, specifically conditions which can be related to the mechanical activation of the heart muscle.

The blood flow pattern changes when a patient suffers from a heart disease, resulting in e.g. a decrease in the ejection fraction or a reduced filling velocity. Mechanisms involved in heart diseases have been investigated by the use of different measuring techniques (one of them being MR). This has led to the definition of indexes of the blood velocity to characterize the left ventricular diastolic function. Several studies have focused on the early diastolic filling, and since we have found a reasonably good comparison between the model and MR data in exactly the early filling phase, the mechanisms responsible for the change in flow pattern and the velocity indexes can be studied in the computer model. However, to be able to simulate pathological conditions, it is necessary first to refine the model for the activation of the heart muscle. The improved model can then be used to study some general mechanisms involved in heart diseases.

This chapter begins with the medical background for improving the model for the activation of the heart muscle and describes the implementation of the improved activation function. The model parameters are then set up to simulate a healthy human. Using these model parameters we make an investigation of some of the mechanisms involved in heart diseases and compare simulations of a diseased heart with MR measurements.

6.1 Medical background

In most heart diseases diastolic dysfunction often coexists with systolic dysfunction. The assessment of diastolic function, or, more precisely, the assessment of left ventricular diastolic function, has been given much attention (Houlind, 2001b; Nishihara et al., 2000; Ohte et al., 1999; Steine et al., 1999; Stugaard et al., 1994a; Stugaard et al., 1994b; Stugaard et al., 1993; Yamamoto et al., 1995; St. Goar et al., 1991). As a results of recent progress the intraventricular blood flow pattern and derived blood velocity indexes can now be used to evaluate the state of the diastolic function. The intraventricular blood flow pattern changes in a diseased heart, but at present the mechanisms responsible for this change are not completely understood. The computer model is a tool for studying these mechanisms.

The diastolic function can be evaluated e.g. by measuring the pressure, the wall thickness, the wall motion or the blood flow/velocity. Naturally, we have focused on comparing the model with studies of the diastolic function that are based on the blood flow pattern or blood flow velocity. These studies are performed using MRI or echocardiography (e.g. colour M-mode Doppler technique). We look at the general flow pattern during early filling and we compare computed and observed velocity indexes derived from the intraventricular velocity field.

6.1.1 Mechanisms during early filling

In the normal state of early left ventricular filling, the rapid left ventricular relaxation generates a pressure gradient in the left ventricle with the highest pressure at the base and the lowest pressure at the apex. The pressure gradient drives the blood entering at the mitral valve toward the apex of the ventricle (Houlind et al., 2001). In the diseased heart with diastolic dysfunction the left ventricular relaxation is slowed and the intraventricular pressure gradient is reduced (see e.g. Steine et al., 1999). So, regional differences in relaxation rate affect the early diastolic function. The reduced intraventricular pressure gradient tends to cause a slower propagation of the blood flow into the ventricle (Houlind et al., 2001).

6.1.2 Pathological heart conditions

There exist several studies of the diastolic function, covering a range of heart diseases, that provide data that can be used to determine appropriate input parameters to the model and to compare with simulation results. This section gives a brief description of some important heart diseases and their influence on the diastolic function.

Ischemic heart disease is a common term for inadequate blood supply to an area of the heart wall. If this is due to blockage of the coronary arteries it is called coronary artery disease, see below. Ischemia can be both local and global. In the case of global ischemia the filling of the ventricle is delayed (Stugaard et al., 1994b). Local ischemia is often seen in an acute infarction (Kim, 2001), see 'Acute myocardial infarction' below.

- **Coronary artery disease (CAD)** is the narrowing of the coronary arteries caused by atherosclerosis. A coronary artery is an artery that supplies blood to the heart muscle. Relaxation is often prolonged during this illness (Weiss et al., 1976; Ohte et al., 1999) and the filling of the ventricle is delayed (Stugaard et al., 1994a; Stugaard et al., 1993).
- **Acute myocardial infarction (AMI)**, often referred to as a heart attack, is the death of part of the heart muscle due to a sudden loss of blood supply. The loss of blood supply is caused by the complete blockage of a coronary artery by a blood clot. AMI affects the motion and the relaxation of the diseased part of the heart wall. Typically, the motion of the heart wall is abnormal and both the relaxation and the filling of the ventricle is delayed (Steine et al., 1999). Furthermore, lower filling peak velocities are seen (Steine et al., 1999; Houlind et al., 2001).

Cardiomyopathy is a general term for a disease of the heart muscle (the myocardium).

- **Hypertrophic cardiomyopathy (HCM)** is characterized by increased growth (hypertrophy) in the thickness of the left ventricular wall. In this case the ejection fraction (see Section 2.2) is often not affected, but the relaxation is prolonged (Nishihara et al., 2000).
- **Dilated cardiomyopathy (DCM)** is characterized by a dilated ventricle. This is often seen in chronic heart failure, where a global dilation of the ventricle is present and the relaxation is abnormal (Kim, 2001). In the case of DCM the ejection fraction is decreased and the filling of the ventricle is abnormal (Houlind, 2001a; Yamamoto et al., 1995; St. Goar et al., 1991). It is not clear whether the abnormal filling is caused by diastolic or systolic dysfunction of the ventricle (Yamamoto et al., 1995).

6.1.3 Velocity indexes

The diastolic function can be determined by investigating (spatial) velocity profiles along lines across the left ventricle, i.e. velocity profiles along lines perpendicular to the long axis of the ventricle, at different times during the early inflow. This has been done using both MRI (Houlind et al., 2001) and pulsed Doppler echocardiography (Steine et al., 1999; Yamamoto et al., 1995). Typically 3-6 lines are examined.

We present here the method of Houlind et al. (2001), where six lines are examined during an MR scan. One line is placed at the level of the mitral leaflet tips (MLT) perpendicular to the inflow jet. The other lines are placed parallel to the first line but displaced either upstream or downstream of the first: one line is placed 2 cm upstream (approximately at the level of the mitral ring), and lines are placed 1, 2, 3 and 4 cm downstream. These lines are fixed in space and do not move with the heart. This is acceptable because the motion of the heart is small during diastole. Along each of these lines the absolute velocity is computed based on all three velocity components, and the spatial velocity profile is plotted. The inflow jet is manually traced and all velocities outside the jet are set to zero. The velocity profiles are examined at 5 times: the time of E peak velocity at the mitral leaflet tips, the time frame prior to this, and the three subsequent time frames. The time difference between succeeding time frames are of the order of 25 ms.

From the velocity profiles three quantities can be derived that characterize the ventricular diastolic function (Houlind et al., 2001). These are the peak velocity (PV), the velocity index (VI), and the time delay (TD). PV is the maximum velocity (in both space and time) at a particular line. VI for a particular line is computed as the PV at that line relative to the PV at the line at the mitral leaflet tips. Finally, TD is calculated as the time difference between time of occurrence of PV in a particular line and time of occurrence of PV at the line at the mitral leaflet tips.

Figure 6.1 shows the velocity profiles from a healthy person along the six lines at five times: 27 ms before PV at the mitral leaflet tips, at the time of PV at the mitral leaflet tips, and 27, 54 and 81 ms after the time of PV at the mitral leaflet tips. It is seen that the velocity profiles are wider and lower for the lines closest to the apex (the 2, 3 and 4 cm lines). Furthermore, the figure shows that PV is obtained almost at the same time at all the lines.

In Houlind et al. (2001) PV, VI and TD are given for a group of healthy persons and for a group of AMI patients. Figure 6.2 shows the PV at the six lines from the healthy group and the AMI group. The data are plotted as the mean values with the standard deviation shown as error bars. From this figure it is clear that

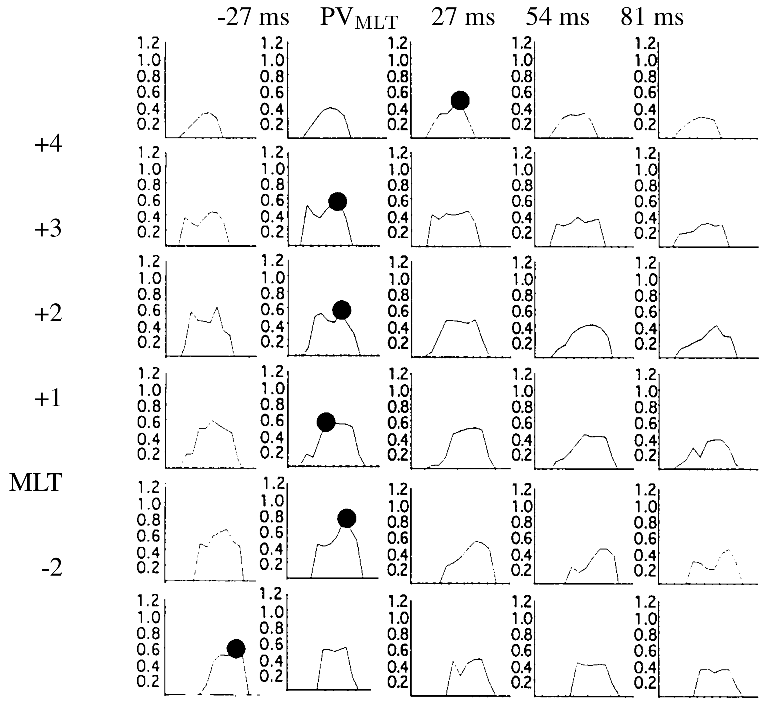

Figure 6.1: Velocity profiles of absolute velocity (m/s) along six lines at five times from a healthy person obtained by MRI. Peak velocity in each measuring position is marked by a •. From Houlind et al. (2001).

the peak velocity at all lines are lower in an AMI patient than in a healthy person. PV is only significantly lower (from a statistical point of view) at the 3 and 4 cm lines (Houlind et al., 2001).

Figure 6.3 shows the velocity index, VI, at the six lines from the healthy and the AMI group. The figure shows that close to the apex (at the 3 and 4 cm lines) VI is lower in the AMI patients than for the healthy group. In Figure 6.4 the time delay, TD, at the six lines is shown. TD is markedly higher closer to the apex (at the 3 and 4 cm lines) for the AMI group than for the healthy group. All these figures (Figures 6.1–6.4) show that in AMI patients the filling pattern during early diastole in the lower part of the ventricle is changed compared to healthy persons: the filling is delayed, peak velocities are lower and the peak velocity at MLT is not maintained downstream of MLT.

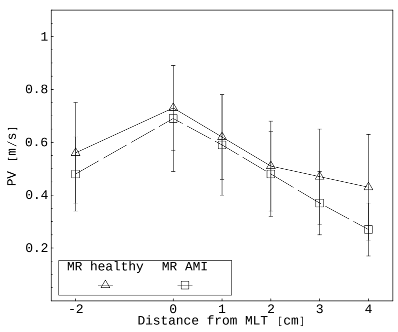

Figure 6.2: Peak velocity (PV) at six lines from MR measurements of healthy persons (△) and AMI patients (□). Data are shown as the mean value with the standard deviation (SD) as error bars.

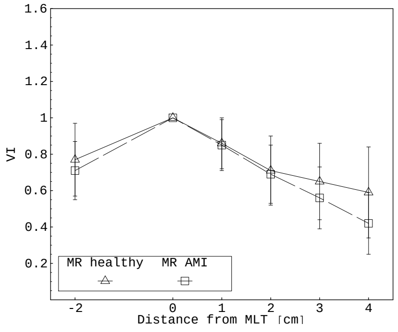

Figure 6.3: Velocity index (VI) at six lines from MR measurements of healthy persons (△) and AMI patients (□). Data are shown as the mean value with the standard deviation (SD) as error bars.

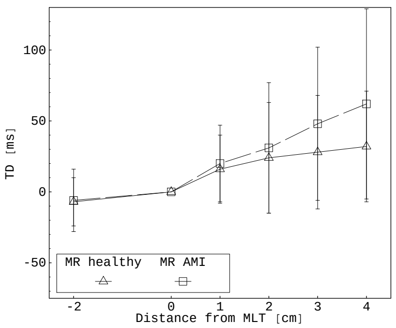

Figure 6.4: Time delay (TD) at six lines from MR measurements of healthy persons (△) and AMI patients (□). Data are shown as the mean value with the standard deviation (SD) as error bars.

6.1.4 Time constant of relaxation

The relaxation of the left ventricle is closely related to the pressure there. Weiss et al. (1976) showed that during isovolumic relaxation the pressure-time variation follows an exponential decay ($e^{-t/\tau}$) with a certain time constant τ, and τ has subsequently been used as an index for the relaxation. The measured pressure-time variation during isovolumic relaxation is fitted to an exponential decay to determine the time constant τ.

Pressure is measured by invasive methods (not MRI). The pressure measurements can be done at several points in the ventricle, thus making it possible to obtain τ for different regions in the ventricle. Typically, τ is determined for the basal and apical parts, see e.g. Steine et al. (1999).

6.1.5 Regions of the ventricle

In studies of the left ventricle the ventricular wall is divided into five regions of approximately the same size (Schroeder, 1999): the basal half of the anterior wall region (AB), the apical half of the anterior wall region (AA), the apical region (A), the apical half of the posterior wall region (PA), and the basal half of the posterior wall region (PB). The five regions are shown on an MR image in Figure 6.5.

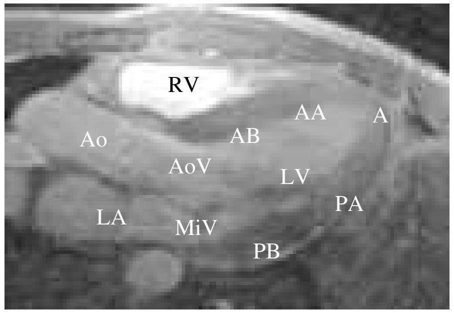

Figure 6.5: MR image with the five regions of the ventricular wall indicated: AB: basal half of anterior wall, AA: apical half of anterior wall, A: apex, PA: apical half of posterior wall, PB: basal half of posterior wall. Furthermore, the position of the left ventricle (LV), the left atrium (LA), the right ventricle (RV), the mitral valve (MiV), the aortic valve AoV and the aorta (Ao) are indicated.

6.2 The new activation function

The previous section showed that in a diseased heart the relaxation of the heart muscle is often affected. The relaxation of the heart wall can easily be controlled and changed in the model through manipulation of the parameters determining the activation function.

In the original model, the parameters that determine the relaxation and contraction of the heart wall (the parameters in the activation function α) are defined separately for the atrium and ventricle. To be able to simulate regional differences, which is necessary in the pathological cases above, the parameters have to be regionally given rather than given for each heart chamber as a whole. This is achieved by dividing the heart wall into five regions, similar to the ones described in Section 6.1.5. The parameters determining the activation function are then defined within each region. These parameters are the relaxation and excitation, or contraction, time constants K_r and K_e, the limiting and initial values of the activation function α_{max} and α^0, the onset time of systole t_s and the end time of systole $t_{s,end}$ (which is also the onset time of diastole). We call this refinement of the activation function a regional activation.

In addition to making it possible to simulate pathological conditions, we wish to improve the activation function from a general physiological point of view. The activation function $\alpha(t)$ gives the time course of contraction and relaxation of the heart muscle. $\alpha(t)$ is a model for the release of Ca^{2+} (Peskin, 2001), which initiates the mechanical contraction of heart muscle (see Section 2.4). The release of Ca^{2+} is triggered by the action potential, which is propagated through the conduction system of the heart. Since the contractile response of a cardiac muscle begins just after the action potential has reached the muscle fiber, the contraction also propagates as a wave over the heart wall with the same velocity field as the electrical impulses. But this is not how the contraction and relaxation are implemented in the original model.

In the original model the contraction of the heart wall occurs simultaneously in the entire atrium and, after a delay, simultaneously in the entire ventricle, because t_s is the same for the entire atrium and for the entire ventricle. The same holds for the relaxation in the original model, because also $t_{s,end}$ is the same for the entire atrium and for the entire ventricle. Changing to a regional activation would still not be physiologically correct, because t_s and $t_{s,end}$ would be the same within each region. The physiologically correct way to model the time course of contraction and relaxation is to let the contraction and relaxation propagate over the heart wall with a finite velocity. With respect to the model, this means that the onset time of systole t_s and the end time of systole $t_{s,end}$ are given individually

for each link in the heart and not for a group of links together. This improvement of the activation function we call a gradual activation.

The gradual activation affects the timing of the contraction and relaxation, while the regional activation affects both the timing and the rate of contraction and relaxation. The gradual and regional activations are not complementary processes but can be used together or separately. If they are used together, the timing is determined by the gradual activation, and the rate of contraction and relaxation are determined by the regional activation.

6.2.1 The original model

In this section we briefly repeat how the activation function is defined in the original model.

In diastole the governing equation for the activation function $\alpha(t)$ is (see Section 3.3.6)

$$\frac{d\alpha}{dt} = -K_r\alpha$$

with the analytic solution

$$\alpha(t) = \alpha(t_d)e^{-K_r(t-t_d)}$$

where K_r is the relaxation rate constant and t_d is either the onset time of diastole or the starting time of the simulation.

In systole the governing equations are (see Section 3.3.6)

$$\frac{d\alpha_*}{dt} = K_e(\alpha_{max} - \alpha_*), \qquad \frac{d\alpha}{dt} = K_e(\alpha_* - \alpha)$$

with the analytic solution

$$\begin{aligned} \alpha_*(t) &= \alpha_{max} - (\alpha_{max} - \alpha_*(t_s))e^{-K_e(t-t_s)} \\ \alpha(t) &= \alpha_{max} - (\alpha_{max} - \alpha(t_s))(1 + K_e(t-t_s))e^{-K_e(t-t_s)} \end{aligned}$$

where K_e is the excitation rate constant, α_{max} is the limiting value of the activation function and t_s is the time of onset of systole. The equations are solved with a common initial value for the auxiliary function α_* and the activation function α: $\alpha_*(t_s) = \alpha(t_s)$.

The six parameters that determine the time course of the activation function are: K_r, K_e, α_{max}, $\alpha^0 = \alpha(t=0)$, t_s time of onset of systole and $t_{s,end}$ time of end of systole (which is equal to t_d the time of onset of diastole). There is one set of parameters for the links in the atrium, one for the links in the ventricle and one for the papillary muscle link. The only distinction between the set for the ventricular links and that for the papillary muscle link is the initial value α^0. The values of the parameters are listed in Table 3.1 in Section 3.3.6.

6.2.2 The new implementation

The core of the new implementation of the activation function α is that this function including the six parameters K_r, K_e, α_{max}, α^0, t_s and $t_{s,end}$ are defined separately for each link in the heart boundary.

Gradual activation

In the code of the original model, the activation function was given by three variables: A, V and C, representing the activation function in the atrium, ventricle and papillary muscle (chord), respectively. These variables are now defined as arrays with index IX: $A(IX)$, $V(IX)$ and $C(IX)$, where IX is an index to the link. Each of these variables holds only values of links in its own domain, e.g. for $A(IX)$ we deal only with indexes IX to links that are part of the atrial heart boundary.

The two parameters affected by the gradual activation t_s and $t_{s,end}$ were originally defined as constant variables for the three groups atrium, ventricle and papillary chord, respectively. They are now, similarly to A, V and C, defined as arrays with index IX, e.g. the time t_s of onset of atrial systole, which used to be the variable NTA, is now $NTA(IX)$.

We set up two chains of links, one for the atrium, $LNKCYCA$, and one for the ventricle, $LNKCYCV$. These variables holds the index, in a geometrically natural order, to all the links in the atrium and ventricle, respectively. By geometrically natural order we mean that $LNKCYCA(i)$ and $LNKCYCA(i+1)$ hold indexes to neighbouring links on the heart boundary. Figure 6.6 shows how the two chains are set up. Each cross link in the ventricle is numbered directly after the link along the right (posterior) boundary with which it has a common boundary point.

We define a starting link ($IXSA$ and $IXSV$) for each of the chains, i.e. $IXSA$ and $IXSV$ are the numbers of the links where the wave of contraction or relaxation starts in each chain, respectively. For physiological reasons the starting link in the atrium should be at the position of the SA node and the starting link in the ventricle should be at the position of the AV node (see Section 2.3).

Next, we prescribe a velocity V with which the activation should propagate over the heart boundary. The velocity does not have to be the same for the atrium

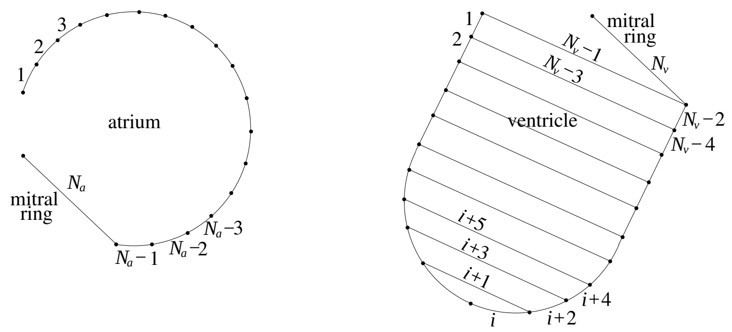

Figure 6.6: Illustration of the numbering of the links in the two chains in the atrium (left) and the ventricle (right). N_a and N_v are the total number of links in the chains, respectively. Note, the mitral ring is modelled by two links, one in each of the chains.

and the ventricle, nor does it has to be the same for all links in either the atrium or the ventricle. In the following we introduce at propagation velocity for the atrium $V = V_a$ and a propagation velocity for the ventricle $V = V_v$. Theoretically the propagation velocity should be equal to the velocity of conduction of the electrical impulses in the heart (see Section 2.3).

To implement the gradual activation function, the parameters t_s and $t_{s,end}$ should be set for each link according to the link's spatial position at time $t = t_s$ and $t = t_{s,end}$. However, to simplify the calculations we compute t_s and $t_{s,end}$ according to the initial position of the link. That is, first we set t_s and $t_{s,end}$ for the starting link ($IXSA$ and $IXSV$) in each chain. Then, based on the propagation velocity and the distance between links in the initial heart configuration, we compute t_s and $t_{s,end}$ for the rest of the links in each chain. The general formula for the onset time of systole t_s for a link IX is

$$t_s(IX) = t_s(IX_{start}) + \frac{\mathrm{dist}(IX)}{V}$$

where IX_{start} is either $IXSA$ or $IXSV$, V is the propagation velocity and $\mathrm{dist}(IX)$ is the distance between link IX and the starting link (either $IXSA$ or $IXSV$).

Typically, we have that the distance $\mathrm{dist}(IX)$ is of the form $|IX - IX_{start}| \cdot \Delta s^0$, where Δs^0 is the initial distance between neighbouring boundary points.

Thus

$$t_s(IX) = t_s(IX_{start}) + |IX - IX_{start}| \frac{\Delta s^0}{V}$$

We assume that the duration of systole $t_{s,dur}$ is the same for all links in the atrium and for all links in the ventricle (Ganong, 1993). Thus the general formula for the end time of systole $t_{s,end}$ is

$$t_{s,end}(IX) = t_s(IX) + t_{s,dur}$$

In the initial heart configuration the distance between neighbouring points is Δs^0. By computing the values for the links according to their initial positions, we get the right onset time of systole $t_s(IX)$ only if the distance between neighbouring points at $t_s(IX)$ is Δs^0. This condition does not hold, and we take that into account when we compute $t_s(IX)$.

For the atrium we know that at the onset of systole $t = t_s$ the distance between neighbouring points is $\Delta s^{t_s} = 0.5 \cdot \Delta s^0$, i.e. $\Delta s^0 = 2\Delta s^{t_s}$. So to assure the correct value of $t_s(IX)$ we multiply the propagation velocity in the atrium $V = V_a$ by 2. Thus the equations for the onset time of systole and end time of systole in the atrium are

$$\begin{aligned} t_s(IX) &= t_s(IXSA) + |IX - IXSA| \frac{\Delta s^0}{2 \cdot V_a} \\ t_{s,end}(IX) &= t_s(IX) + t_{s,dur} \end{aligned}$$

In the ventricle the distance between neighbouring points at the onset of systole $t = t_s$ is approximately $\Delta s^{ts} = 1.66\Delta s^0$, i.e. $\Delta s^0 = 0.6\Delta s^{t_s}$. Thus we need to multiply the propagation velocity in the ventricle $V = V_v$ by 0.6 to assure the correct value of $t_s(IX)$. The onset and end time of systole for all the links along the left (anterior) ventricular wall (called short links) are computed similarly to the links in the atrium, i.e.

$$\begin{aligned} t_s(IX) &= t_s(IXSV) + |IX - IXSV| \frac{\Delta s^0}{0.6 \cdot V_v} \\ t_{s,end}(IX) &= t_s(IX) + t_{s,dur} \end{aligned}$$

Here $t_s(IXSV)$ has been set to a value greater than t_s for the last link in the atrial chain, the difference being equal to the delay in the AV node (see Section 2.3).

For the short links along the right ventricular wall the principle is the same, provided we take into account that every second index is an index to a cross link.

Thus

$$\begin{aligned} t_s(IX) &= t_s(IXSV) + \frac{1}{2}|IX - IXSV| \frac{\Delta s^0}{0.6 \cdot V_v} \\ t_{s,end}(IX) &= t_s(IX) + t_{s,dur} \end{aligned}$$

Onset and end time of systole for each cross link in the ventricle are associated with the short links along the right ventricular wall. The values of t_s and $t_{s,end}$ for a cross link are identical to the values for the next short link in the ventricular chain, e.g. the short link with index $i + 2$ and the cross link with index $i + 1$ in Figure 6.6 have identical values of onset and end time of systole.

In summary we have that with the gradual activation the time course of the activation function is determined by the following parameters: the starting links $IXSA$ and $IXSV$, the onset times of systole for the starting links $t_s(IXSA)$ and $t_s(IXSV)$, the velocities V_a and V_v, and the duration times of systole $t_{s,dur}$ in the atrium and ventricle.

Regional activation

The regional activation function is introduced based on the wish to simulate regional differences in the ventricular activation, particularly in the ventricular relaxation. Hence, this improvement of the activation function affects only the activation function for the ventricular links. While the gradual activation affects only t_s and $t_{s,end}$, the regional activation affects all six parameters that determine the activation function, t_s, $t_{s,end}$, K_e, K_r, α_{max} and α^0.

We define five regions of the ventricular heart wall of approximately the same size: region 1 along the upper anterior wall, region 2 along the lower anterior wall, region 3 along the apex, region 4 along the lower posterior wall and region 5 along the upper posterior wall. Figure 6.7 shows the five regions at the initial time. The regions correspond to the five regions presented in Section 6.1.4. The papillary muscle link belongs to region 3.

In each of the five regions all the parameters (t_s, $t_{s,end}$, K_e, K_r, α^0 and α_{max}) determining the activation function are fixed. Thus if we choose regional and not gradual activation, the values of t_s and $t_{s,end}$ are the same within each region. It is also possible to have both regional and gradual activation at the same time. In this case t_s and $t_{s,end}$ are given by the gradual activation process and the remaining four parameters are determined by the value for the given region. We give the values for the papillary muscle link independently of the region values, assuming conditions where the papillary muscle activation is not affected by the heart disease.

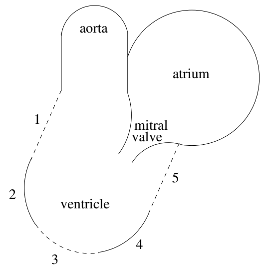

Figure 6.7: The five regions of the ventricular heart wall at initial time.

6.2.3 Time constant of relaxation

In Section 4.1.3 we found a close relation between the time course of the activation function α and the time course of the ventricular pressure, particularly from the beginning of relaxation until the mitral valve opens (see Figure 4.7). Furthermore, the previous sections show that during relaxation α is described by an exponential decay of the form $e^{-K_r t}$. This supports the use of a pressure-determined index (the time constant τ of an exponential decay during relaxation) for the evaluation of the relaxation, as described in Section 6.1.4. Hence, assuming that $\tau = 1/K_r$, we can use measurements of the time constant τ to determine K_r in the activation function.

6.3 Calibrating the model

The parameters determining the two improvements of the activation function (gradual and regional activation) are set up to match a healthy human by comparisons with MR data and calibrations based on physiological knowledge.

6.3.1 Velocity profiles along transverse lines

In addition to the typical output from the model (see Section 4.1) we also look at spatial velocity profiles (of absolute velocity) along transverse lines in the ventricle by a method similar to that used by Houlind et al. (2001) for MR data during the early filling phase. We described that method in Section 6.1.3. Since we are only interested in the diastolic filling phase, we only investigate the velocity profiles during diastole, but we investigate them for a longer time period and at

smaller time intervals (approximately 13 ms) than done in Houlind et al. (2001).

When we investigate the results from the six lines, we look at the spatial velocity profile along each of the lines at different times and compute PV, VI and TD for each of the lines (see Section 6.1.3 for a definition of these quantities). Because we investigate the lines for a longer time period than done in Houlind et al. (2001) we are able to find higher values of TD.

In Houlind et al. (2001) the lines are fixed in space, and this is reasonable because the motion of the heart is relatively small. However, in the model the heart motion is more pronounced. Therefore we examine the difference between results from lines fixed in space and results from lines following the heart motion.

The lines fixed in space are set up similarly to the method for the MR data: at the time of peak velocity between the leaflet tips a line is placed at the level of the mitral leaflet tips (MLT) but perpendicular to the inflow jet. Another line is placed parallel to the first one but displaced 2 cm upstream, approximately at the level of the mitral ring. Furthermore, 4 lines are placed parallel to the first line but displaced 1, 2, 3 and 4 cm downstream. The top row of Figure 6.8 shows the velocity field, the heart boundary and the six lines at two times during the first cycle of a simulation where the lines are fixed in space.

For the lines following the heart motion we take, at each time step, the mitral ring as the basic line, because this is a well defined line in the model and the flow is practically perpendicular to this line. Then we place 5 lines parallel to this line but displaced 2, 3, 4, 5 and 6 cm downstream, see bottom row of Figure 6.8. The line 2 cm downstream of the mitral ring is approximately at the level of the mitral leaflet tips and we thus denote it MLT.

The comparison between the results obtained at lines fixed in space and lines following the heart motion reveals that even though we only look at diastole (where the motion is less than in systole), the heart motion is too great to obtain reasonable results from the lines fixed in space. E.g. the line positioned 1 cm downstream of the mitral leaflet tips moves above the level of the mitral leaflet tips, and the line at the mitral ring is positioned in the middle of the atrium, see top right picture in Figure 6.8. Thus we conclude that we should choose lines following the heart motion.

Since the lines that follow the heart motion are based on the line at the mitral ring and not on a line positioned perpendicular to the inflow jet, we cannot be certain that the lines are perpendicular to the inflow jet. This is not a problem for the velocity indexes since they are based on the maximum of an absolute velocity, but the spatial variation of the velocity along the lines might be different than seen in MR data obtained by the method described in Houlind et al. (2001).

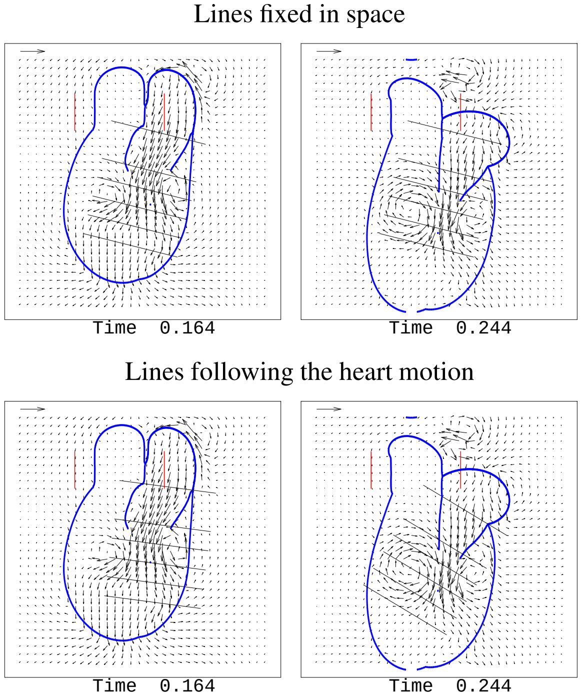

Figure 6.8: The six lines where spatial velocity profiles are computed during diastole in the case of lines fixed in space (top) and lines following the heart motion (bottom). The pictures in the left side is at the time of peak velocity at the mitral leaflet tips.

6.3.2 Gradual activation

The parameters determining the gradual activation are: the starting link in atrium $IXSA$, the starting link in ventricle $IXSV$, the onset time of systole for the starting links $t_s(IXSA)$ and $t_s(IXSV)$, the velocities V_v and V_a, the duration times of systole $t_{s,dur}$ in the atrium and in the ventricle, and the onset/end times of systole for the papillary muscle link. The parameters for the papillary muscle link are set separately from the ventricular parameters, because it turns out that the model is very sensitive to the activation of the papillary muscle.

We performed a series of simulations to decide the best setting of the parameters for the gradual activation. We define the best setting as one that best improves the comparison with MR data (see Chapter 5) without introducing non-physiological behaviour of the heart. E.g. it is important that the movement of the mitral valve is symmetrical and not asymmetrical (see Adeler and Jacobsen (2001) and Jacobsen et al. (2001)). For all of the simulations we chose to let the duration of systole be the same as in our reference model, i.e. $t_{s,dur}$ is 0.104 s and 0.306 s for the atrium and ventricle, respectively. Furthermore, t_s for the starting links were chosen to be the same as t_s in our reference model, i.e. in the first heart cycle $t_s(IXSA) = 0.362$ s and $t_s(IXSV) = 0.545$ s.

The simulations indicate that the model is not very sensitive to the activation of the atrium, showing only minor differences when we change the velocity V_a and the starting link $IXSA$. We chose to let the atrial activation propagate symmetrically over the heart wall from the midpoint on the atrial wall and with a velocity of $V_a = 0.5$ m/s, which is physiologically correct (see Section 2.3). $IXSA$ is not placed at the position of the SA node, because a symmetrical activation of the atrium gives a movement of the mitral valve that is slightly more symmetrical.

The physiologically correct velocity in the ventricle is approximately 5.0 m/s, so $V_v = 5.0$ m/s. The starting link in the ventricle is the top link on the anterior wall, since this is approximately where the AV node is located in the heart, see Section 2.3. Because the model starts up from an unphysiological situation (all the blood is at rest at $t = 0$), we chose to let the relaxation be simultaneous in the entire ventricle in the first heart cycle. The propagation of the activation over the ventricular wall does not change the simulation results very much, the biggest difference being seen in the outflow through the aortic sink. However, the model is very sensitive to the activation time of the papillary muscle link.

When the papillary muscle link is defined as part of the ventricular link chain and thus is activated according to the propagation of the activation wave, the anterior ventricular wall motion is very abnormal because of a vigorous contraction of this part of the wall. This is because the papillary muscle contracts before the posterior wall. Even if we let the papillary muscle contract 20 ms later, the contraction of the anterior wall is distorted and the mitral valve closes very asymmetrically. This can be seen in Figure 6.9 where the heart boundary configuration is shown at two times from a simulation with the gradual activation and from the reference simulation described in Chapter 4.

The distorted contraction of the anterior wall and the asymmetrical closing of the mitral valve is seen because the papillary muscle is tethered to a point along the anterior wall. In our previously reported work (Jacobsen et al., 2001; Adeler and Jacobsen, 2001) the papillary muscle was tethered to a point along the posterior wall, and here the contraction of the posterior wall was distorted and the mitral

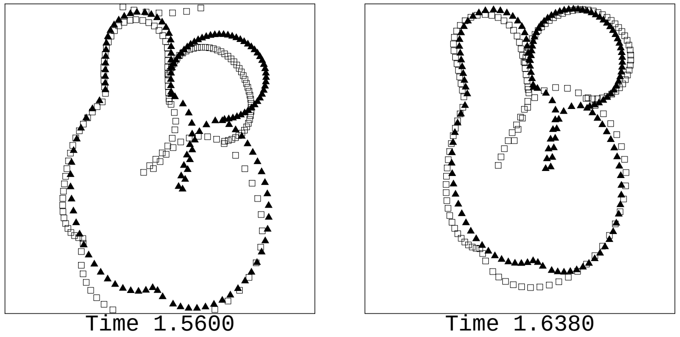

Figure 6.9: Heart boundary at two times during a heart cycle from a simulation with gradual activation with $V_v = 5.0$ m/s and 20 ms later activation of papillary muscle (□) and from the reference simulation (▲).

valve closed asymmetrically to the other side.

The best way to minimize the distortion of the anterior wall is to increase the velocity V_v in the ventricle. If we set $V_v = 10.0$ m/s and let the papillary muscle contract 10 ms later than it should according to the propagation of the activation wave, we obtain reasonable simulation results. However, $V_v = 10.0$ m/s is too high compared to typical velocities in the Purkinje fibers of approximately 3.0-5.0 m/s (see Section 2.3).

Figure 6.10 shows the heart boundary at six times during the second heart cycle from a simulation with $V_v = 10.0$ m/s and 10 ms later activation of the papillary muscle and from the reference simulation. We see some difference in the heart boundary configuration and naturally the biggest difference is during systole. But the figure also shows a better contraction of the anterior wall compared to the results in Figure 6.9 and an improved movement of the mitral valve during closing, though the valve does not close as symmetrically as in the reference simulation.

To further judge the changes in simulation results due to the gradual activation we compare pressure time profiles, velocity time profiles and flow time profiles. The pressure time profiles (not shown) show hardly any difference compared to the reference simulation. The velocity time profiles over the mitral ring and between the leaflet tips are shown in Figure 6.11. The figure shows that the peak velocities for the mitral ring profile are lower in the simulation with the gradual

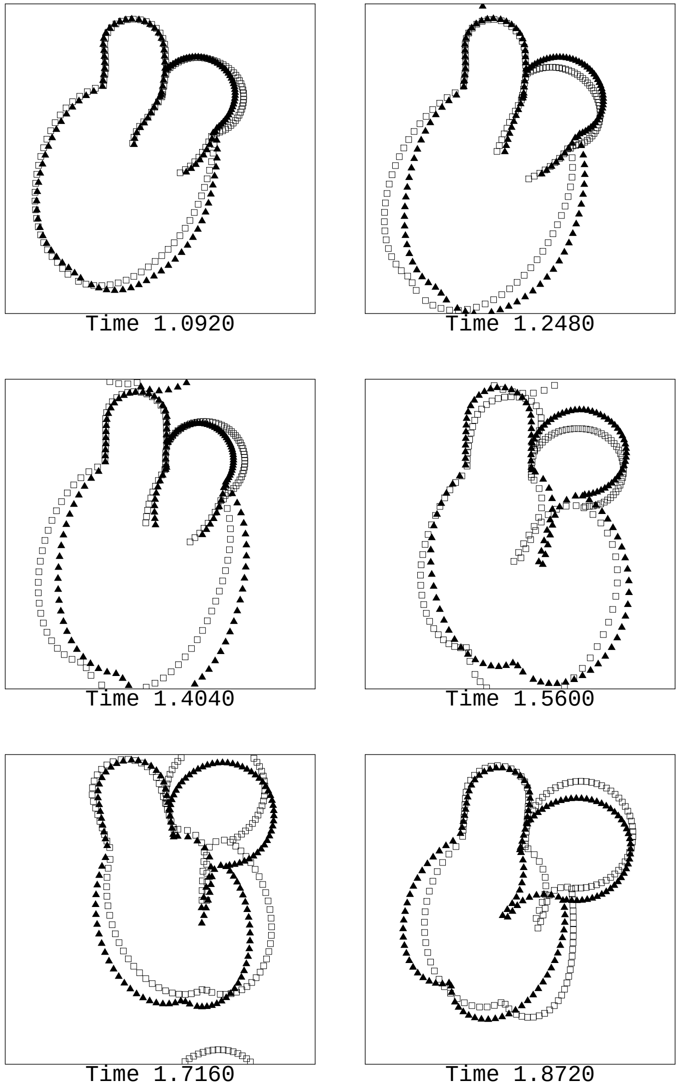

Figure 6.10: Heart boundary at six times during a heart cycle. From a simulation with gradual activation with $V_v = 10.0$ m/s and 10 ms later activation of papillary muscle (□) and from the reference simulation (▲).

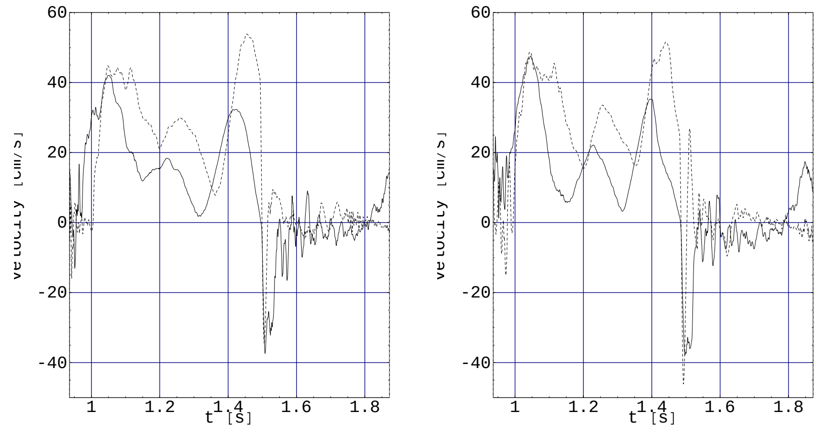

Figure 6.11: Velocity time profile of the mean velocity (cm/s) at the mitral ring (solid) and between the leaflet tips (dashed) from a simulation with gradual activation (left) and from the reference simulation (right).

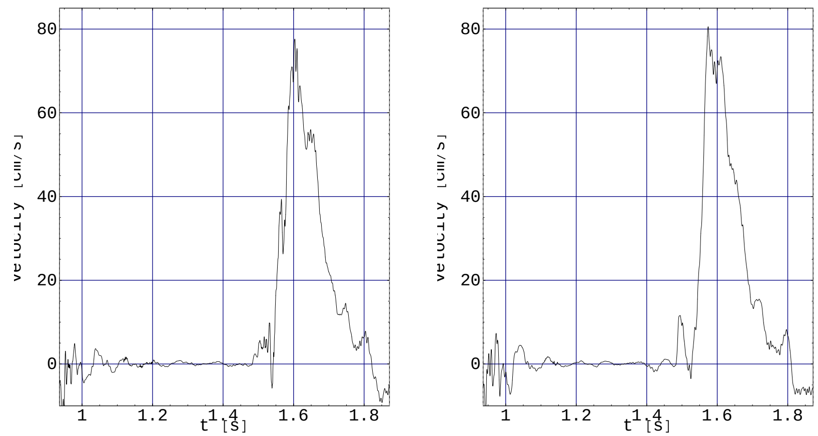

Figure 6.12: Velocity time profile of the mean velocity (cm/s) across the aortic outflow tract below the aortic sink from a simulation with gradual activation (left) and from the reference simulation (right).

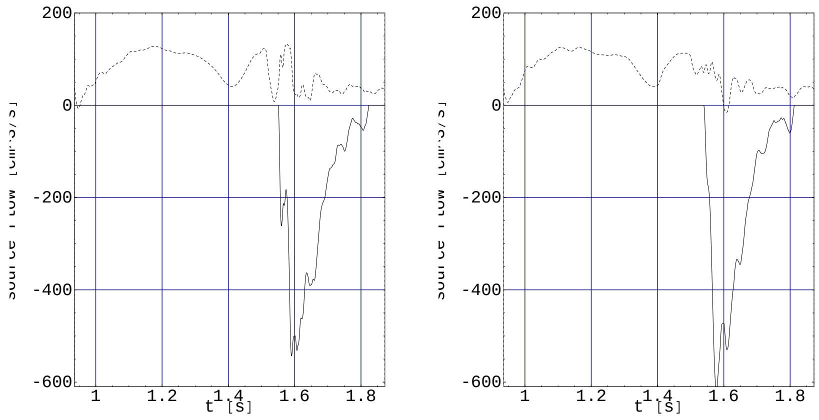

Figure 6.13: Flow time profile for the flow (cm^3/s) through the mitral source (dashed) and the aortic sink (full) from a simulation with gradual activation (left) and from the reference (right).

activation implemented. The peak in the leaflet tip profile caused by the atrial contraction is higher in the simulation with the gradual activation and, as expected, occurs later. Based on the comparison between the reference simulation and MR data presented in Chapter 5, we do not want the atrial systole to be delayed. Apart from the differences at the peaks, the profiles are comparable and have similar shapes.

Figure 6.12 shows the velocity profile across the aortic outflow tract, while Figure 6.13 shows the flow through the mitral source and aortic sink. The velocity profile across the aortic outflow tract shows only minor differences compared to the reference simulation, e.g. a slightly lower peak value. From the source/sink flow profiles we see that the aortic sink opens and closes slightly later in the simulation with the gradual activation. This is expected because onset of systole at the first link in the ventricle is at the same time as onset of systole in the entire ventricle in the reference simulation. Thus the overall ventricular contraction is delayed in the simulation with gradual activation. Furthermore, the peak outflow rate is less in the gradual activation simulation than in the reference simulation. The flow through the mitral source shows only small discrepancies, e.g. the flow is never negative in the gradual activation simulation as in the reference simulation.

The results presented in this section show that we obtain reasonable results only with an unphysiological parameter setting (V_v =10.0 m/s) and the results are very sensitive to the activation of the papillary muscle. Furthermore, the gradual activation only slightly influences the simulation results, thus we choose not to use gradual activation.

6.3.3 Regional activation

This section describes the model set up for a healthy human when we use only the regional activation. This set up involves the parameters K_e, K_r, α^0 and α_{max}, while t_s and $t_{s,end}$ are unchanged from the original model set up (see Table 3.1 for the original model set up).

In Section 6.1 we saw that pathological heart conditions affect the relaxation of the ventricular heart muscle. Thus the primary parameter to adjust is the relaxation rate constant K_r for the ventricle, which corresponds to the reciprocal of the parameter τ in physiological measurements. Adjusting K_r changes the duration time of diastole and consequently the period of the activation function, which in turn means that the length of a heart cycle is altered. We choose not to adjust any of the other parameters for the activation function, since we will limit our investigations to the early filling phase which is during relaxation.

For a healthy human τ is the same for the entire ventricle, so there are no regional differences in the relaxation. Thus K_r should be the same for the entire ventricle in the model. When comparing the value of K_r ($1/55\ \mathrm{ms}^{-1}$) in our reference model with the reciprocal of measured values of τ for the ventricle as a whole (i.e. not for any particular region in the ventricle) it turns out that this value corresponds to a diseased heart. The values of the activation function parameters in our reference model (see Table 3.1) were not chosen based on physiological knowledge, but were set to achieve the same timing in the model as in the MR data we compared the model with. Nishihara et al. (2000) find that in patients with HCM τ is 54±12ms (mean±SD), while in the control group of healthy persons τ is 32±7 ms. Similarly, Ohte et al. (1999) find that in patients with e.g. AMI τ is 48.5±6 ms, while τ for a healthy control group is 37.6±2.6 ms. Note that all of the studies mentioned are of persons with an age around 60 years. Based on these measurements of τ we change K_r from $1/55\,\mathrm{ms}^{-1}$ to $1/38\,\mathrm{ms}^{-1}$. The period of the activation function (and consequently the length of a heart cycle) then changes from 0.936 s to 0.909 s. In reducing the duration of diastole the length of a heart cycle has been reduced, and this is physiologically correct.

To determine the affect of the changed relaxation rate K_r and the shorter heart cycle length, we compare a simulation with these new parameters implemented with the reference simulation described in Chapter 4. Generally the results are

very similar. We find that the pressure level (not shown) is raised a little with the new parameter choice and the velocity time profile at the aortic outflow (not shown) is slightly changed. The velocity time profiles at the mitral valve are also changed, which is seen in Figure 6.14. The width of the first peak in the mitral ring profile is wider and the mean velocity over the mitral ring is practically zero at two points in time. From the comparison between the reference simulation and MR data in Chapter 5 we see that both of these features are improvements of the simulation results. In the velocity profile between the leaflet tips from the simulation with $K_r = 1/38\,\mathrm{ms}^{-1}$ we see a negative velocity just before $t = 1.2$ s, which is related to the semiclosure of the mitral valve.

The model with the above described parameter adjustments (K_r and length of heart cycle) we refer to as a 'healthy person'. In the following we use this model set up to study different mechanisms involved in the early filling of the left ventricle. These mechanisms are examined on the basis of velocity profiles along six transverse lines in the ventricle as described in Section 6.3.1 and on the basis of the pressure difference between atrium and ventricle, since the pressure gradient is assumed to be what drives the blood into the ventricle (see Section 6.1.1).

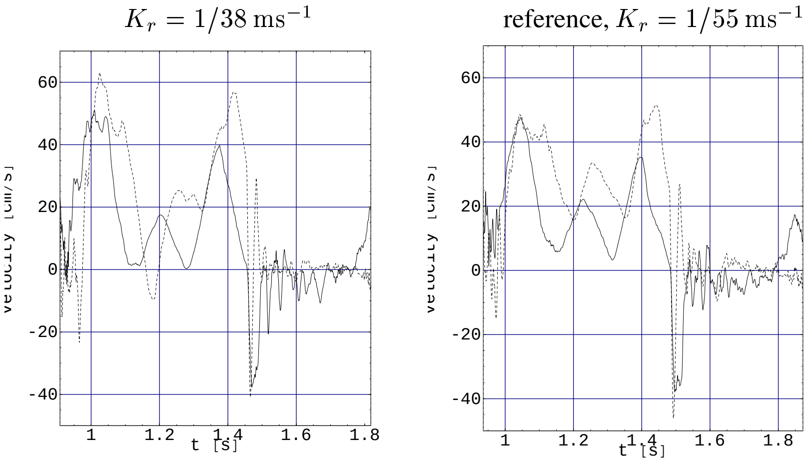

Figure 6.14: Velocity time profile of the mean velocity (cm/s) at the mitral ring (solid) and between the leaflet tips (dashed) from a simulation where $K_r = 1/38\ \mathrm{ms}^{-1}$ (left) and from the reference simulation where $K_r = 1/55\ \mathrm{ms}^{-1}$ (right).

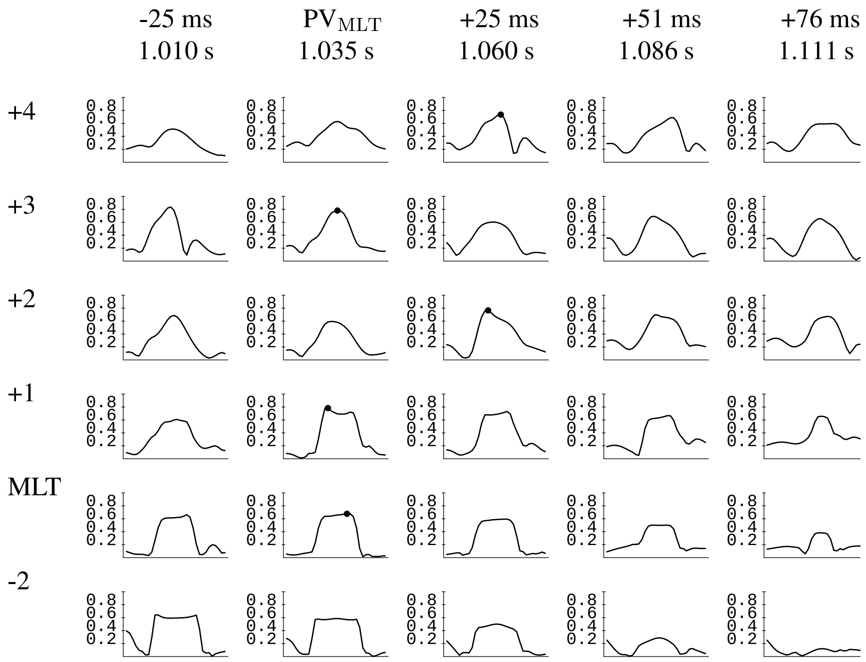

Figure 6.15: Velocity profiles of absolute velocity (m/s) along six lines at five times from a simulation of a healthy human. If the velocity profile is plotted at the time of PV at a line, PV is marked by a •.

Figure 6.15 shows the spatial velocity profiles (of absolute velocity) along the six transverse lines in the ventricle at five times: 25 ms before PV at the mitral leaflet tips, at the time of PV at the mitral leaflet tips, and 25, 51 and 76 ms after the time of PV at the mitral leaflet tips.

The velocity profiles in Figure 6.15 are similar to those of a healthy person from MR measurements shown in Figure 6.1. Figure 6.1 shows that the velocity profiles become wider and decrease in height at a line as time increases. In the simulation we do not see a wider profile at a line as time increases, but there is a decrease in height. The MR data is averaged over many heart cycles and this could result in wider and lower profiles than what typically occurs in one specific heart cycle.

The peak velocity is obtained at the same time at four of the lines in the MR

data, in the simulation this is true for three of the lines. The profiles from the MR data show that the jet gets slightly wider further down in the ventricle at a fixed time. The simulation shows the opposite: a slightly narrower jet further down in the ventricle at a fixed time. Furthermore, in the simulation the velocity profiles at the 2, 3 and 4 cm lines are triangular in shape, this is not true for the MR data, again this could be a consequence of the averaging in the MR data.

Figure 6.16 shows the peak velocity PV at the six lines from the simulation along with the same data from MR measurements of healthy persons. The MR data are the same as in Figure 6.2, so the MR data are shown as mean value with the standard deviation shown as error bars. The figure shows that PV is generally higher in the simulation, except at the MLT line. At the lines just up- and downstream of the MLT line PV is within the standard deviation of the MR data, but further downstream PV is much higher in the simulation. Furthermore, PV increases downstream of the MLT line in the simulation, while it decreases in the MR measurements. The latter is probably related to the jet becoming narrower further down in the ventricle seen in the velocity profiles from the simulation above, see Figure 6.15. In the MR data the jet becomes wider further down in the ventricle, which leads to lower PV. The narrower jet in the simulation could be a result of the vortex motion, which is much more pronounced in the simulation than seen in MR measurements, see Section 5.2. More pronounced vortices would leave less room for the jet, hereby making it narrower. This again might be a result of the model being only 2D, while the MR measurements are of the full 3D phenomenon.

Figure 6.17 shows the velocity index VI at the six lines from the simulation and the MR data of healthy persons. The latter are identical to those shown in Figure 6.3. The velocity index VI is considerably higher in the simulation, being only identical, naturally, at the MLT line with the MR data. Furthermore, VI is greater than 1 for lines downstream of MLT, which is a result of PV being higher at lines downstream in the ventricle than at the MLT line.

Figure 6.18 shows the time delay TD at the six lines from the simulation and from the MR data of healthy persons, which are the same as those shown in Figure 6.4. The figure shows that TD in the simulation is comparable to TD from the MR data; only at the line 2 cm upstream of the MLT line is TD not within the standard deviation. The value of TD at the 3 cm line from the simulation is low (0 ms) and results in a less smoothly increasing TD curve as for the MR data. The low value of TD at the 3 cm line is a results of the vortex present in the ventricle from the previous heart cycle (described in Section 5.2). This vortex extends the inflow jet (spatially) and consequently the velocity becomes high at an earlier time lower in the ventricle. This is seen in the left plot in Figure 6.19 that shows the

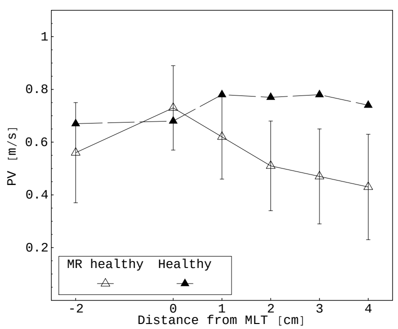

Figure 6.16: Peak velocity (PV) at the six lines from MR measurements of healthy persons (△) and from a simulation of a healthy person (▲).

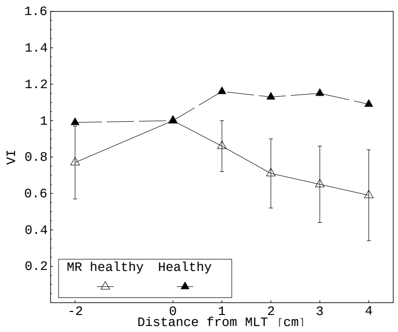

Figure 6.17: Velocity index (VI) at the six lines from MR measurements of healthy persons (△) and from a simulation of a healthy person (▲).

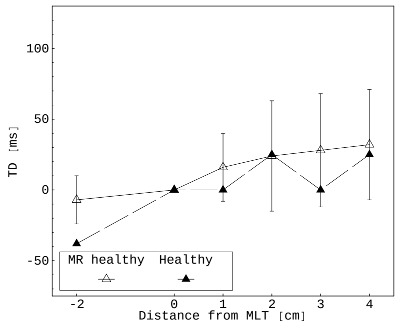

Figure 6.18: Time delay (TD) at the six lines from MR measurements of healthy persons (△) and from a simulation of a healthy person (▲).

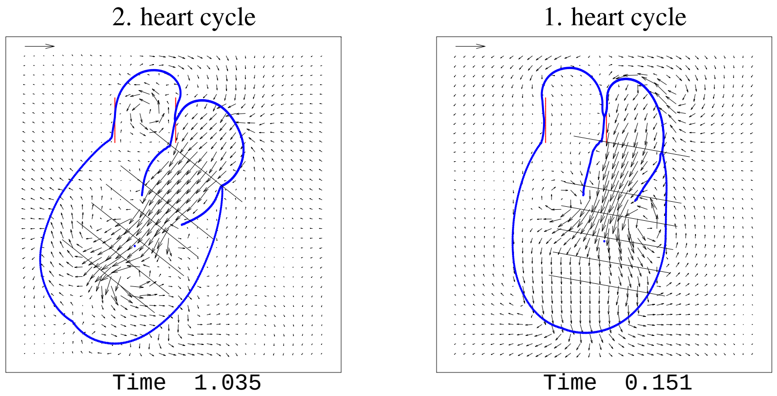

Figure 6.19: Velocity field at the time of PV at the MLT line in the second heart cycle (left) and in the first heart cycle (right).

velocity field at the time of PV at the MLT line. If the vortex was not present PV would be lower and TD would be higher at the 3 and 4 cm lines. We can support this by looking at the velocity field from the first heart cycle of the simulation, where no vortex is present low in the ventricle; see the right plot in Figure 6.19. From this figure it is clear that the jet does not reach as far into the ventricle as in the second cycle.

Figure 6.20 shows the time variation of the pressure difference between atrium and ventricle. The ventricular pressure is measured approximately 2/3 down in the ventricle from the mitral ring, while the atrial pressure is measured in the middle of the atrium. In the simulation we find a peak pressure difference during early filling of approximately 2 mmHg (the first peak in Figure 6.20 is related to early filling). The largest peak in Figure 6.20 is caused by atrial systole. Steine et al. (1999) measured using colour M-mode Doppler echocardiography the pressure difference between the mitral tip and the apex and between the atrium and the mitral tip during early diastole in dogs. They found that the peak pressure difference between mitral tip and apex was 1.9 ± 0.9 mmHg and between atrium and mitral tips it was 2.4 ± 0.7 mmHg. This gives a mean value of the pressure difference from atrium to apex of 4.3 mmHg. Thus the peak pressure difference in the simulation is reasonable compared to measurements when we take into account the deviations in the measurements and the fact that the pressure level is too low in the model, see Section 4.5.

The agreement of the velocity profiles and velocity indexes between simulation and MR data is reasonably fair. Because of previous comparisons between

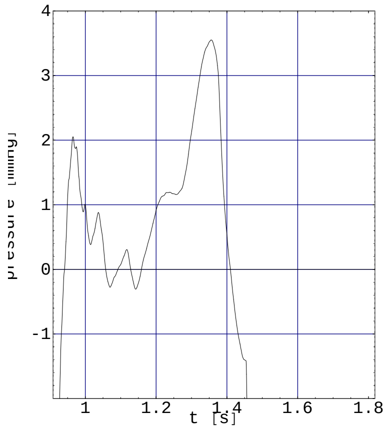

Figure 6.20: Time variation of pressure difference (mmHg) between atrium and ventricle from a simulation of a healthy human.

model and MR data (Chapter 3), we could not expect it to be better. In the following investigations we focus on the relative changes in PV, VI, TD and pressure difference when we simulate different mechanisms.

6.4 Simulations of pathological heart conditions

We wish to investigate certain mechanisms of early diastolic filling using the model described in the previous section. We hypothesize that a heart disease which affects the diastolic function can be modelled either by a change in the relaxation rate K_r or simply by letting a region of the heart wall be inactive. The former corresponds to a change in τ seen in measurements of several patient types, while the latter corresponds to a myocardial infarction, where part of the heart wall dies due to a blockage of the coronary arteries and subsequently loses its ability to contract and relax.

We include three scenarios in our investigation

1. slow relaxation of the entire ventricle
2. slow relaxation of the apical region of the ventricle
3. inactive (passive) apical region

The first scenario could have been investigated without the new activation function implemented in the model, because it corresponds to a change in K_r for the entire ventricle. This scenario corresponds to a global dysfunction of the ventricle, e.g. caused by a global ischemia. The second scenario corresponds to a local dysfunction of the heart caused by an ischemic apical region due to e.g. CAD or AMI. The third scenario resembles what happens during a myocardial infarction and thus should compare the best with results from AMI patients. We expect to see significant changes in simulation results in the this case, because an inactive region is a very drastic change of the model.

6.4.1 Slow relaxation of the ventricle

A slower relaxation in the entire ventricle corresponds to modelling a diseased heart where the global functioning of the heart is reduced. We achieve a slower relaxation by decreasing the value of K_r for the entire ventricle corresponding to an increase in τ. Nishihara et al. (2000) report τ values of 54±12 ms for patients with HCM, while St. Goar et al. (1991) report τ values of 59±8 ms for patients with DCM, and finally Ohte et al. (1999) report values of 47±6.3 ms for CAD patients. Based on these three studies we adjust K_r to $1/60\ \mathrm{ms}^{-1}$ corresponding to $\tau = 60$ ms. With $K_r = 1/60\ \mathrm{ms}^{-1}$ the period of the activation function, and consequently the length of the heart cycle, becomes 0.942 s. Apart from these adjustments, the parameter setting is identical to the reference simulation.

The velocity profiles along the six transverse lines in the ventricle are shown in Figure 6.21 at five times: 26 ms before PV at the mitral leaflet tips, at the time of PV at the mitral leaflet tips, and 26, 52 and 78 ms after the time of PV at the mitral leaflet tips. From the figure we see that the shape of the velocity profiles have not changed compared to a simulation of a healthy human (Figure 6.15).

Figures 6.22–6.24 show the peak velocity PV, the velocity index VI, and the time delay TD, respectively. In each of these three figures the corresponding data from MR measurements of healthy persons and from a simulation of a healthy person are included. The data from the MR measurements is identical to that of Figures 6.2–6.4, while the data from a simulation of a healthy person is identical to that of Figures 6.16–6.18.

From both the velocity profiles and the plot of PV we see that the peak velocities in the present simulation are lower than in the simulation of a healthy person. The peak velocities still have a tendency to increase further downstream of the MLT line, where the MR data shows a decrease. The relatively high PV value at the 3 cm line is not related to the inflow jet but is due to the vortex in the lower part of the ventricle. This can be seen by looking at the velocity field at the time

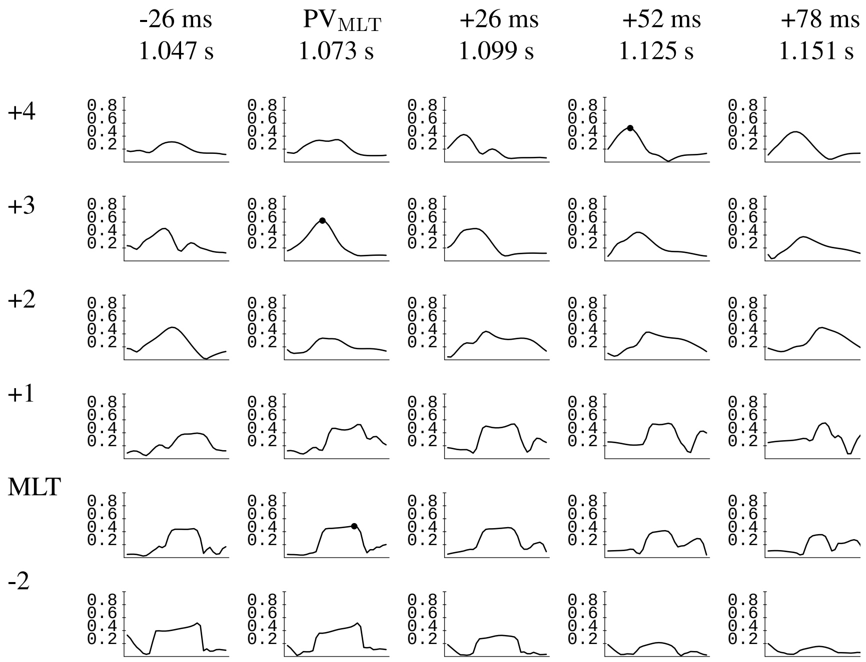

Figure 6.21: Velocity profiles of absolute velocity (m/s) along six lines at five times from a simulation where ventricular relaxation is slow. If the velocity profile is plotted at the time of PV at a line, PV is marked by a •.

of PV at the MLT line shown in Figure 6.25. Because of this vortex we should not put too much emphasis on the velocity indexes from the 3 and 4 cm lines, since they are not related to the inflow jet but rather to the vortex.

We only see a small change in VI in the present simulation compared to a simulation of a healthy person. However, Figure 6.23 shows that the velocity index VI is generally higher in the simulation than seen in MR measurements of healthy persons. We have no measured data of VI in patients with a globally reduced functioning of the ventricle to compare with.

Figure 6.24 of TD shows that at lines 1 and 2 cm downstream of the MLT line TD is substantially higher compared to a simulation of a healthy person. At the 3 and 4 cm lines TD is not higher or only moderately higher. TD at the 3 and 4 cm lines is not obtained for the inflow jet, as described above, but rather

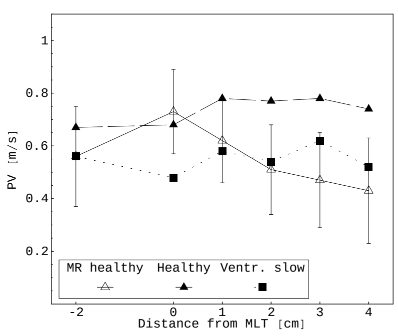

Figure 6.22: Peak velocity (PV) at the six lines from MR measurements of healthy persons (△), and from a simulation of a healthy person (▲) and a simulation where the ventricular relaxation is slow (■).

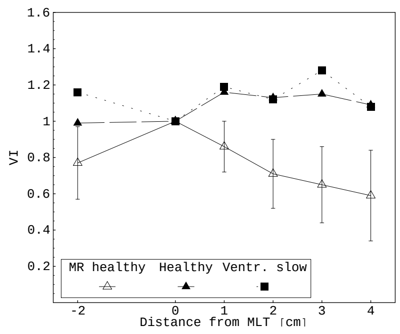

Figure 6.23: Velocity index (VI) at the six lines from MR measurements of healthy persons (△), and from a simulation of a healthy person (▲) and a simulation where the ventricular relaxation is slow (■).

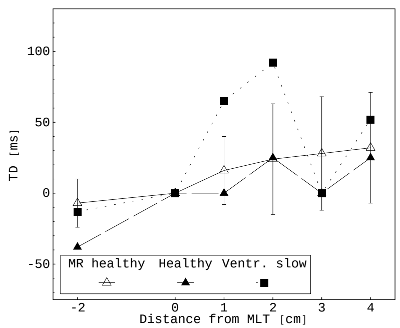

Figure 6.24: Time delay (TD) at the six lines from MR measurements of healthy persons (△), and from a simulation of a healthy person (▲) and a simulation where the ventricular relaxation is slow (■).

from the vortex in the ventricle. If the vortex was not present we would expect that TD would be much higher at lower lines. Stugaard et al. (1994b) measures the apical time delay in dogs, both in healthy dogs and when beta-blockade is induced. According to Kim (2001) induction of beta-blockade affects the ventricle globally, so we can use this for comparison with our present simulation. Stugaard et al. (1994b) find that the mean value of the apical time delay for healthy dogs is 21 ms, and it increases to 80 ms when beta-blockade is induced. Thus the substantially increased TD in our simulation compares well with measurements.

If we compare the velocity field at the time of peak velocity at the mitral leaflet tips (Figure 6.25) with the velocity field from a healthy human (Figure 6.19) we can see that the inflow jet is not as strong. It has lower velocities and does not reach as deeply into the ventricle as for a healthy human. Both of these findings are identical to the findings of the velocity profiles and indexes above and are signs of poor diastolic filling.

Figure 6.26 shows the time variation of the pressure difference between the atrium and ventricle during diastole from the simulation. By comparing the figure with the same from a simulation of a healthy person (Figure 6.20) we see that the peak pressure difference during early filling is reduced. In a healthy human it is approximately 2 mmHg, while it is approximately 1.2 mmHg in the present simulation, i.e. a 40% reduction. Stugaard et al. (1994b) find a peak pressure difference between atrium and ventricle of 3.9 mmHg (mean value) in healthy dogs, while it falls to 3.4 mmHg during induction of beta-blockade, this is a 13%

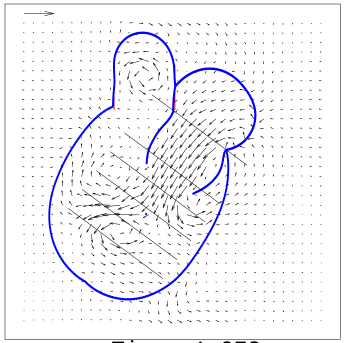

Figure 6.25: Velocity field at the time of peak velocity at the MLT line from a simulation where the ventricular relaxation is slow.

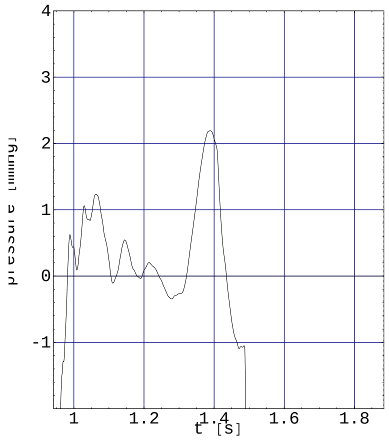

Figure 6.26: Time variation of pressure difference (mmHg) between atrium and ventricle from a simulation where the ventricular relaxation is slow.

reduction.

Lemmon and Yoganathan (2000a) have made an investigation of ventricular dysfunction using a 3D model of the left atrium and ventricle based on the immersed boundary method (Lemmon and Yoganathan, 2000b). Their model have been found to be in agreement with clinically observed diastolic flow conditions (Lemmon and Yoganathan, 2000b), but the intraventricular flow pattern has not been compared in detail with e.g. MR data.

Lemmon and Yoganathan (2000a) examine the blood velocity in the ventricular inflow tract, that is, from the mitral annulus and 3.5 cm into the ventricle. One of their simulation cases is similar to our present simulation: delayed ventricular relaxation. They compare their simulation with a simulation where the relaxation is normal. They find that the peak velocity is decreased in the diseased case: the peak velocity at the mitral ring in the normal case is approximately 0.74 cm/s and it decreases to approximately 0.68 cm/s in the diseased case. Both of these values are higher than our similar results and higher than the value from the MR data, but within the standard deviation of this. Lemmon and Yoganathan (2000a) find that the peak velocity progresses slower into the ventricle.

Summarizing our results, we find that a slower relaxation of the entire ventricle results in generally lower peak velocities in the ventricle and a delayed filling. It can be explained by a reduced pressure difference between the atrium and the ventricle. The lower peak velocities and delayed filling is similar to the simulation results of Lemmon and Yoganathan (2000a), who use a 3D model of the left side of the heart. The increased time delay and reduced pressure difference is in accordance with the findings of Stugaard et al. (1994b), who measured the changes in dogs during induction of beta-blockade, which affects the ventricle globally.

6.4.2 Slow relaxation of apical region

The second scenario is a simulation where the relaxation of the apical region (region 3 in Figure 6.7) is slowed. This corresponds to modelling a heart where the apical region is ischemic. Steine et al. (1999) measures τ in the apical region in healthy dogs and in dogs with acute ischemic failure. Acute ischemic failure is obtained by induced coronary microembolization. Steine et al. (1999) measures a τ_{apex} in the apical region in the ischemic heart of 49±6 ms (mean±SD). Thus we choose to let the relaxation rate constant K_r be $1/55\ \mathrm{ms}^{-1}$ in the apical region, while it is still $1/38\ \mathrm{ms}^{-1}$ in the rest of the ventricle as for a healthy human. The length of a heart cycle is still 0.909 s.

Figure 6.27 shows the velocity profiles along the six transverse lines at five times: 25 ms before PV at the mitral leaflet tips, at the time of PV at the mitral leaflet tips, and 25, 50 and 76 ms after the time of PV at the mitral leaflet tips. The velocity profiles are not very different from the ones in the simulation of a healthy person in Figure 6.15.

Figures 6.28–6.30 show the peak velocity PV, the velocity index VI, and the time delay TD, respectively. In each of these three figures the corresponding data from MR measurements of healthy persons and AMI patients and from a simulation of a healthy person are included. The data from the MR measurements is identical to that of Figures 6.2–6.4, while the data from a simulation of a healthy person is identical to that of Figures 6.16–6.18.

Figure 6.28 shows that PV is not very different in the present simulation compared to a simulation of a healthy person. Only at the 3 cm line do we see a considerably higher PV. This is, as seen in the previous simulation, related to the vortex present in the ventricle, as can be seen by looking at the velocity field at the time of PV at the MLT line in Figure 6.31. The change in PV between a simulation of a healthy person and the present simulation is not the same as seen in MR measurements between healthy persons and AMI patients. In the MR measurements PV decreases at the 3 and 4 cm lines, and in the simulation we actually see an increase (again because of the vortex).

The same pattern is seen for VI in Figure 6.29. VI is the same from the present simulation and the simulation of a healthy person, except at the 3 and 4 cm lines.

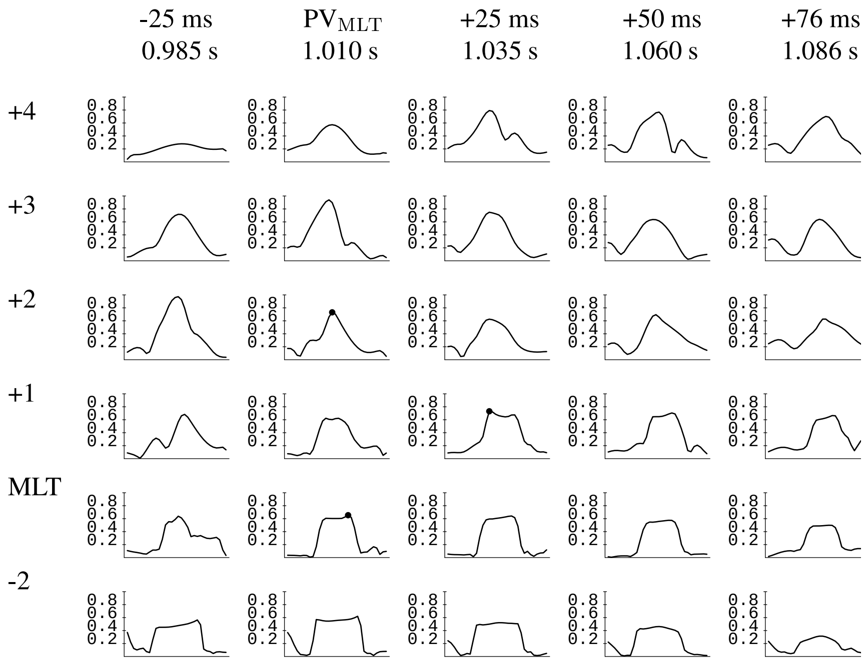

Figure 6.27: Velocity profiles of absolute velocity (m/s) along six lines at five times from a simulation where the apical relaxation is slow. If the velocity profile is plotted at the time of PV at a line, PV is marked by a •.

Here, VI is higher in the present simulation. MR measurements of healthy persons and AMI patients show that VI should decrease in an AMI patients at the 3 and 4 lines and otherwise be unchanged.

Figure 6.30 shows that TD is higher in the present simulation than seen in the simulation of a healthy person, except at the 2 cm line where it is lower. The MR data also shows that TD increases in an AMI patient compared to a healthy person, but only at the 3 and 4 cm lines. Because of the vortex in the simulations we should not put too much emphasis on the results from the 3 and 4 cm lines, so we must conclude that TD does not show significant changes in the present simulation compared to the simulation of a healthy person.

The plot of the velocity field at the time of peak velocity at the mitral leaflet tips (Figure 6.31) is very similar to the velocity field seen for a healthy human

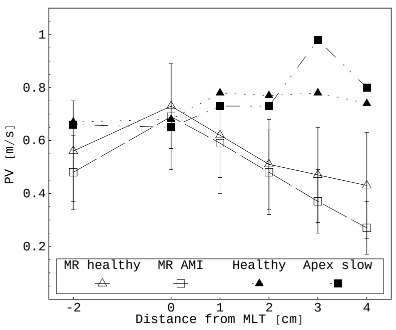

Figure 6.28: Peak velocity (PV) at the six lines from MR measurements of healthy persons (△) and AMI patients (□), and from a simulation of a healthy person (▲) and a simulation where the apical relaxation is slow (■).

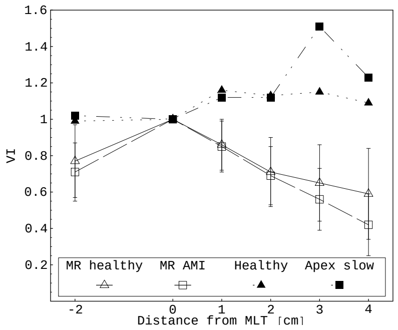

Figure 6.29: Velocity index (VI) at the six lines from MR measurements of healthy persons (△) and AMI patients (□), and from a simulation of a healthy person (▲) and a simulation where the apical relaxation is slow (■).

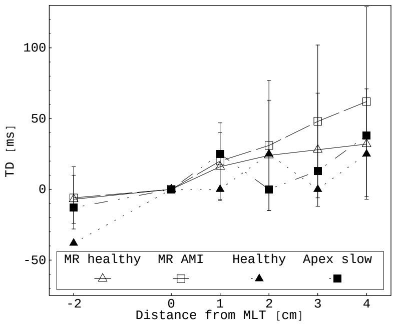

Figure 6.30: Time delay (TD) at the six lines from MR measurements of healthy persons (△) and AMI patients (□), and from a simulation of a healthy person (▲) and a simulation where the apical relaxation is slow (■).

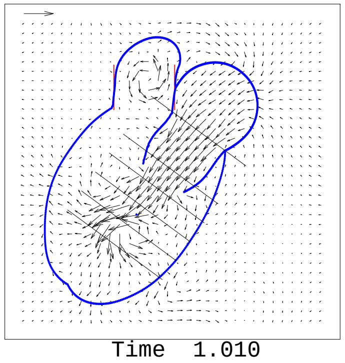

Figure 6.31: Velocity field at the time of peak velocity at the MLT line from a simulation where the apical relaxation is slow.

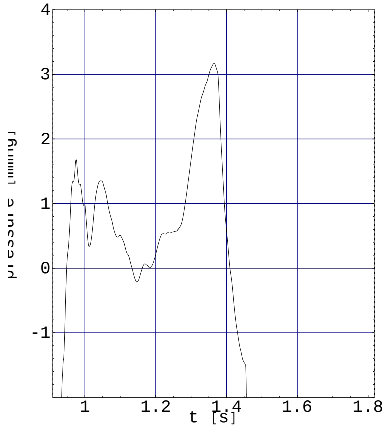

Figure 6.32: Time variation of pressure difference (mmHg) between atrium and ventricle from a simulation where the apical relaxation is slow.

(Figure 6.19), which agrees with the results above: the present simulation is not very different from the simulation of a healthy human presented in Section 6.3.3. This is further supported by the plot of the pressure difference between atrium and ventricle shown in Figure 6.32. The peak pressure difference is somewhat lower than in the simulation of a healthy human (Figure 6.20), it has decreased approximately 15%. But this is not in agreement with what Stugaard et al. (1994b) found for dogs with acute ischemic failure, where the peak pressure difference decreased approximately 59%.

In summary, we find that the simulation of a slow relaxation of the apical region is not very different compared to a simulation of a healthy person, an observation which holds for both velocity and pressure difference data. These simulation results are not in agreement with measurements on humans and dogs, where substantial changes are seen in AMI patients compared to healthy persons.

6.4.3 Apical region inactive

The third scenario we investigate is the case of an inactive (or passive) apical region. This means that the region neither contracts nor relaxes. It is simply passive tissue following the motion of the blood. It corresponds to a myocardial infarction, where part of the heart wall dies due to a blockage of the coronary arteries and subsequently looses its ability to contract and relax. When we simulate an inactive region of the heart wall in 2D it corresponds to a whole cross section of the heart being inactive in 3D. Thus, this type of simulation is only reasonable when the inactive region is located at the apex. Choosing any other region in a 2D model would not be very meaningful.

We simulate a passive region by letting it be defined similarly to the valve tissue, i.e. by not letting it have any muscle property. We do this only for the links along the heart wall in the apex region, i.e. not for the cross links in the region. We reduce the size of the apical region because the model cannot withstand the pressure in systole when the entire apical region is inactive. As a consequence of the high pressure, the walls leak and blood leaves the ventricle through the ventricular wall. Even when we reduce the size of the inactive region we have to increase the number of boundary points to withstand the systolic pressure.

During diastole the heart boundary configuration from the simulation with an inactive apical region (left side plot in Figure 6.33) is not very different from the configuration for a healthy person (Figure 6.19), the ventricle being slightly larger. But when systole sets in it is clear that the apical part is inactive: it bulges out and hangs like a balloon filled with water below the contracted upper part of the ventricle. The right side plot in Figure 6.33 shows the velocity field and heart

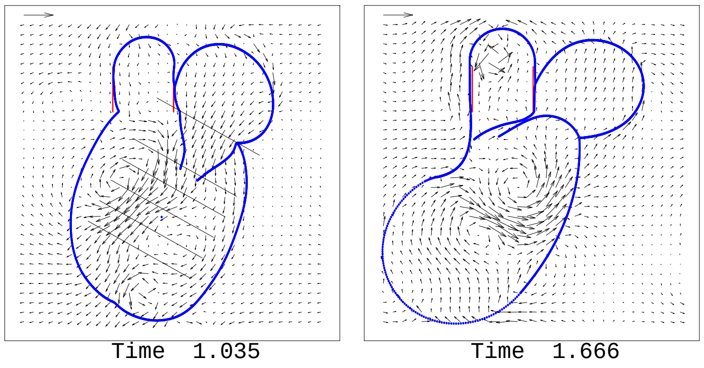

Figure 6.33: Velocity field and heart boundary at the time of peak velocity at MLT line (left) and during systole (right) from a simulation where the apical region is inactive.

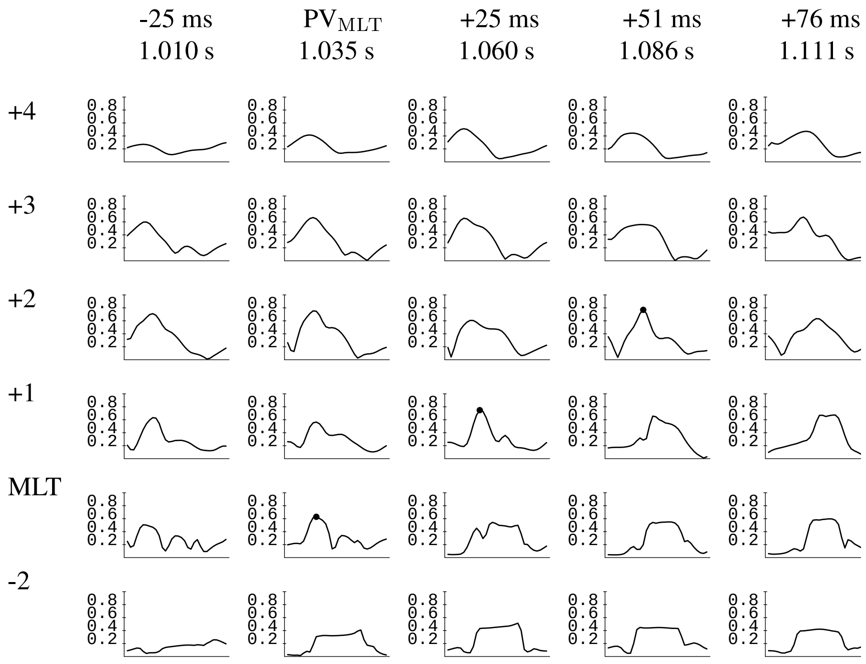

Figure 6.34: Velocity profiles of absolute velocity (m/s) along six lines at five times from a simulation where the apical region is inactive. If the velocity profile is plotted at the time of PV at a line, PV is marked by a •.

boundary at $t = 1.666$ s, where the large ventricle is clearly seen. Compare this plot with the velocity field in the last frame (at $t = 1.716$ s) in Figure 4.2. The two plots are at the same time relative to the length of a heart cycle.

Figure 6.34 shows the velocity profiles along the six transverse lines in the ventricle at five times: 25 ms before PV at the mitral leaflet tips, at the time of PV at the mitral leaflet tips, and 25, 51 and 76 ms after the time of PV at the mitral leaflet tips. Comparing the velocity profiles with those obtained for a healthy human (Figure 6.15) we see several changes. The profiles are generally lower, wider and more skewed. The latter can also be seen from the plot of the velocity field at the time of peak velocity at the mitral leaflet tips in Figure 6.33. If we compare this to the velocity field for the healthy human (Figure 6.19) we see that the direction of the inflow jet is more toward the anterior wall in the

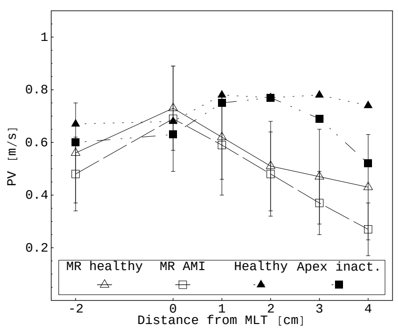

Figure 6.35: Peak velocity (PV) at the six lines from MR measurements of healthy persons (△) and AMI patients (□), and from a simulation of a healthy person (▲) and a simulation where the apical region is inactive (■).

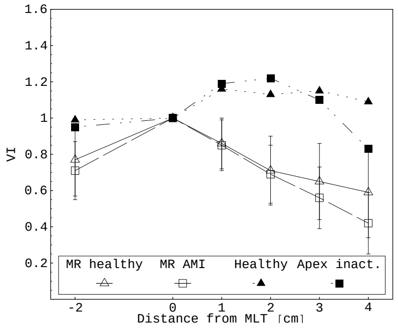

Figure 6.36: Velocity index (VI) at the six lines from MR measurements of healthy persons (△) and AMI patients (□), and from a simulation of a healthy person (▲) and a simulation where the apical region is inactive (■).

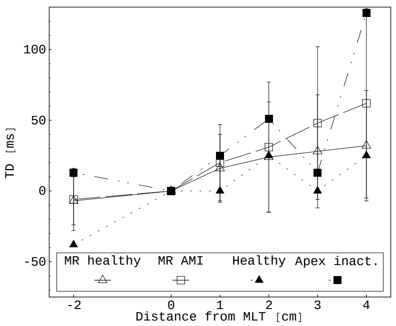

Figure 6.37: Time delay (TD) at the six lines from MR measurements of healthy persons (△) and AMI patients (□), and from a simulation of a healthy person (▲) and a simulation where the apical region is inactive (■).

present simulation. Furthermore, the shape of the profiles in Figure 6.34 are more triangular than for a healthy person.

Figures 6.35–6.37 show the peak velocity PV, the velocity index VI, and the time delay TD, respectively. In each of these three figures the corresponding data from MR measurements of healthy persons and AMI patients and from a simulation of a healthy person are included. The data from the MR measurements is identical to that of Figures 6.2–6.4, while the data from a simulation of a healthy person is identical to that of Figures 6.16–6.18.

Figure 6.35 shows that downstream of the MLT line PV is lower at the 3 and 4 cm lines compared to the simulation of a healthy person. This is in contrast to what we saw in the previous scenario (with a slow relaxation of the apical region), here PV was higher at those lines. In the present simulation PV is lower despite the vortex present in the ventricle, so we believe that we can trust these results more. The change in the variation of PV with the distance from the MLT line is very similar in simulations and MR measurements: PV is generally lower in a diseased heart, but mostly at the 3 and 4 cm lines.

We find the same good agreement between simulations and MR measurements when we look at VI in Figure 6.36. VI is lower at the 4 cm line in a diseased heart (both from simulations and MR data) than in a healthy heart, otherwise it does not change much. It should be noted, however, that in MR measurements VI is also lower at the 3 cm line in an AMI patient than in a healthy person

Figure 6.37 shows that TD is higher in the present simulation than in the simulation of a healthy person, especially for the -2 and 4 cm lines. This is in reasonable agreement with the MR measurements. Here, TD is higher at the 3 and 4 cm lines for AMI patients compared to healthy persons, otherwise it is unchanged. TD from the present simulation is everywhere within the standard deviation of the MR results. A much higher TD at the line closest to the apex is in good agreement with the findings of Stugaard et al. (1994b). They measure the time delay in healthy dogs and dogs with acute ischemic failure and find that the time delay increases approximately by a factor of 5 (from 20 ms to 101 ms).

The simulation results can partly be explained by the pressure difference between atrium and ventricle, which is plotted in Figure 6.38. The figure shows a small positive pressure difference first, and then, delayed compared to a healthy human (Figure 6.20), a larger positive pressure peak occurs. The peak pressure difference is larger than for the healthy human. The later occurrence of the peak pressure difference explains why TD increases, but since the peak is larger than for a healthy person it does not explain why PV and VI are lower at the 4 cm line. The larger peak pressure difference in the present simulation compared to the simulation of a healthy person is not in agreement with the findings of Stugaard et al.

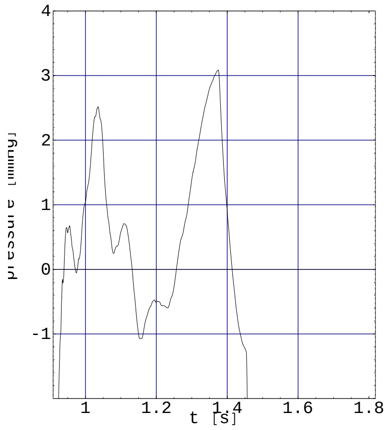

Figure 6.38: Time variation of pressure difference (mmHg) between atrium and ventricle from a simulation where the apical region is inactive.

(1994b). They find that the peak pressure decreases with approximately 58% in dogs during acute ischemic failure compared to healthy dogs.

The simulation of an inactive apical region compares reasonably well with MR measurements of AMI patients. We see the same changes in the velocity profiles and indexes found by Houlind et al. (2001) in MR measurements of healthy persons and AMI patients. The shapes of the velocity profiles are more triangular in a diseased heart, and PV and VI are lower near the apex while TD is higher near the apex. The variation of the pressure difference between the atrium and the ventricle explains the higher TD value but not the lower values of PV and VI. Furthermore, the peak pressure difference is not in agreement with measurements.

6.5 Conclusions

We have implemented a gradual activation of the heart muscle in the model and compared a simulation with the gradual activation with the reference simulation from Chapter 4. The comparison showed that the model is very sensitive to the activation time of the papillary muscle, because the latter influences the contraction pattern of the ventricular wall and the movement of the mitral valve. The results from a simulation where we adjusted the activation time of the papillary muscle

and the propagation velocity in the ventricle showed that the gradual activation does not introduce major differences in the flow pattern. The biggest difference is seen at the aortic outflow as a delayed opening/closing of the aortic sink and a lower peak outflow rate. We choose not to use the gradual activation because it introduces only small changes, and because of the sensitivity to the activation of the papillary muscle.

We also implemented a regional activation, where it is possible to define the parameters determining the activation function independently for 5 regions in the ventricular wall. This was our basis for conducting investigations of the mechanisms of the early diastolic filling phase.

We simulated a healthy human and compared the results with MR measurements. The velocity profile along six transverse lines in the ventricle and the velocity indexes derived from the profiles compare reasonably well with MR measurements. The pressure difference between atrium and ventricle, which drives the blood into the ventricle, also compared well with measurements.

We have investigated three scenarios which reflect the mechanisms of early diastolic filling: slow relaxation of the ventricle, slow relaxation of the apical region, and an inactive apical region. We hypothesized that diastolic dysfunction could be modelled by a lower relaxation rate K_r (corresponding to a higher τ in measurements) or simply by letting a region of the heart wall be inactive.

In the first scenario we saw lower peak velocities and a delayed filling, and this could be explained by a reduced pressure difference between the atrium and the ventricle. These results were in agreement with the measurements of Stugaard et al. (1994b), who investigated dogs during induction of beta-blockade, which affects the ventricle globally. Thus it is possible to simulate global ischemia in the ventricle by decreasing K_r.

The second scenario revealed that the simulation results do not change very much when one region relaxes slower than the other regions. These simulation results are not in agreement with measurements on both human and dogs, where substantial changes are seen. Thus decreasing K_r regionally does not simulate a local ischemic situation.

The results of the third scenario where the apical region is inactive compared well with MR measurements of AMI patients. Both velocity profiles and velocity indexes showed the same change between a healthy and a diseased heart (AMI) as seen in MR data. However, these changes could only partly be explained by the pressure difference between atrium and ventricle seen in the simulation. The peak pressure difference was, furthermore, not in agreement with measurements. Thus letting the apical region be inactive seems to be a reasonable way of modelling AMI.

We conclude that the model can be used to study certain mechanisms involved in the early diastolic filling phase. The model can capture mechanisms that change the relaxation pattern drastically, but smaller changes in the relaxation pattern do not change the model results. We have shown that it is possible to model a global diastolic dysfunction by changing the relaxation rate K_r. But in the case of an ischemic apical region (a local dysfunctioning region), we could not model it by changing K_r, but we were able to simulate an infarction by letting the region be inactive, even though the driving pressure difference was not in agreement with measurements.

Chapter 7

The 3D heart model

Originally it was hoped that the 2D model could be used as a preliminary testing tool for experiments eventually to be carried out in the 3D heart model. However, it turned out that the 3D model was computationally too demanding and did not match MR measurements well enough to be used for experiments and investigations of the type presented in Chapter 6 for the 2D model.

This chapter describes briefly the 3D heart model and presents a comparison of the output from a simulation with MR data. The computational demand of the 3D model is also presented.

7.1 Description of the model

The principles of the 3D model are similar to those of the 2D model. The heart is immersed in a cube filled with a fluid of the same density and viscosity as blood. The heart boundary (muscular wall and the valve leaflets) are treated as massless one-dimensional boundaries totally immersed in fluid (blood) with the potential of exerting forces on the fluid. In- and outflow to the heart is modelled by sources and sinks and the model includes an exterior sink/source to make room for the variation in total heart volume during a heartbeat.

The major difference between the 2D and 3D models is that the 3D model is of the full heart (all four heart chambers and the nearby great vessels), while the 2D model is of the left side only. Furthermore, some computational differences exist and these are described in the following.

7.1.1 Equations of motion

The governing equations of motion are

$$\rho\left(\frac{\partial \boldsymbol{u}}{\partial t} + \boldsymbol{u}\cdot\nabla\boldsymbol{u}\right) = -\nabla p + \mu\nabla^2\boldsymbol{u} + \boldsymbol{F} \tag{7.1}$$

$$\nabla\cdot\boldsymbol{u} = \psi(\boldsymbol{x},t) \tag{7.2}$$

$$\boldsymbol{F}(\boldsymbol{x},t) = \int \boldsymbol{f}(q,r,s,t)\delta(\boldsymbol{x}-\boldsymbol{X}(q,r,s,t))\,dq\,dr\,ds \tag{7.3}$$

$$\frac{\partial \boldsymbol{X}}{\partial t}(q,r,s,t) = \boldsymbol{u}(\boldsymbol{X}(q,r,s,t),t) \tag{7.4a}$$

$$= \int \boldsymbol{u}(\boldsymbol{x},t)\delta(\boldsymbol{x}-\boldsymbol{X}(q,r,s,t))\,d\boldsymbol{x} \tag{7.4b}$$

$$T = \sigma\left(\left|\frac{\partial \boldsymbol{X}}{\partial s}\right|; q,r,s,t\right) \tag{7.5}$$

$$\boldsymbol{\tau} = \frac{\partial\boldsymbol{X}/\partial s}{|\partial\boldsymbol{X}/\partial s|} \tag{7.6}$$

$$\boldsymbol{f} = \frac{\partial}{\partial s}(T\boldsymbol{\tau}) \tag{7.7}$$

The 3D Eulerian variables are the velocity $\boldsymbol{u}(\boldsymbol{x},t)$, the pressure $p(\boldsymbol{x},t)$, the force $\boldsymbol{F}(\boldsymbol{x},t)\,d\boldsymbol{x}$ and the density distribution of the sources and sinks $\psi(\boldsymbol{x},t)$, where $\boldsymbol{x}$ denotes position in space, $d\boldsymbol{x}$ is the volume element, and t is time. The Lagrangian variables are the fiber point position $\boldsymbol{X}(q,r,s,t)$, the fiber tension $T(q,r,s,t)\,dq\,dr$, the unit tangent to the fibers $\boldsymbol{\tau}(q,r,s,t)$ and the resultant fiber force $\boldsymbol{f}(q,r,s,t)\,dq\,dr\,ds$. $\boldsymbol{F}$ and $\boldsymbol{f}$ are corresponding force densities. Here q, r and s are curvilinear coordinates chosen in such a way that (q,r) labels a particular fiber and (q,r,s) labels a particular material point. The equations, as written here, describe a three-dimensional system of fibers as is appropriate for the thick heart wall. A valve leaflet is a fiber-reinforced surface and can be described by dropping one of the indices q or r.

Equation (7.1) is the three-dimensional Navier-Stokes equation and equation (7.2) is the continuity equation, the 3D versions of equations (3.1) and (3.2), respectively for the 2D case. Peskin and McQueen have not, to our knowledge, published a description of the density distribution ψ in 3D, but since sources and sinks are handled identically in the 2D and 3D models, the density distribution in the 3D model will be of the same form as in the 2D model (see equation (3.8)). The only difference is that the summation is over the total number of sources and sinks in the 3D model.

Recently McQueen and Peskin (2000) introduced the new form of the momentum equation discussed in Section 4.6, which takes into account the different form of the continuity equation and consequently the different form of the momentum equation, when distributed sources and sinks are included. However, this it is not included in the version of the 3D code we work with.

Equations (7.3) and (7.4b) are the interaction equations that connect Eulerian and Lagrangian quantities, analogous to equations (3.3) and (3.4) in the 2D case. Here $\delta(\boldsymbol{x}-\boldsymbol{X}(q,r,s,t))$ is the three-dimensional Dirac delta function.

Equations (7.6)–(7.7) are the fiber equations that are used to determine the Lagrangian fiber force density $\boldsymbol{f}$ from the fiber configuration $\boldsymbol{X}$ at time t. In equation (7.5), $|\partial\boldsymbol{X}/\partial s|$ is the fiber strain and σ is the stress-strain relation of the fibers. Note the explicit time dependence in σ, which allows the heart to contract and relax.

Boundary forces

In the 3D case the heart muscle is not represented by the 3 element model described in Section 3.3.5 for the 2D model, nor is the passive tissue modelled by linear springs. In the 3D model the tension T in a short fiber segment is given by a non-linear relation ship

$$T = \begin{cases} S_0\left(\dfrac{L-L_0}{L_0}\right)^2 & L \geq L_0 \\ 0 & L < L_0 \end{cases}$$

where L is the length of the fiber segment, L_0 is the resting length of the segment and S_0 is the stiffness. In the case of active, contractile heart muscle L_0 and S_0 are time dependent, while they are constant for passive tissue. In the original 2D model the entire atrium contracts simultaneously, and, after a delay, the entire ventricle contracts simultaneously, this is also the case in the 3D model. The propagation of the activation wave introduced in the 2D model in Chapter 6 could easily be introduced in 3D by defining the time dependence of L_0 and S_0 differently for different parts of the heart.

Sources and sinks

The 3D model includes all the nearby great vessels of the heart: the aorta, the pulmonary artery, the four pulmonary veins and the superior and inferior vena cava. All the vessels have blind ends, but are equipped with either a source (pulmonary veins and vena cava) or a sink (aorta and pulmonary artery). Furthermore, an exterior source/sink allows for volume changes as the heart fills and ejects.

As in the original 2D model the relation between flow and pressure for all sources and sinks is chosen to be a linear resistance model pumping against a constant pressure reservoir, see Section 3.2.1 for a description of the linear resistance model of the atrial source in the 2D model.

7.1.2 Computational method

The numerical method used in the 3D model is different from the one in the 2D model. It is based on the following discretization of the equations of motion. Time is divided into intervals of length Δt. The fluid equations are discretized on a regular cubic lattice in the physical space of the variable $\boldsymbol{x} = (x_1, x_2, x_3)$, and the fiber equations are discretized on a rectangular lattice in the space of the Lagrangian parameters q, r, s. The mesh widths of these lattices are $h = \Delta x_1 = \Delta x_2 = \Delta x_3$ and Δq, Δr, Δs, respectively.

On the fluid lattice the forward, backward and central divided difference operators are denoted D^+, D^- and D^0, respectively. A subscript $\alpha = 1, 2, 3$ indicates the direction in which the difference is applied. $\boldsymbol{D}^0$ is used for the vector difference operator $(\boldsymbol{D}_1^0, \boldsymbol{D}_2^0, \boldsymbol{D}_3^0)$, which corresponds to ∇.

On the Lagrangian fiber lattice the central difference operator in the fiber direction is denoted D_s and defined by

$$(D_s\phi)(s) = (\phi(s + \Delta s/2) - \phi(s - \Delta s/2))/\Delta s$$

The discretized equations are

$$\rho\left(\frac{\boldsymbol{u}^{n+1} - \boldsymbol{u}^n}{\Delta t} + \sum_{\alpha=1}^{3} u_\alpha^n D_\alpha^\pm \boldsymbol{u}^n\right) = -\boldsymbol{D}^0 p^{n+1} + \mu \sum_{\alpha=1}^{3} D_\alpha^+ D_\alpha^- \boldsymbol{u}^{n+1} + \boldsymbol{F}^n \tag{7.8}$$

$$\boldsymbol{D}^0 \cdot \boldsymbol{u}^{n+1} = \psi^n \tag{7.9}$$

$$\boldsymbol{F}^n(\boldsymbol{x}) = \sum_{q,r,s} \boldsymbol{f}^n(q,r,s)\delta_h(\boldsymbol{x} - \boldsymbol{X}^n(q,r,s))\,\Delta q\,\Delta r\,\Delta s \tag{7.10}$$

$$\boldsymbol{X}^{n+1}(q,r,s) = \boldsymbol{X}^n(q,r,s) + \Delta t \sum_{\boldsymbol{x}} \boldsymbol{u}^{n+1}(\boldsymbol{x})\delta_h(\boldsymbol{x} - \boldsymbol{X}^n(q,r,s))h^3 \tag{7.11}$$

$$T^n = \sigma(|D_s\boldsymbol{X}^n|; q, r, s) \tag{7.12}$$

$$\boldsymbol{\tau}^n = \frac{D_s\boldsymbol{X}^n}{|D_s\boldsymbol{X}^n|} \tag{7.13}$$

$$\boldsymbol{f}^n = D_s(T^n\boldsymbol{\tau}^n) \tag{7.14}$$

In these equations $u_\alpha^n D_\alpha^\pm$ refers to upwind differencing: the forward difference is used if the convection velocity u^n is negative and the backward difference if the convection velocity is positive. The notation $\sum_{q,r,s}$ refers to a sum over the fiber lattice, while $\sum_{\boldsymbol{x}}$ refers to a sum over the fluid lattice. Finally, the notation δ_h refers to an approximation of the three-dimensional Dirac delta function. The δ_h function used in the 3D model is

$$\delta_h(\boldsymbol{x}) = \frac{1}{h^3}\delta_h\left(\frac{x_1}{h}\right)\delta_h\left(\frac{x_2}{h}\right)\delta_h\left(\frac{x_3}{h}\right)$$

where

$$\delta_h(r) = \begin{cases} \dfrac{3 - 2|r| + \sqrt{1 + 4|r| - 4r^2}}{8}, & |r| \le 1 \\ \dfrac{5 - 2|r| - \sqrt{-7 + 12|r| - 4r^2}}{8}, & 1 \le |r| \le 2 \\ 0, & 2 \le |r| \end{cases}$$

The computational method proceeds as follows. Given the fiber configuration $\boldsymbol{X}^n(q,r,s)$ and the fluid velocity $\boldsymbol{u}^n(\boldsymbol{x})$ evaluate the fiber forces $\boldsymbol{f}^n(q,r,s)$ through the successive use of equations (7.12), (7.13) and (7.14). Then apply the fiber forces to the computational lattice of the fluid using equation (7.10). Then update the fluid velocity by solving the system of equations (7.8) and (7.9) for $(\boldsymbol{u}^{n+1}, p^{n+1})$. This is done by Fourier transforming the equations, solving for the Fourier transforms of $\boldsymbol{u}$ and p, and then applying the inverse Fourier transformation. The details of this is explained in Peskin and McQueen (1996). Finally, interpolate the new velocity field and move the fibers using equation (7.11), and the time step is complete.

This new computational method removes the need to scale all lengths and time by a factor γ as done in the 2D model. Thus, in the 3D model the viscosity (and consequently the Reynolds number) is kept at its physiologically correct value. Peskin and McQueen have improved the computational method even more recently by reducing the numerical viscosity through the introduction of a (formally) second order accurate method (McQueen and Peskin, 2000; Lai and Peskin, 2000).

7.1.3 Initial geometry

The initial geometry of the heart in the 3D model is much more realistic than in the 2D model. It is based on the work by Thomas (1957), who gave a detailed description of the fiber layout of muscle fibers in the ventricles of mammalian hearts and on the work by Streeter et al. (1969; 1978) who made measurements of the distribution of fiber angles in the left ventricular wall. Peskin and McQueen constructs the initial layout of fibers (as best as possible) to mimic the fiber layout described in Thomas (1957) and Streeter et al. (1969; 1978). The details of the initial heart geometry are described in Peskin and McQueen (1996). The initial layout of the heart consist of more than 4000 fibers and approximately 600000 boundary points.

Figure 7.1 shows the initial geometry of the heart. From the figure it is seen

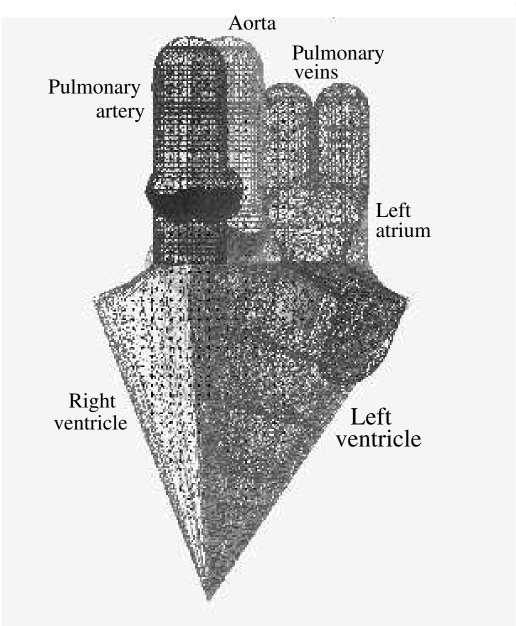

Figure 7.1: Initial geometry of the 3D heart, the right atrium and the inferior and superior vena cava cannot be seen.

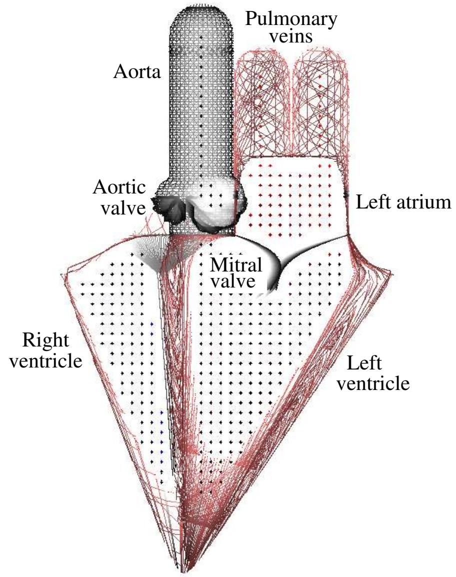

Figure 7.2: Cut-away view of the initial fiber configuration.

that the initial geometry is still simplified compared to a realistic shape of the heart, but the geometry changes quickly to a more realistic shape when the model is run. From Figure 7.1 it is difficult to see the interior of the heart, but in Figure 7.2 a cut-away view of the initial geometry is shown. Here, the mitral and aortic valves can be seen, as well as the initial cone shape of the left ventricle.

The heart in the 3D model is also tethered to fixed points, in a way similar to that described for the 2D model in Section 3.3.7. In the 3D model the fix points are located along the initial positions of the outflow vessels of the heart. The tetherings in the 2D and 3D models were introduced independently.

7.2 Results

A simulation with the 3D model starts in diastole, just as the 2D model, but in the 3D model none of the fibers are under tension at initial time (their resting lengths are equal to their initial lengths). Thus the initial set up is even more unrealistic than in the 2D model. As a consequence of this, the model starts with a long filling phase (it lasts for 3/4 of a heart cycle), then atrial systole sets in and the simulation computes one heart beat. The total simulation time is thus 1.75 heart beats. The long filling in the beginning of a simulation is driven simply by the flow of blood entering from the sources in the atria, because neither stiffnesses nor resting lengths (which determine relaxation and contraction) of the contractile fibers change until the onset of atrial systole.

We performed one simulation with the 3D model where the parameters determining the time course in the model (onset and duration times of ventricular and atrial systole) are identical to the parameters in our reference simulation with the 2D model (see Section 3.3.6). We chose these parameters to (hopefully) be able to match the simulation results with the MR data set we compared the 2D model with (see Chapter 5).

We did not change any other parameter values in the model, so the remaining values are thus as published by Peskin and McQueen (see e.g. Peskin and McQueen, 1996; Peskin and McQueen, 1994). This means that the computations are performed on a $128 \times 128 \times 128$ grid with 32768 time steps per heart beat, giving a total of 57344 time steps corresponding to 1.75 heart beats.

Simulations with the 3D model are computationally very demanding. The simulation presented here takes approximately 580 cpu hours on a Cray C90 and uses 512 MB of memory. The implementation of the code on e.g. the Cray is described in McQueen and Peskin (1997). From this paper it is also seen that the computationally demanding parts are the integration of the Navier-Stokes equations and the interactions between fluid and fiber lattices. Furthermore, during a simulation many output files are produced and subsequently the post processing is also computationally very demanding.

In Figure 7.3 the flow through the mitral and aortic valves during the simulation is shown. The flow through the aortic valve looks as expected: zero flow until the onset of systole, then a large forward peak, followed by a small backward peak at the time of closure of the valve, and finally zero flow. For the mitral valve flow there is a peak at the time of atrial systole, as expected, but this is followed by a long period of time with backflow (negative flow), until the onset of the next diastolic phase, when a forward peak (the E peak) is seen. The long period of backflow is not expected but might be caused by the mitral valves being closed and bulging into the left atrium, i.e. the backward flow may be blood flowing toward the mitral leaflets from the ventricle. We would have expected a larger backflow at the time of the closure of the mitral valve, as seen in the 2D model. This has been seen in other simulations with the 3D model. The last peak in the

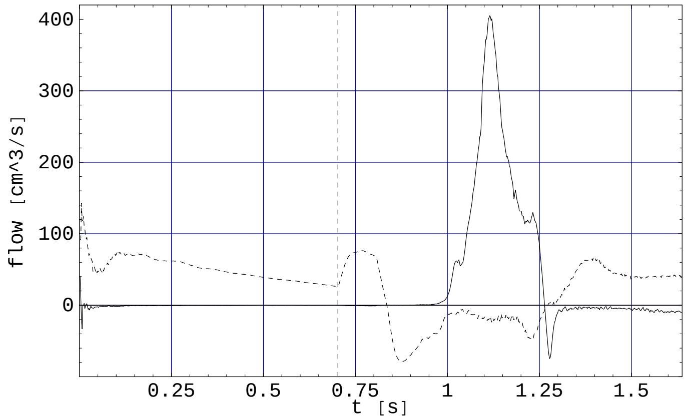

Figure 7.3: Flow time profile of the flow (cm^3/s) through the mitral valve (dashed) and through the aortic valve (solid). Vertical dashed line indicates the time of the long filling phase ($t = 0.702$ s).

mitral flow profile corresponds to the E peak, and this should have been larger than the first peak in the flow profile.

Figure 7.4 shows the time velocity profile for the absolute centre velocity at the aortic valve. Compared to the velocity profile from MR data (Figure 5.5) we see that the peak velocity is much larger in the 3D model, 460 cm/s in the 3D model and 90 cm/s in MR data. The second peak in the simulation profile is caused by backflow at the time of closure of the valve. Thus the time interval the valve is open is approximately 250 ms, which is less than seen in the MR data (approximately 365 ms).

Figure 7.5 shows the time velocity profile for the absolute centre velocity at the mitral valve. This is more difficult to judge than the aortic velocity profile because it is not clear which peaks are related to forward flow and which are related to backward flow. But the first peak after the vertical line must be caused by atrial systole, and we expect the following peak to be related to backflow by the time of closure of the mitral valve. By comparing the time course in Figure 7.3 with this figure, we believe that the last peak seen must be the E peak, which here is approximately 25 cm/s. In the MR data the E peak is approximately 65 cm/s (Figure 5.4). Even if the highest peak seen (approximately 43 cm/s) was caused by maximum forward flow, this is less than the 65 cm/s seen in the MR data. The low peak velocity could be caused by a skewed inflow, but other data from the

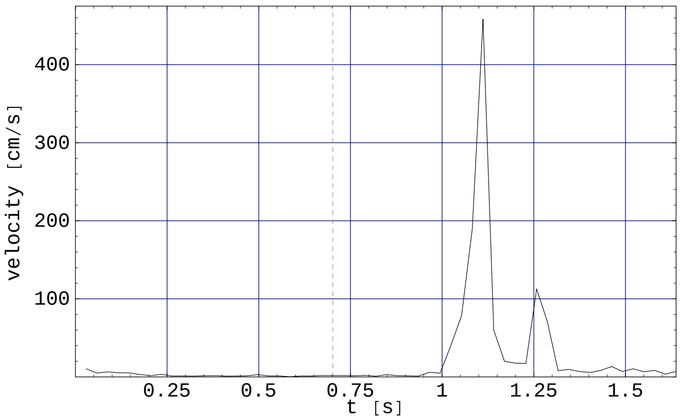

Figure 7.4: Velocity time profile for the absolute centre velocity (cm/s) at the aortic valve. Vertical dashed line indicates the time of the long filling phase ($t = 0.702$ s).

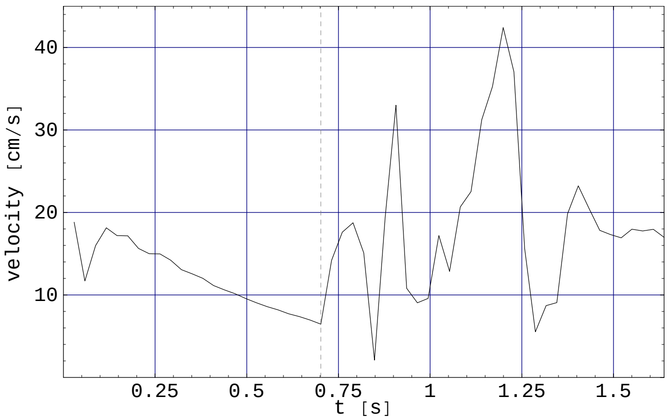

Figure 7.5: Velocity time profile for the absolute centre velocity (cm/s) at the mitral valve. Vertical dashed line indicates the time of the long filling phase ($t = 0.702$ s).

simulation does not support this.

The pressure in the model is not realistic. Especially the pressure in the ventricles is far too high, where a maximum pressure above 1200 mmHg is reached. This is a general problem with the 3D model that has not yet been solved.

Even though the heart is tethered, it is difficult to examine the flow pattern inside the heart because of the movement of the heart. Thus it is difficult to see the vortex pattern in the left ventricle. But in Figure 14.12 in Peskin and McQueen (1996) the flow during early diastolic filling is depicted by streaklines, i.e. trajectories of particles immersed in the flow. The figure is reproduced in Figure 7.6. Here we clearly see a vortex ring forming below the mitral ring. This is also seen in Figure 1 in McQueen and Peskin (2000), which we have reproduced

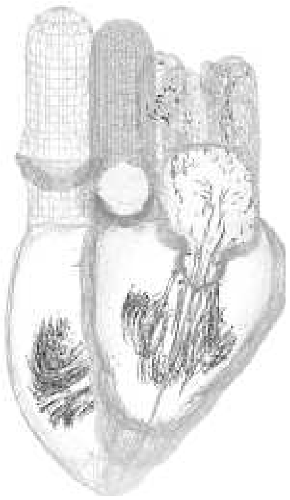

Figure 7.6: Cut-away view of the heart during early ventricular diastole. Note the ring vortex visible in the left ventricle below the mitral valve. From Peskin and McQueen (1996).

Figure 7.7: Section through the left ventricle showing streamlines of ventricular filling. A pair of vortices (cross-section of a vortex ring) has been shed from the mitral leaflets and has migrated downwards towards the apex of the left ventricle. From McQueen and Peskin (2000).

in Figure 7.7. In this figure the flow is shown as streamlines, which are computed by choosing a time of interest, fixing the velocity field at that given time, and computing and plotting what the trajectories of particles would be if the particles were to move in that (time-independent) velocity field. Both of the figures clearly show the formation of a vortex ring below the mitral valve, and when cutting through the ring we see a pair of vortices, similar to what we see in the 2D model, see Figure 5.1.

7.3 Discussion

The results presented in this chapter show that the 3D model has to be adjusted and improved before a reasonable comparison with MR data can be obtained. This is not a surprise, since it took a long time to find a good parameter setting in the 2D model, and the 3D model is even more complex. But it was hoped that because the 3D model was based on a realistic, human heart the results would have been reasonable without too many parameter changes.

Parameters determining the time course, the contraction and relaxation of the fibers, the pre- and afterload and possibly the geometry of the valves have to be adjusted to improve the comparison between model and MR data. But simulations with the 3D model are computationally very demanding, also in the post processing step. Thus it is not realistic to achieve a better parameter setting for the model within a reasonable time period.

Even if the comparison with one specific MR data set is not good, we can still obtain valuable insights into the flow pattern, particularly in the left ventricle, from the 3D model. Because the model is 3D and the geometry of the left ventricle is very realistic we can use the model to examine the vortex pattern during filling. From the results reproduced here, we see that a vortex ring forms during diastole and a cut-away view of this shows a vortex pair, exactly as seen in the 2D model. This supports the idea of the vortex pattern being a 3D phenomenon as indicated by the MR data in Chapter 5.

Chapter 8

Conclusions and suggestions

The purpose of this Ph.D. project has been to achieve a better understanding of the hemodynamics of the heart using a computational model and MR data. We have presented a 2D computational model of the blood flow in the left side of the human heart, which was constructed by introducing modifications and improvements to Peskin and McQueen's 2D heart model dimensioned to a dog's heart. These modifications and improvements were based on physiological knowledge and comparisons with MR data on humans.

8.1 Summary of conclusions

We compared output from our 2D model with an MR velocity data set. In particular, we examined the intraventricular velocity fields and the velocity times curves over the mitral ring and across the aortic outflow tract. We found reasonable agreement between the general flow pattern from the simulation and the MR data: a wide inflow jet during filling, the formation of an anterior vortex, and a wide outflow jet during ejection. However, there were differences in the details of the two flow patterns, particularly in the vortex formations. In the simulations the vortices were more distinct and the velocity in the vortices was higher. Furthermore, we saw three vortices in the simulation but only two in the MR data. The third vortex in the simulation is probably unphysiological, and it would improve the model considerably if it could be removed.

The time course of diastole and systole in the simulation was fairly good: the timing of atrial systole and the onset of ventricular systole were set reasonably well, but the duration of systole could be further improved by extending it.

The velocity time profiles at the mitral ring and aortic tract from the simulation matched reasonably well with MR data. The timing of the profiles was very good, while the shapes and maximum values differed some what.

The connection between the simulation results and the parameters in the model is very complex, and we believe that improvements can be achieved by further parameter adjustments. However, the reasonable comparison with MR data justifies using the model for investigations of the hemodynamics of the heart.

We implemented a gradual activation of the heart muscle, i.e. propagation of the activation across the heart wall with a given velocity, which resembles the activation of the heart muscle in the normal heart. We found that this did not affect the simulation results much, and the results were very sensitive to the activation of the papillary muscle.

We performed an investigation of certain mechanisms affecting the diastolic functioning of the heart by examining the flow pattern during early filling. We found reasonable agreement between simulation results and MR data for a healthy human. In particular, the pressure difference that drives the filling of the ventricle was in agreement with clinical data.

We were not able to simulate the changes seen clinically in the flow pattern in a local ischemic condition by letting the apical region relax more slowly than the rest of the ventricle. However, we successfully simulated a global ischemic ventricle by letting the entire ventricle relax more slowly than in the healthy heart. We found lower peak velocities and delayed filling in this situation compared with a simulation of a healthy human. These changes are similar to measured data on healthy dogs and dogs in a global ischemic condition. Furthermore, we were able to simulate acute myocardial infarction (AMI) by letting the apical region be inactive. Here the velocity data from the simulation matched those obtained by MR measurements in AMI patients. However, the driving pressure difference was not in good agreement with clinical data.

We have shown that our anatomically simple 2D model is able to capture some of the changes seen during pathological heart conditions. The model can be used to study mechanisms that introduce major differences in the flow pattern, while simulations of less severe conditions do not alter the flow pattern compared with the flow pattern from a simulation of a healthy person.

We have presented Peskin and McQueen's 3D model of the entire heart and briefly compared its results with an MR velocity data set. This showed that the model has to be further improved before a reasonable agreement can be obtained. In particular, the flow and velocity over the mitral ring is not in agreement. Furthermore, since the 3D model is computationally very demanding it is not very useful as a tool for hemodynamic investigations of the heart. However, from the simulation results we still gain insight into the 3D nature of the flow pattern inside the heart. The results show a clear vortex ring forming below the mitral ring during filling.

8.2 Suggestions for future work

Suggestions for future work can be divided in two parts: future work with the model presented in this thesis and future work with heart simulations in general.

We believe that the 2D model presented in this thesis can still be of importance in understanding the hemodynamics of the heart if its limitations are kept in mind. The following scenarios could be simulated and investigated in the 2D model:

- Diastolic functioning. The investigations presented in this thesis could be extended e.g. by simulating increased stiffness in part of the ventricular wall due to an infarction.
- Hypertrophic cardiomyopathy (HCM). This conditions, which is characterized by increased growth of the left ventricular wall, can be simulated in the model by raising the stiffnesses S_{pe}, S_{se} and S_0 in the muscular model (see Section 3.3.5).
- Mitral valve stenosis. This narrowing of the mitral valve can be simulated by introducing one or several cross links between the two mitral valve leaflets.
- Mitral valve regurgitation. This is backflow of blood from the ventricle to the atrium due to mitral valve insufficiency and can be simulated by introducing bending resistance in the mitral leaflets, which would cause them not to close. Bending resistance can be introduced by the procedure described in Peskin and McQueen (1980) on modelling prosthetic heart valves.

The results presented in this thesis support the idea of computational models as a tool for understanding the hemodynamics of the heart. However, since the intraventricular flow pattern is three dimensional, future work should eventually be performed with a 3D model. We believe that this would not have to be a computationally demanding model of the entire heart, like the model of Peskin and McQueen. Instead, a simpler 3D model of the left side of the heart would be enough to meet the demands of a hemodynamic tool. The work presented here has shown that an (anatomically) simple 2D model can, within limits, predict physiologically correct flow patterns. Thus a simple 3D model should also be able to do this and even better. Such a 3D model should be evaluated and validated in detail by comparison with MR velocity data. Once this is done, the model could be used for investigations similar to those presented in this thesis and to those suggested above for future work with the 2D model.

Appendix A

Magnetic resonance imaging

This appendix provides an introduction to magnetic resonance imaging (MRI). It provides the reader with a knowledge on how the MRI data used in the thesis is recorded. It describes the basics of MRI: spin of nuclei, excitation, relaxation and pulse sequences used in MR scanning. It also describes the imaging process: how MRI is created, choice of scan area, spatial encoding and imaging sequences in MRI. Finally, velocity measurements with MRI using velocity encoding is described. The main source for this appendix is Philips (n.d.).

A.1 Basics of MRI

The principle of MR scanning is based on the magnetic properties of nuclei with an uneven atomic mass or atomic number, e.g. ^1H. Such nuclei possess angular momentum and have a characteristic spin quantum number greater than zero. The spin induces a magnetic field with an axis coincident with the axis of spin, and with a magnitude and direction represented by the magnetic dipole moment, or dipole vector, μ, see Figure A.1.

Normally, the dipole vector of a nucleus is ordered randomly. But, when an external magnetic field is applied the dipole vector is aligned in parallel or antiparallel direction with the applied field. In the presence of an external magnetic field the dipole vector of the nucleus experiences a torque, which causes it to rotate (or precess) around the axis of the external field with a certain frequency. This phenomenon is called Larmor precession, see Figure A.2.

The rate of precession depends upon the physical characteristics of the nucleus and the strength, B_0, of the magnetic field. This is expressed in the Larmor

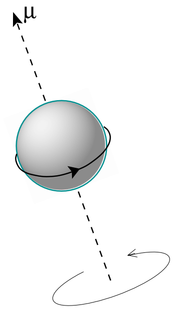

Figure A.1: A spinning nucleus with its dipole vector μ when no external magnetic field is applied. The spin axis coincides with the dipole vector.

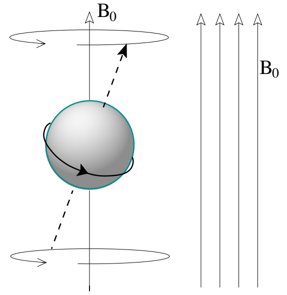

Figure A.2: Precession of the dipole vector of a spinning nucleus about an external magnetic field B_0.

equation

$$\omega = \gamma B_0,$$

where ω is the Larmor frequency, γ is the gyromagnetic ratio specific to the nucleus and B_0 is the strength of the external magnetic field. Since γ is specific to each nucleus the Larmor frequency is thereby also specific to each nucleus. e.g. for the hydrogen nucleus, ^1H, the Larmor frequency is 42.5759 at an external magnetic field of 1 T (Schlaikjer and Kolenda, 1997). Larmor precession is a resonance phenomenon. If a system has a natural resonance, energy can be most efficiently transferred to the system at this frequency.

In MR imaging it is mainly the ^1H nucleus (the proton) that is considered. We therefore limit ourselves to this case in the following.

Considering a collection of protons in a volume in the absence of an external magnetic field. The individual dipole vectors are ordered randomly and thus the net magnetic moment, M_0, is zero. In the following we refer to the net magnetic moment as the magnetization vector. When an external magnetic field B_0 is applied the dipole vectors will tend to align parallel or antiparallel to the applied field. There is a slight excess favouring the parallel direction (the low energy state), and thus the magnetization vector M_0 is non-zero and is oriented in the direction of the applied magnetic field. There is no transverse component since the individual precessing protons are randomly oriented with respect to the phase of their precessional motion.

We now introduce a coordinate system where the $z-$axis is parallel to the direction of the external magnetic field B_0. We can then think of the magnetization vector as having two components: M_{xy} in the transverse plane and M_z in the longitudinal plane. In the equilibrium state we have $M_z = M_0$ and $M_{xy} = 0$. In this state the magnetization vector is static and does not induce a current, i.e. we cannot obtain any signal from the volume under observation. In order to obtain a signal, the spins have to be perturbed and leave the equilibrium state.

A.1.1 Excitation

The equilibrium state can be left by exposing the spin system to a radio frequency (RF) pulse in the form of a time varying magnetic field B_1. B_1 is made to be perpendicular to the static field B_0 and varies with the Larmor frequency. The B_1 field, which is turned on only for a short period of time, is produced by a coil with its axis in the $xy-$plane. The static field is typically of the order of 0.1-1.5 T, while the excitation field is of the order of 1 mT.

The effect of applying the B_1 field is that the magnetization vector also precesses about this second field and rotates away from the vertical direction toward the $xy-$plane. The B_0 field still affects the magnetization vector and makes it precess about the $z-$axis, so the total effect is that, while the RF pulse is turned on, the magnetization vector performs a spiralling motion on a sphere as sketched in Figure A.3.

When observing the situation in a coordinate system (x', y', z) that rotates about the $z-$axis with the Larmor frequency, the effect of applying B_1 is seen as simply flipping the magnetization vector toward the $x'y'-$plane. The length of the magnetization vector is practically constant during the short period of time the RF

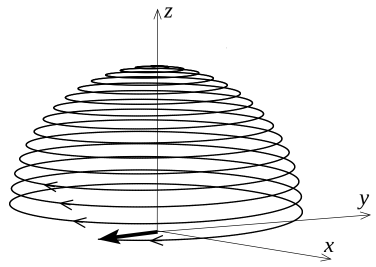

Figure A.3: Spiralling motion of the magnetization vector during an RF pulse.

pulse is on. The final flip angle θ can be calculated by $\theta = \gamma B_1 t$, where γ is the gyromagnetic ratio and t is the duration of the RF pulse. Thus the final position of the magnetization vector in space after the RF pulse is turned off depends on the magnitude of the B_1 field and the duration of the RF pulse.

After excitation the magnetization vector's precession induces a current called the MR signal. The coil producing the B_1 field can also be used to sample this signal. When sampling an MR signal only the component in the $xy-$plane can be detected. Thus the maximum MR signal is obtained at a flip angle of $90°$. In MRI typically two excitations are interesting: the $90°(\pi/2)$ and the $180°$ (π) pulses. The names refer to the flip angle of the magnetization when the RF pulse is turned off. Thus the $180°$ pulse is an inversion of the magnetization vector.

A.1.2 Relaxation

After excitation the nuclei return to the equilibrium state. This process is called relaxation and begins at the termination of the RF pulse. During relaxation both the longitudinal (M_z) and the transverse (M_{xy}) components return to their equilibrium values. The longitudinal and transverse relaxations are mutually independent. In Figure A.4 the time variation of the length of the longitudinal and transverse components of the magnetization vector during relaxation is shown. The magnetization vector returns to its equilibrium value in an exponential fashion as indicated in Figure A.4.

The longitudinal relaxation (often referred to as spin-lattice relaxation) is related to how fast the nuclei emit energy through interaction between the spins and the lattice. In MRI the lattice is the magnetic and thermal environment of the nuclei. The time variation of the longitudinal magnetization vector during relaxation is given by $M_z = M_0\left(1 - e^{-t/T_1}\right)$ characterized by the time constant T_1, see the top panel of Figure A.4. In biological tissue T_1 ranges from about 50 milliseconds to a few seconds.

Transverse relaxation (or spin-spin relaxation) is related to the interaction of individual spins causing local variations in the static magnetic field B_0. These variations lead to fluctuations in the precessional frequency of the individual nuclei. This results in a gradual and random dephasing of the spins and hence in a decay in the magnitude of the transverse component of the magnetization vector. Figure A.5 shows the dephasing of spins after an $90°$ RF pulse. The time variation of the transverse magnetization vector during relaxation is given by $M_{xy} = M_0 e^{-t/T_2}$, where T_2 is the transverse relaxation time constant. T_2 is always smaller than T_1 and is typically in the range of a few milliseconds to a few seconds in biological tissue.

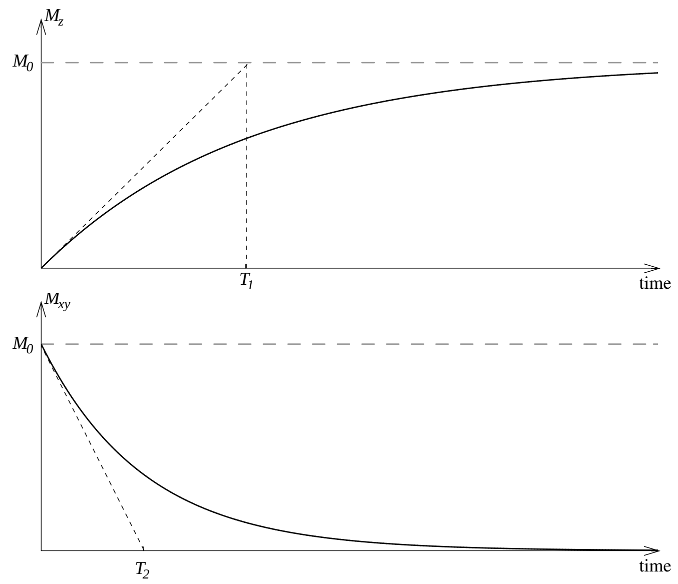

Figure A.4: The time variation of the length of the magnetization vector during relaxation. Top: longitudinal relaxation; bottom: transverse relaxation. Relaxation constants T_1 and T_2 are shown.

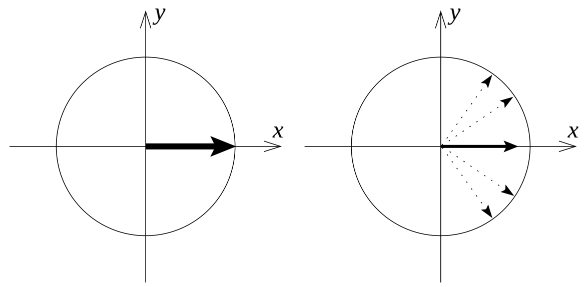

Figure A.5: Dephasing of spins after a $90°$ pulse. Left: immediately after the RF pulse; right: some time after the RF pulse, when the spins are out of phase and the magnetization vector has decayed.

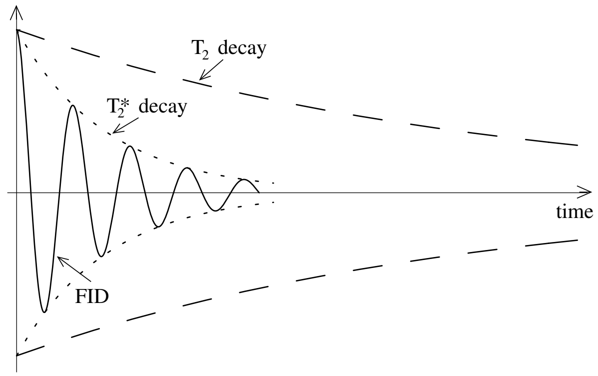

Figure A.6: Time variation of the FID with the T_2^* and T_2 decay shown.

The relaxation time constants depend on the fact that different tissues have different courses of relaxation. These differences are the basis for the MRI scanning.

The transverse component M_{xy} induces a current (a signal) which is called the Free Induction Decay (FID). The coil used to create the B_1 field (with its axis in the $xy-$plane) can also be used to sample the signal in the $xy-$plane after the excitation pulse is terminated. In the sampling, amplitude, frequency, phase and decay are detected. The amplitude of the MR signal decays exponentially with a time constant T_2^*, due to both spin-spin (transverse) relaxation and magnetic field inhomogeneities. T_2^* is smaller than T_2. Figure A.6 shows the time variation of the FID with both the T_2^* and the T_2 decays shown.

A.1.3 Pulse sequences

It is important to bear in mind that the MR signal depends on both T_1 and T_2, but it is possible, through the use of pulse sequences, to obtain an MR signal that depends primarily on either T_1 or T_2.

A pulse sequence is a set of RF pulses used in conjunction with a signal sampling. There are several pulse sequences available. The individual sequences are characterized by giving an MR signal whose intensity depends primarily on either T_1 or T_2. This is called a T_1 or T_2 weighted MR signal. For a T_1 weighted signal the saturation recovery or inversion recovery sequences are available, and for a T_2

weighted signal the spin echo sequence is available. In this section the spin echo sequences will be presented as an example of a pulse sequence.

Spin echo

The FID signal follows a T_2^* decay caused by both spin-spin relaxation (T_2 decay) and by magnetic field inhomogeneities, see Figure A.6. Thus the FID signal alone cannot be used to measure true T_2 relaxation. However, spin-spin relaxation is a random and irreversible process, while field inhomogeneities are static and can be accounted for, and this is exploited in the spin echo pulse sequence. This sequence aims at eliminating the influence of the field inhomogeneities, leaving only the true T_2 relaxation.

The sequence starts with a 90° RF pulse that flips the magnetization vector into the $xy-$plane. Immediately after, the relaxation process sets in: the transverse component M_{xy} decays following the T_2^* decay. The effect of the static magnetic field inhomogeneities causes the individual spins to precess out of phase (dephase), see Figure A.7b–c. At $t = \mathrm{TE}/2$ (TE is the echo time) a 180° pulse is applied. This pulse inverts all the spins, which is seen as a mirroring in the $xy-$plane, see Figure A.7c–d. After this pulse, the field inhomogeneities still in-

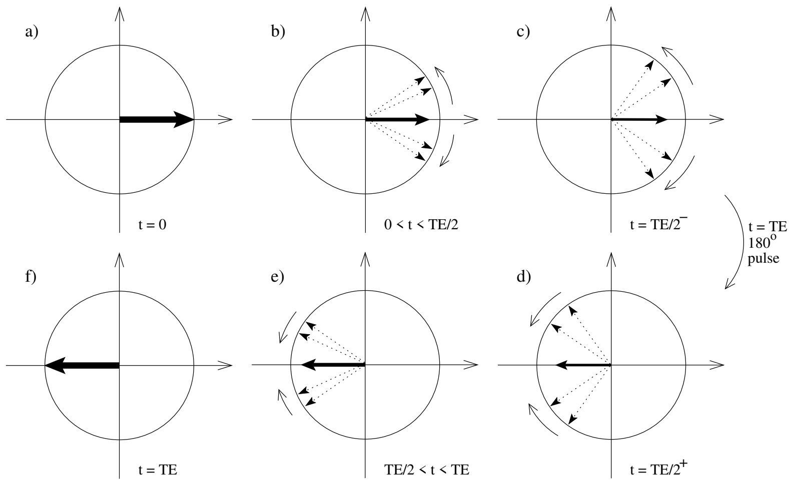

Figure A.7: The spin echo sequence: dephasing of spins due to the field inhomogeneities and the elimination of the effect of these by a 180° pulse.

fluence the spins, but now it causes them to rephase because of the inversion, see Figure A.7d–f. At time $t = \mathrm{TE}$ the spins are once again in phase and the MR signal can be sampled. The echo signal (MR signal at $t = \mathrm{TE}$) has a smaller amplitude than the signal at $t = 0$, due to the spin-spin relaxation. The spin-spin relaxation is not affected by the inversion pulse because it is random and irreversible. The signal decay from $t = 0$ to $t = \mathrm{TE}$ is then a measure of the true T_2 relaxation.

If subsequent 180° pulses are applied, at $t = 1/2\mathrm{TE}, 3/2\mathrm{TE}, 5/2\mathrm{TE}, \ldots$ and the signal sampled at $T = \mathrm{TE}, 2\mathrm{TE}, 3\mathrm{TE}, \ldots$ the sampled signal will continue to decay according to the true T_2 relaxation and the T_2 relaxation can be determined with higher accuracy. Figure A.8 shows the time variation of the signal amplitude during a spin echo sequence.

A particular volume being scanned is often composed of several tissues and the sampled MR signal is a sum of the signals from the individual tissues. Each tissue has different relaxation time constants and this is exploited in the pulse sequences, e.g. in the choice of TE in the spin echo sequence. The optimal TE is a time value such that the difference between the signal amplitudes of the individual tissues is large. Signal sampling at the optimal time results in an image

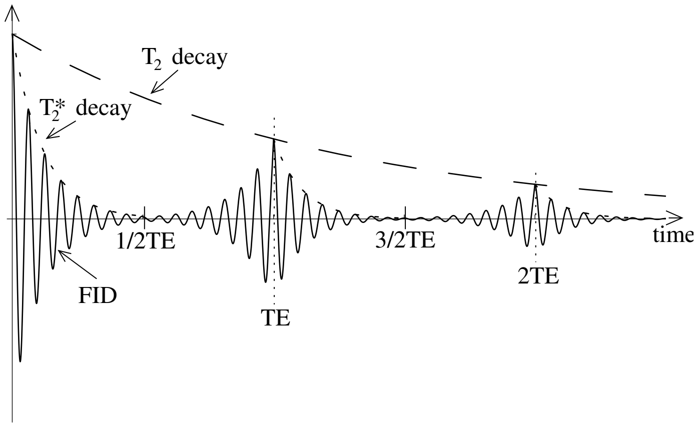

Figure A.8: Time variation of the MR signal amplitude during a spin echo sequences. 180° pulses are applied, at $t = 1/2\mathrm{TE}, 3/2\mathrm{TE}, 5/2\mathrm{TE}, \ldots$ and the signal is sampled at $T = \mathrm{TE}, 2\mathrm{TE}, 3\mathrm{TE}, \ldots$.

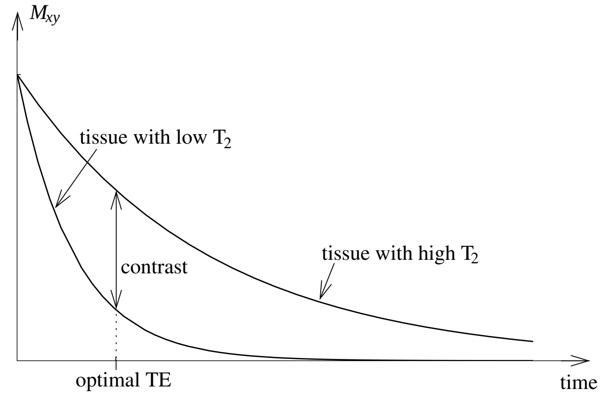

Figure A.9: Transverse relaxation curve for two tissues with different T_2 values. In a spin echo sequence the optimal echo time is at t_{opt} where the difference between signal amplitudes is large.

where there is a large contrast between the individual tissues when the signal is transformed into an image (see Section A.2). Figure A.9 shows the transverse relaxation curves for two different tissues (with different T_2 values) with the optimal TE indicated.

A.2 Imaging methods

The situation described in the previous section is that where the entire volume under observation is excited. Since the sampled MR signal is a result of the relaxation process in the entire volume, it contains no spatial information. In order to construct an MR image the signal has to be spatially encoded. The spatial encoding is achieved using the fact that the Larmor frequency depends on the magnetic field strength. If the magnetic field varies with position in a controlled way, the resonance frequency of the individual spins varies accordingly. Thus spins can be picked out and excited by their position in space.

In an MR scanner three sets of coils are present, the main coils, which create the static magnetic field B_0, the high frequency coils, which emit the RF pulses and sample the MR signal, and finally the gradient coils, which are used to control the spatial variation of the magnetic field. The gradient coils create a magnetic field which is parallel to the main field B_0. If we assume, as previously, that the main field is parallel to the $z-$axis we have

$$B_z = B_0 + G_x x + G_y y + G_z z$$

where G_x, G_y and G_z are magnetic field gradients in the $x-$, $y-$ and $z-$directions, respectively. The gradient field is weak compared to the static magnetic field, being typically in the range 1–10mT/m (Andersen, 1997). The three gradient fields are often referred to as the slice selection gradient, the read-out or frequency encoding gradient, and the phase encoding gradient, because of their functions in an MRI sequence.

A.2.1 Slice selection gradient

If a gradient is turned on while the volume is being exposed to an RF pulse containing a given range of frequencies, only the slice which contains spin with a Larmor frequency that matches the frequencies in the pulse will be excited.

The thickness of a slice is determined by the bandwidth of the RF pulse (i.e. the range of frequencies in the pulse). The slice selection gradient field is perpendicular to the slice direction and can be chosen in any given direction. The MR image is constructed by a Fourier analysis of the sampled MR signal. E.g. if we use a slice selection gradient parallel to the $z-$axis in combination with a spin echo sequence of pulses, the Fourier transform of the MR signal will be a projection of a T_2 weighted signal from the entire selected slice onto the $z-$axis. But there is no spatial resolution of the selected slice.

The Fourier connection between MR image and RF pulses (through the sampled signal) influences the choice of RF pulse. When a sharp rectangular slice

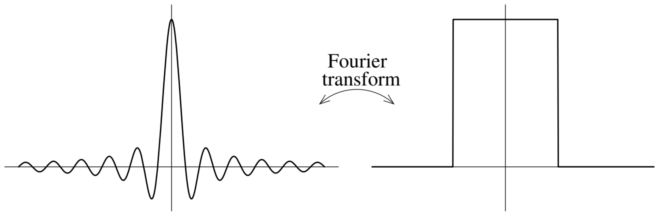

Figure A.10: A sinc wave pulse and its Fourier transform: the step function. The sinc wave is a decaying sine wave: $sinc(t) = sin(\pi t)/(\pi t)$

profile is needed the RF pulse should be a decaying sinc wave, since the sinc wave and the step function are each others Fourier transforms, see Figure A.10.

The magnetic field influencing the spins inside the selected slice will vary slightly because of the gradient. The frequency of the individual spins will then vary accordingly, and thus they will dephase. To achieve the maximal signal the spins are rephased by applying a magnetic field gradient with the opposite polarity of the slice selection gradient. This is called a rephasing gradient.

With the slice selection gradient, a particular slice to be excited has been picked out but no information on how that slice is spatially resolved is obtained.

A.2.2 Phase encoding gradient

After the slice selection and rephasing gradients have been applied along with the RF pulse all spins in the selected slice precess at the same frequency and in phase. If a second gradient, the phase encoding gradient, is then turned on, e.g. in the $y-$direction, the resonance frequency of the spins changes along the $y-$axis and the rate of precession changes accordingly. When the phase encoding gradient is then turned off, the spins once again precess at the same frequency, but now their phases are no longer the same. The individual spins have a phase that depends on their position along the $y-$axis.

A.2.3 Read-out gradient

If a third gradient, the read-out or frequency gradient e.g. in the $x-$direction, is applied while the MR signal is being sampled, the frequency of the emitted signal varies according to its position along the $x-$axis. The signal at a specific frequency along the $x-$axis is a sum of all spins in a row along the $y-$axis (where there is a phase variation).

The signal is sampled at N_x points in the read-out (or $x-$) direction. The measurement is repeated N_y times for different values of the phase encoding ($y-$) gradient, thus generating a matrix of $N_x \times N_y$ signal points. Performing a 2D Fourier transform of the matrix yields a 2D spectrum whose intensity is a value of the signal distribution in the imaging slice. The typical final MR image is a grey-scale representation of the spectrum. Figure A.11 shows an MR spectrum and its corresponding grey scale image.

The image matrix determines the number of pixels in the MR image, and the colour of each pixel represents the intensity of the MR signal from the corresponding volume element, or voxel. The volume of a voxel is determined by the matrix size divided by the field of view (actual size of image in mm) multiplied by the

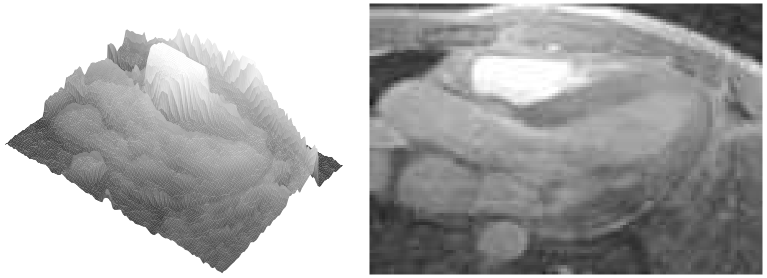

Figure A.11: MR spectrum and corresponding grey scale image.

slice thickness. The MR signal from a voxel is the average of the signal from all the nuclei in that voxel.

The above procedure for obtaining an MRI is just an example, and alternative procedures are available. An MRI could e.g. also be obtained as a volume image/3D image. In a volume image the entire volume is excited (i.e. no slice selection during excitation) and to obtain a slice selection a second phase encoding gradient is applied. The advantages of this method is that noise is reduced, slice thickness can be reduced, and spatial resolution in all three directions can be identical, i.e. isotropic voxels.

A.2.4 Imaging sequences

The process of creating an MRI is done on the basis of an imaging sequences. Imaging sequences describe the RF pulses, the application of gradient fields and the timing of MR signal aquisition. Thus an imaging sequence is an extended pulse sequences, which was described in Section A.1.3. An imaging sequence typically consists of three parts: spin preparation, signal production and image generation. Where image generation simply is Fourier transformation of the MR signal.

Spin preparation

In spin preparation RF prepulses or magnetic field gradients are employed to change the characteristics of the MR signal. Spin preparation can consist of prepulses (e.g. an inversion pulse) or it can be saturation of part of the volume, saturation being a long term excitation. The result is that the magnetization vector approaches zero and during the following excitation pulse only the volume outside the saturated part is excited (Andersen, 1997). Through the use of an inversion prepulse in the spin echo sequence it is possible to generate images that are T_1 weighted and not T_2 weighted as a standard spin echo sequence.

Signal production

Signal production consists of generating the MR signal and encoding it with spatial information. This can be done in three ways: FID, spin echo and gradient echo. A FID generated signal is a sampling of the FID signal. This gives an image where image intensity is proportional to the net equilibrium magnetization vector. The spin echo generated signal is a combination of the spin echo pulse sequence described in Section A.1.3 and the the MRI procedure described in Sections A.2.1-A.2.3. The pulse sequence is repeated N_y times to obtain the full spatial information. The time between successive excitation pulses is called the repetition time TR. Thus the full scan time is $N_y \times$TR. The gradient echo generated signal is based on a combination of the gradient echo sequence and the MRI procedure described above (Sections A.2.1-A.2.3). The gradient echo sequence is described in the following section.

Gradient echo sequence

In the gradient echo sequence a magnetic field gradient is used to create an echo, as opposed to the use of a 180° pulse in the spin echo sequence.

In the gradient echo sequence a gradient is applied in the read-out direction, e.g. the $x-$direction, for a limited time directly after the excitation pulse. This makes the spin precess at different rates along the read-out direction, resulting in a dephasing of spins. The gradient is then reversed, which causes spin to rephase and create an echo.

Figure A.12 sketches the gradient echo sequence. An excitation pulse with flip angle α is applied at the same times as the slice selection gradient in the $z-$direction. Immediately following the slice selection gradient is the rephasing gradient in the slice selection direction, see Section A.2.1. Then the phase encoding gradient is turned on (in this case in the $y-$direction) at the same time as the echo gradient in the read-out direction ($x-$direction). The echo gradient consists of two parts with reversed polarity (as described above). After the echo gradient the echo is created and the signal is sampled in the read-out direction at the same time as the read-out gradient is applied. This sequence is repeated N_y times with different values of the phase encoding gradient. This is illustrated in the figure by

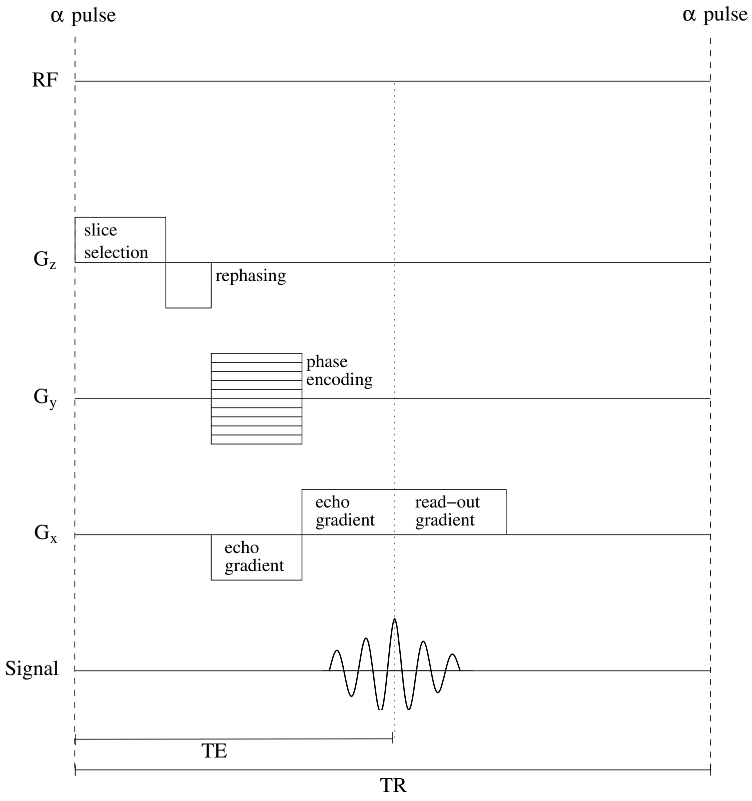

Figure A.12: The gradient echo sequence.

several lines drawn at the phase encoding gradient. The echo time, TE, and the repetition time, TR, are indicated.

The advantages of the gradient echo sequence, compared to the spin echo sequence, are the possibility of smaller pulse flip angles, shorter echo times and shorter repetition times, yielding a much shorter total imaging time.

In the spin echo sequence the repetition time has to be long to assure that the longitudinal relaxation is complete before the next excitation pulse is applied. If the longitudinal relaxation is not complete the effective magnetization vector flipped into the $xy-$plane is smaller. After several excitations the magnetization vector decays toward zero and the volume becomes saturated (refer to Section A.2.4 above). The repetition time could be reduced by using an excitation pulse with a smaller flip angle than 90° (e.g. 15-45°), making the time to restore longitudinal relaxation smaller. But even in the case of a pulse with a low flip angle a large part of the net magnetization is in the longitudinal direction. With a 180° inversion pulse this would also affect the longitudinal magnetization and not only the transverse magnetization.

In the gradient echo sequence it is possible to use pulses with shorter flip angles because the echo is created by a gradient rather than an inversion pulse. Lower flip angles lead to shorter recovery time of the longitudinal magnetization (prior to the next excitation pulse). This shortens the TR and thereby the total imaging time. This is the primary argument for using a gradient echo sequence rather than a spin echo sequence.

A.2.5 Motion artifacts

Motion results in ghosting or blurring of the MR image. In the present context motion usually means patient movements, respiratory or cardiac motion or motion due to swallowing. Depending on the type of MR image being recorded different motions are unwanted. E.g. if the brain is being mapped cardiac or respiratory motion is not a problem. Since this thesis is concerned with cardiac MRI we describe the procedures for eliminating the effect of patient movements, as well as cardiac and respiratory motion.

Signal averaging: Because of the random nature of patient movement the effect can be reduced by averaging the MR signal over several samplings. The drawback is that the total imaging time is increased.

Cardiac triggering: The effect of cardiac motion can be eliminated by coupling the aquisition to a trigger signal, in the cardiac case the ECG (electrocardiogram) signal. The heart cycle is assumed periodic and by triggering on e.g. the R peak of the ECG, aquisition is done at the same time in the heart cycle every time and the effect of cardiac motion is minimized. The drawback is that total imaging time is substantially increased.

Respiratory triggering: This is similar to cardiac triggering except that here the triggering is related to a signal indicating expiration.

Respiratory gating: Aquisition is done while the respiratory motion is minimal. This is an effective procedure but increases the total imaging time substantially.

Breath hold: In a short aquisition sequence the aquisition can be done while the patient holds his/her breath, thereby eliminating the effect of respiratory motion.

A.3 Velocity measurements

All the MR images described previously are grey scale images of the intensity of the MR signal. They are often referred to as magnitude or modulus images. It is also possible to obtain information on the velocity of the tissue (e.g. blood) in each voxel in an MRI.

The phase of spins in blood are altered by the blood flow, a phenomenon called a phase shift. This can be exploited in a phase velocity map where the phase of the spins are correlated to the velocity of the moving spins.

When a moving spin is subjected to a bipolar gradient the spin has a phase at the termination of the gradient which is proportional to the velocity of the spin. This is opposed to a static spin, which has no net phase at the termination of a bipolar gradient. So by applying a bipolar gradient in an image sequence it is possible to record the velocity of the blood in each voxel. The bipolar gradient can be applied in any chosen direction, or in all three spatial directions to obtain three dimensional velocity information.

A phase shift can have other causes than flow velocity, e.g. magnetic field inhomogeneities. Thus it is necessary to record a flow-compensated background image. Through the use of flow-compensated gradients it is possible to record a phase image, where phase effects stem only from unwanted deviations. This flow-compensated image can then be subtracted from the phase velocity map, leaving a phase image which is the result only of flow velocity phase shifts.

Phase velocity mapping requires obtaining several images per slice: one image per velocity component and one velocity-compensated image. Thus it increases the total scan time. Figure A.13 shows three images from a velocity encoded cardiac MRI: the modulus image, the velocity image (with velocity vectors from the in-plane components) and the velocity image superimposed on the modulus image.

The velocity image is of limited value on its own, but it is very useful when it is superimposed on the modulus image. This combination is a very strong imaging technique when e.g. the cardiac function is evaluated.

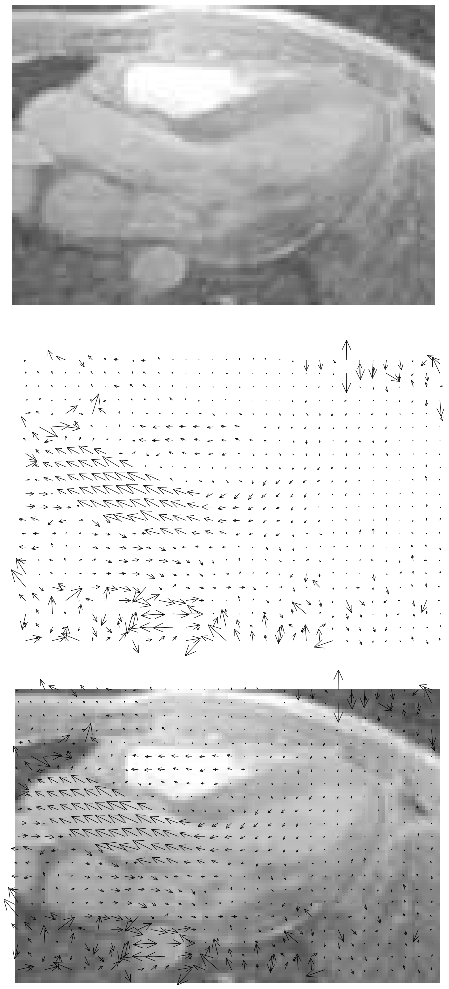

Figure A.13: Images from a cardiac MRI with velocity encoding. Top: the modulus image, middle: the velocity image with in-plane velocity components shown as vectors, bottom: velocity image superimposed on modulus image. The anatomy of the heart seen on the MRI is explained in Figure 6.5.

Bibliography

Adeler, P. T. and Jacobsen, J. M. (2001). Blood flow in the heart, *in* J. T. Ottesen, M. S. Olufsen and J. Larsen (eds), *Applied Mathematical Models in Human Physiology*, to be published by SIAM, chapter 3.

Andersen, O. T. (1997). Billeddannelse med NMR (in Danish), *Medicinsk Elektronik (in Danish)*, Institut for Informationsteknologi, Technical University of Denmark, chapter 11.

Beyer, R. P. (1992). A computational model of the cochlea using the immersed boundary method, *J. Comput. Phys.* **98**(1): 145–162.

Beyer, R. P. and LeVeque, R. J. (1992). Analysis of a one-dimensional model for the immersed boundary method, *SIAM J. Numer. Anal.* **29**(2): 332–364.

Börgers, C. and Peskin, C. S. (1987). A lagrangian fractional step method for the incompressible Navier-Stokes equations on a periodic domain., *J. Comput. Phys.* **70**(2): 397–438.

Cappello, A., Gnudi, G. and Lamberti, C. (1995). Identification of the three-element windkessel model incorporating a pressure-dependent compliance, *Annals of Biomedical Engineering* **23**(2): 164–177.

Chorin, A. J. (1968). Numerical solution of the Navier-Stokes equations, *Math. Comp.* **22**: 745–762.

Chorin, A. J. (1969). On the convergence of discrete approximations to the Navier-Stokes equations, *Math. Comp.* **23**: 341–353.

Davis, P. (1995). The art of the heart valve, *SIAM News* **28**(5): 1 and 13.

Despopoulos, A. and Silbernagl, S. (1991). *Color Atlas of Physiology*, 4th edn, Thieme, Stuttgart.

Ding, T. and Schoephoerster, R. T. (1997). Evaluation of global left ventricular function based on simulated flow dynamics computed from regional wall motion, *ASME, Bioengineering Division (Publication) BED* **35**: 193–194.

Fung, Y. C. (1993). *Biomechanics. Mechanical Properties of Living Tissues*, 2nd edn, Springer-Verlag, New York.

Ganong, W. F. (1993). *Review of Medical Physiology*, 16th edn, Prentice-Hall International, London.

Georgiadis, J. G., Wang, M. and Pasipoularides, A. (1992). Computational fluid dynamics of left ventricular ejection, *Annals of Biomedical Engineering* **20**(1): 81–97.

Gonzalez, E. and Schoephoerster, R. T. (1996). A simulation of three-dimensional systolic flow dynamics in a spherical ventricle: Effects of abnormal wall motion, *Annals of Biomedical Engineering* **24**: 48–57.

Greenberg, S., McQueen, D. M. and Peskin, C. S. (1987). Three-dimensional fluid dynamics in a two-dimensional amount of central memory, *in* A. J. Chorin and A. J. Majda (eds), *Wave Motion: Theory, Modelling and Computation. Proceedings of a Conference in Honor of the 60th Birthday of Peter D. Lax.*, Springer-Verlag, New York, pp. 85–146.

Groen, J. P. and Dijk, P. v. (1987). Design of flow adjustable gradient waveforms, *in* J. T. E. d. Kleef (ed.), *Society of Magnetic Resonance in Medicine, 6th annual meeting*, p. 868.

Guyton, A. C. (1991). *Textbook of Medical Physiology*, 8th edn, W.B. Saunders Company, Philadelphia, USA.

Houlind, K. (2001a). Private communication.

Houlind, K. (2001b). *Early diastolic left ventricular blood flow patterns. Assements by magnetic resonance velocity mapping.*, PhD thesis, Dept. of Cardiothoracic and Vascular Surgery T, Aarhus University Hospital.

Houlind, K., Pedersen, E. M., Oyre, S., Kim, W. Y., Walker, P. G., Egeblad, H. and Yoganathan, A. P. (1994). Left ventricular blood flow patterns assessed by magnetic resonance velocity mapping in patients with ischemic heart disease, *Am. J. of Noninvas. Cardiol.* **8**: 317–325.

Houlind, K., Schroeder, A. P., Egeblad, H. and Pedersen, E. M. (1999). Age-dependent changes in spatial and temporal blood velocity distribution of early left ventricular filling, *Magnetic Resonance Imaging* **17**(6): 859–868.

Houlind, K., Schroeder, A. P., Stødkilde-Jørgensen, H., Paulsen, P. K., Egeblad, H. and Pedersen, E. M. (2001). Intraventricular dispersion and temporal delay of early left ventricular filling after acute myocardial infarction. Assesment by magnetic resonance velocity mapping, *in* Houlind (2001b).

Jacobsen, J. M. (1999). Peskin's 2D model of a section of the left side of the heart: Description, Investigation and Modification. Unpublished report.

Jacobsen, J. M., Adeler, P. T., Kim, W. Y., Houlind, K., Pedersen, E. M. and Larsen, J. (2001). Evaluation of a 2D model of the left side of a human heart against magnetic resonance velocity mapping, *Cardiovascular Engineering* **1**(2): 59–76.

Jakobsen, B. and Niss, K. (2000). Behandling af impuls ved kilder og dræn i C. S. Peskins 2D-hjertemodel (in Danish), *Technical Report , Tekst Nr 388*, Roskilde University.

Jones, T. N. and Metaxas, D. N. (1998). Patient-specific analysis of left ventricular blood flow, *in* W. M. Wells, A. Colchester and S. Delp (eds), *Medical Image Computing and Compuer-Assisted Intervention – MICCAI '98. Proceedings.*, Vol. 1498 of *Lecture Notes in Computer Science*, Springer Verlag, pp. 156–166.

Kim, W. Y., Walker, P. G., Pedersen, E. M., Poulsen, J. K., Oyre, S., Houlind, K. and Yoganathan, A. P. (1995). Left ventricular blood flow patterns in normal subjects: A quantitative analysis by three-dimensional magnetic resonance velocity mapping, *J. Am. Coll. Cardiol.* **26**(1): 224–238.

Kim, Y. H. (2001). Private communication.

Lai, M.-C. and Peskin, C. S. (2000). An immersed boundary method with formal second order accuracy and reduced numerical viscosity, *J. Comput. Phys.* **160**: 705–719.

Lemmon, J. D. and Yoganathan, A. P. (1998). Three-dimensional cardiac models with fluid-structure interaction : Application of the immersed boundary method at physiologic Reynolds numbers, *ASME, Bioengineering Division (Publication) BED* **39**: 73–74.

Lemmon, J. D. and Yoganathan, A. P. (2000a). Computational modeling of left heart diastolic function: Examination of ventricular dysfunction, *Journal of Biomechanical Engineering* **122**(4): 297–303.

Lemmon, J. D. and Yoganathan, A. P. (2000b). Three-dimensional computational model of left heart diastolic function with fluid-structure interaction, *Journal of Biomechanical Engineering* **122**(2): 109–117.

Mayo, A. A. and Peskin, C. S. (1993). An implicit numerical method for fluid dynamics problems with immersed elastic boundaries, *in* A. Y. Cheer and C. P. van Dam (eds), *Fluid Dynamics in Biology*, Vol. 141, American Mathematical Society, Providence, Rhode Island, pp. 261–277.

McCracken, M. F. and Peskin, C. S. (1980). A vortex method for blood flow through heart valves, *J. Comput. Phys.* **35**: 183–205.

McQueen, D. M. and Peskin, C. S. (1983). Computer-assisted design of pivoting disc prosthetic mitral valves, *Journal of Thoracic and Cardiovascular Surgery* **86**: 126–135.

McQueen, D. M. and Peskin, C. S. (1985). Computer-assisted design og butterfly bileaflet valves for the mitral position, *Scand. J. Thor. Cardiovasc. Surg.* **19**(2): 139–148.

McQueen, D. M. and Peskin, C. S. (1989). A three-dimensional computational method for blood flow in the heart. II. Contractile Fibers, *J. Comput. Phys.* **89**: 289–297.

McQueen, D. M. and Peskin, C. S. (1997). Shared-memory parallel vector implementation of the immersed boundary method for the computation of blood flow in the beating mammalian heart, *Journal of Supercomputing* **11**(3): 213–236.

McQueen, D. M. and Peskin, C. S. (2000). Heart simulation by an immersed boundary method with formal second-order accuracy and reduced numerical viscosity, *Proceedings of ICTAM 2000*, Kluwer Academic Publishers. To appear.

McQueen, D. M., Peskin, C. S. and Yellin, E. E. (1982). Fluid dynamics of the mitral valve: Physiological aspects of a mathematical model, *Am. J. Physiol.* **242**: H1095–H1110.

Meisner, J. S., McQueen, D. M., Ishida, Y., Vetter, H. O., Bortolotti, U., Strom, J. A., Frater, R. W. M., Peskin, C. S. and Yellin, E. L. (1985). Effects of timing of atrial systole on LV filling and mitral valve closure: computer and dog studies, *Am. J. Physiol.* **249**: H604–H619.

Netter, F. H. (1991). *Heart*, Vol. 5 of *The Ciba Collection of Medical Illustrations*, CIBA.

Nishihara, K., Mikami, T., Takatsuji, H., Onozuka, H., Saito, N., Yamada, S., Urasawa, K. and Kitabatake, A. (2000). Usefulness of early diastolic flow propagation velocity measured by color M-mode Doppler technique for the assesment of left ventricular diastolic function in patients with hypertrophic cardiomyopathy, *J. Am. Soc. Echocardiogr.* **13**: 801–808.

Noordergraaf, A. (1978). *Circulatory System Dynamics*, Academic Press, San Diego.

Ohte, N., Narita, H., Hashimoto, T., Hayano, J., Akita, S. and Kurokawa, K. (1999). Differentiation of abnormal relaxation pattern with aging from abnormal relaxation pattern with coronary artery disease in transmitral flow with the use of tissue Doppler imaging of the mitral annulus, *J. Am. Soc. Echocardiogr.* **12**: 629–635.

Olufsen, M., Adeler, P. T., Danielsen, M. and Larsen, J. (2001). Cardiovascular and pulmonary physiology and anatomy, *in* J. T. Ottesen, M. S. Olufsen and J. Larsen (eds), *Applied Mathematical Models in Human Physiology*, to be published by SIAM, chapter 2.

Park, J., Metaxas, D. N. and Axel, L. (1996). Analysis of left ventricular wall motion based on volumetric deformable models and mri spamm, *Medical Image Analysis* **1**(1): 53–71.

Peskin, C. S. (1972a). *Flow Patterns around Heart Valves*, PhD thesis, Albert Einstein College of Medicine.

Peskin, C. S. (1972b). Flow patterns around heart valves: A numerical method, *J. Comput. Phys.* **10**: 252–271.

Peskin, C. S. (1975). Mathematical aspects of heart physiology, Courant Institute of Mathematical Sciences, New York University, Lecture Notes.

Peskin, C. S. (1977). Numerical analysis of blood flow in the heart, *J. Comput. Phys.* **25**: 220–252.

Peskin, C. S. (1981). Mathematical aspects of physiology, *in* F. C. Hoppensteadt (ed.), *Mathematical Aspects of Physiology. Lectures in Applied Mathematics, Vol. 19*, American Mathematical Society, Providence, Rhode Island, pp. 69–93.

Peskin, C. S. (1989). Fiber architecture of the left ventricular wall: An asymptotic analysis, *Commun. Pure Appl. Math.* **XLII**: 79–113.

Peskin, C. S. (1998). Incompressible fluid dynamics with distributed sources and sinks. Unpublished note.

Peskin, C. S. (2001). Private communication.

Peskin, C. S. and McQueen, D. M. (1980). Modeling prosthetic heart valves for numerical analysis of blood flow in the heart, *J. Comput. Phys.* **37**: 113–132.

Peskin, C. S. and McQueen, D. M. (1989). A Three-Dimensional computational method for blood flow in the heart, *J. Comput. Phys.* **81**: 372–405.

Peskin, C. S. and McQueen, D. M. (1992). Cardiac fluid dynamics, *Critical Reviews in Biomedical Engineering* **20**(5,6): 451–459.

Peskin, C. S. and McQueen, D. M. (1993a). Cardiac fluid dynamics, *in* T. C. Pilkington et al. (ed.), *High-performance Computing in Biomedical Research*, CRC Press.

Peskin, C. S. and McQueen, D. M. (1993b). Computational biofluid dynamics, *in* A. Y. Cheer and C. P. van Dam (eds), *Fluid Dynamics in Biology*, Vol. 141, American Mathematical Society, Providence, Rhode Island, pp. 161–186.

Peskin, C. S. and McQueen, D. M. (1994). Mechanical equilibrium determines the fractal fiber architecture of aortic heart valve leaflets, *Am. J. Physiol.* **266**: H319–H328.

Peskin, C. S. and McQueen, D. M. (1995). A general method for the computer simulation of biological systems interacting with fluids, *in* C. P. Ellington and T. J. Pedley (eds), *Biological Fluid Dynamics: Proceedings of a meeting held at the University of Leeds, UK, 4-8 July 1994*, Vol. 49 of *Symposia of the Society for Experimental Biology*, Cambridge, UK, pp. 265–276.

Peskin, C. S. and McQueen, D. M. (1996). Fluid dynamics of the heart and its valves, *in* H. Othmer, F. R. Adler, M. A. Lewis and J. C. Dallon (eds), *Case Studies in Mathematical Modeling - Ecology, Physiology, and Cell Biology*, Prentice-Hall, Inc., Englewood Cliffs, New Jersey, chapter 14, pp. 309–337.

Peskin, C. S. and Printz, B. F. (1993). Improved volume conservation in the computation of flows with immersed boundaries, *J. Comput. Phys.* **105**: 33–46.

Philips (n.d.). *Basic Principles of MR Imaging*, Philips Medical System.

Rideout, V. (1991). *Mathematical and Computer Modeling of Physiological Systems*, Prentice Hall, Biophysics and Bioengineering Series.

Saber, N. R., Gosman, A. D., Wood, N. B., Kilner, P. J., Charrier, C. L. and Firmin, D. N. (2001). Computational flow modeling of the left ventricle based on in vivo MRI data: Initial experience, *Annals of Bimedical Engineering* **29**(4): 275–283.

Schlaikjer, M. and Kolenda, T. (1997). MRI, den grundlggende teori (in Danish), *Student report*, Technical University of Denmark. Unpublished.

Schoephoerster, R. T., Silva, C. L. and Ray, G. (1993). Finite analytic model for left ventricular systolic flow dynamics, *Journal of Engineering Mechanics* **119**(4): 733–747.

Schoephoerster, R. T., Silva, C. L. and Ray, G. (1994). Evaluation of left ventricular function based on simulated systolic flow dynamics computed from regional wall motion, *J. Biomechanics* **27**(2): 125–136.

Schroeder, A. P. (1999). *Magnetic resonance imaging for the study of left ventricular remodeling after acute myocardial infarction*, PhD thesis, Department of Cardiology, Skejby Hospital, University of Aarhus.

St. Goar, F. G., Masuyama, T., Alderman, E. L. and Popp, R. L. (1991). Left ventricular diastolic dysfunction in end-stage dilated cardiomyopathy: Simultaneous Doppler echocardiography and hemodynamic evaluation, *J. Am. Soc. Echocardiogr.* **4**: 349–360.

Steine, K., Stugaard, M. and Smiseth, O. (1999). Mechnisms of retarded apical filling in acute ischemic left ventricular failure, *Circulation* **99**: 2048–2054.

Stockie, J. M. and Wetton, B. T. R. (1995). Stability analysis for the immersed fiber problem, *SIAM J. Appl. Math.* **55**(6): 1577–1591.

Streeter, Jr., D. D., Powers, W. E., Ross, M. A. and Torrent-Guasp, F. (1978). Three-dimensional fiber orientation in the mammalian left ventricle wall, *in* J. Baan, A. Noordergraaf and J. Raines (eds), *Cardiovascular System Dynamics*, MIT Press, Cambridge, MA, pp. 73–84.

Streeter, Jr., D. D., Spotniz, H. M., Patel, D. P., Ross, Jr., J. and Sonnenblick, E. H. (1969). Fiber orientation in the canine left ventricle during diastole and systole, *Circ. Res.* **24**: 339–347.

Stugaard, M., Brodahl, U., Torp, H. and Ihlen, H. (1994a). Abnormalities of left ventricular filling in patients with coronary artery disease: assesment by colour M-mode Doppler technique, *European Heart Journal* **15**: 318–327.

Stugaard, M., Risöe, C., Ihlen, H. and Smiseth, O. (1994b). Intracavitary filling pattern in the failing left ventricle assesed by color M-mode Doppler echocardiography, *J. Am. Coll. Cardiol.* **24**: 663–670.

Stugaard, M., Smiseth, O. A., Risöe, C. and Ihlen, H. (1993). Intraventricular early diastolic filling during acute myocardial infarction, *Circulation* **88**: 2705–2713.

Taylor, T. W., Okino, H. and Yamaguchi, T. (1993). The effects of supravalvular aortic stenosis on realistic three-dimensional left ventricular blood ejection, *Biorheology* **30**(5–6): 429–434.

Taylor, T. W., Suga, H., Goto, Y., Okino, H. and Yamaguchi, T. (1996). The effects of cardiac infarction on realistic three-dimensional left ventricular blood ejection, *J. Biomech. Eng.* **118**(1): 106–110.

Taylor, T. W. and Yamaguchi, T. (1995a). Flow patterns in three-dimensional left ventricular systolic and diastolic flows determined from computational fluid dynamics, *Biorheology* **32**(1): 61–71.

Taylor, T. W. and Yamaguchi, T. (1995b). Realistic three-dimensional left ventricular ejection determined from computational fluid dynamics, *Med. Eng. Phys.* **17**(8): 602–608.

Thomas, C. E. (1957). The muscular architecture of the ventricles of hog and dog hearts, *The American Journal of Anatomy* **101**: 17–57.

Thorup, P. (1997). *Hemodynamic Modelling of the Heart*, Master's thesis, Dept. of Hydrodynamics and Water Resources (ISVA), Technical University of Denmark (DTU).

Tortora, G. J. (1999). *Principles of Human Anatomy*, 8th edn, Addison Wesley Longman, Inc., Menlo Park, California.

Tu, C. and Peskin, C. S. (1992). Stability and instability in the computation of flows with moving immersed boundaries: A comparison of three methods, *SIAM J. Sci. Stat. Comput.* **13**(6): 1462–1376.

Vesier, C. C. and Yoganathan, A. P. (1992). A computer method for simulation of cardiovascular flow fields: validation of approach, *J. Comput. Phys.* **99**(2): 271–287.

Walker, P. G., Cranney, G. B., Grimes, R. Y., Delatore, J., Rectenwald, J., Pohost, G. M. and Yoganathan, A. P. (1996). Three-dimensional reconstruction of the flow in a human left heart by using magnetic resonance phase velocity encoding, *Annals of Biomedical Engineering* **24**(1): 139–147.

Walker, P. G., Cranney, G. B., Scheidegger, M. B., Waseleski, G., Pohost, G. M. and Yoganathan, A. P. (1993). Semi-automated method for noise reduction and background phase error reduction of MR phase velocity data, *J. Magn. Reson. Imaging* **3**: 521–530.

Weiss, J. L., Frederiksen, J. W. and Weisfeldt, M. L. (1976). Hemodynamic determinants of the time-coruse of fall in canine left ventricular pressure, *Journal of Clinical Investigation* **58**: 751–760.

Yamamoto, K., Masuyama, T., Tanouchi, J., Naito, J., Mano, T., Kondo, H., Nagano, R., Masatsugu and Kamada, T. (1995). Intraventricular dispersion of early diastolic filling: A new marker of left ventricular diastolic dysfunction, *Am. Heart. J.* **129**: 291–299.

Yellin, E. L., Peskin, C. S., Yoran, C., Koenigsberg, M., Matsumoto, M., Laniado, S., McQueen, D. M., Shore, D. and Frater, R. W. M. (1981). Mechanisms of mitral valve motion during diastole, *Am. J. Physiol.* **241**(3): H389–H400.

Yoganathan, A. P., Lemmon, J. D., Kim, Y. H., Levine, R. A. and Vesier, C. C. (1995). A three-dimensional computer investigation of intraventricular fluid dynamics: Examination into the initiation of systolic anterior motion of the mitral valve leaflets, *J. Biomech. Eng.* **117**: 94–102.

Yoganathan, A. P., Lemmon, J. D., Kim, Y. H., Walker, P. G., Levine, R. A. and Vesier, C. C. (1994). A computational study of a thin-walled three-dimensional left ventricle during early systole, *J. Biomech. Eng.* **116**: 307–314.

Ph. D. theses from IMM

1. **Larsen, Rasmus.** (1994). *Estimation of visual motion in image sequences. xiv* + 143 pp.
2. **Rygard, Jens Moberg.** (1994). *Design and optimization of flexible manufacturing systems. xiii* + 232 pp.
3. **Lassen, Niels Christian Krieger.** (1994). *Automated determination of crystal orientations from electron backscattering patterns. xv* + 136 pp.
4. **Melgaard, Henrik.** (1994). *Identification of physical models. xvii* + 246 pp.
5. **Wang, Chunyan.** (1994). *Stochastic differential equations and a biological system. xxii* + 153 pp.
6. **Nielsen, Allan Aasbjerg.** (1994). *Analysis of regularly and irregularly sampled spatial, multivariate, and multi-temporal data. xxiv* + 213 pp.
7. **Ersbøll, Annette Kjær.** (1994). *On the spatial and temporal correlations in experimentation with agricultural applications. xviii* + 345 pp.
8. **Møller, Dorte.** (1994). *Methods for analysis and design of heterogeneous telecommunication networks.* Volume 1-2, *xxxviii* + 282 pp., 283-569 pp.
9. **Jensen, Jens Christian.** (1995). *Teoretiske og eksperimentelle dynamiske undersøgelser af jernbanekøretøjer. viii* + 174 pp.
10. **Kuhlmann, Lionel.** (1995). *On automatic visual inspection of reflective surfaces.* Volume 1, *xviii* + 220 pp., (Volume 2, *vi* + 54 pp., fortrolig).
11. **Lazarides, Nikolaos.** (1995). *Nonlinearity in superconductivity and Josephson Junctions. iv* + 154 pp.
12. **Rostgaard, Morten.** (1995). *Modelling, estimation and control of fast sampled dynamical systems. xiv* + 348 pp.
13. **Schultz, Nette.** (1995). *Segmentation and classification of biological objects. xiv* + 194 pp.
14. **Jørgensen, Michael Finn.** (1995). *Nonlinear Hamiltonian systems. xiv* + 120 pp.

15. **Balle, Susanne M.** (1995). *Distributed-memory matrix computations. iii* + 101 pp.

16. **Kohl, Niklas.** (1995). *Exact methods for time constrained routing and related scheduling problems. xviii* + 234 pp.

17. **Rogon, Thomas.** (1995). *Porous media: Analysis, reconstruction and percolation. xiv* + 165 pp.

18. **Andersen, Allan Theodor.** (1995). *Modelling of packet traffic with matrix analytic methods. xvi* + 242 pp.

19. **Hesthaven, Jan.** (1995). *Numerical studies of unsteady coherent structures and transport in two-dimensional flows.* Risø-R-835(EN) 203 pp.

20. **Slivsgaard, Eva Charlotte.** (l995). *On the interaction between wheels and rails in railway dynamics. viii* + 196 pp.

21. **Hartelius, Karsten.** (1996). *Analysis of irregularly distributed points. xvi* + 260 pp.

22. **Hansen, Anca Daniela.** (1996). *Predictive control and identification - Applications to steering dynamics. xviii* + 307 pp.

23. **Sadegh, Payman.** (1996). *Experiment design and optimization in complex systems. xiv* + 162 pp.

24. **Skands, Ulrik.** (1996). *Quantitative methods for the analysis of electron microscope images. xvi* + 198 pp.

25. **Bro-Nielsen, Morten.** (1996). *Medical image registration and surgery simulation. xxvii* + 274 pp.

26. **Bendtsen, Claus.** (1996). *Parallel numerical algorithms for the solution of systems of ordinary differential equations. viii* + 79 pp.

27. **Lauritsen, Morten Bach.** (1997). *Delta-domain predictive control and identification for control. xxii* + 292 pp.

28. **Bischoff, Svend.** (1997). *Modelling colliding-pulse mode-locked semiconductor lasers. xxii* + 217 pp.

29. **Arnbjerg-Nielsen, Karsten.** (1997). *Statistical analysis of urban hydrology with special emphasis on rainfall modelling.* Institut for Miljøteknik, DTU. *xiv* + 161 pp.

30. **Jacobsen, Judith L.** (1997). *Dynamic modelling of processes in rivers affected by precipitation runoff. xix* + 213 pp.

31. **Sommer, Helle Mølgaard.** (1997). *Variability in microbiological degradation experiments - Analysis and case study. xiv* + 211 pp.

32. **Ma, Xin.** (1997). *Adaptive extremum control and wind turbine control. xix* + 293 pp.

33. **Rasmussen, Kim Ørskov.** (1997). *Nonlinear and stochastic dynamics of coherent structures. x* + 215 pp.

34. **Hansen, Lars Henrik.** (1997). *Stochastic modelling of central heating systems. xxii* + 301 pp.

35. **Jørgensen, Claus.** (1997). *Driftsoptimering på kraftvarmesystemer.* 290 pp.

36. **Stauning, Ole.** (1997). *Automatic validation of numerical solutions. viii* + 116 pp.

37. **Pedersen, Morten With.** (1997). *Optimization of recurrent neural networks for time series modeling. x* + 322 pp.

38. **Thorsen, Rune.** (1997). *Restoration of hand function in tetraplegics using myoelectrically controlled functional electrical stimulation of the controlling muscle. x* + 154 pp. + Appendix.

39. **Rosholm, Anders.** (1997). *Statistical methods for segmentation and classification of images. xvi* + 183 pp.

40. **Petersen, Kim Tilgaard.** (1997). *Estimation of speech quality in telecommunication systems. x* + 259 pp.

41. **Jensen, Carsten Nordstrøm.** (1997). *Nonlinear systems with discrete and continuous elements.* 195 pp.

42. **Hansen, Peter S.K.** (1997). *Signal subspace methods for speech enhancement. x* + 226 pp.

43. **Nielsen, Ole Møller.** (1998). *Wavelets in scientific computing. xiv* + 232 pp.

44. **Kjems, Ulrik.** (1998). *Bayesian signal processing and interpretation of brain scans. iv* + 129 pp.

45. **Hansen, Michael Pilegaard.** (1998). *Metaheuristics for multiple objective combinatorial optimization.* *x* + 163 pp.

46. **Riis, Søren Kamaric.** (1998). *Hidden markov models and neural networks for speech recognition.* *x* + 223 pp.

47. **Mørch, Niels Jacob Sand.** (1998). *A multivariate approach to functional neuro modeling.* *xvi* + 147 pp.

48. **Frydendal, Ib.** (1998.) *Quality inspection of sugar beets using vision.* *iv* + 97 pp. + app.

49. **Lundin, Lars Kristian.** (1998). *Parallel computation of rotating flows.* *viii* + 106 pp.

50. **Borges, Pedro.** (1998). *Multicriteria planning and optimization. - Heuristic approaches.* *xiv* + 219 pp.

51. **Nielsen, Jakob Birkedal.** (1998). *New developments in the theory of wheel/rail contact mechanics.* *xviii* + 223 pp.

52. **Fog, Torben.** (1998). *Condition monitoring and fault diagnosis in marine diesel engines.* *xii* + 178 pp.

53. **Knudsen, Ole.** (1998). *Industrial vision.* *xii* + 129 pp.

54. **Andersen, Jens Strodl.** (1998). *Statistical analysis of biotests. - Applied to complex polluted samples.* *xx* + 207 pp.

55. **Philipsen, Peter Alshede.** (1998). *Reconstruction and restoration of PET images.* *vi* + 132 pp.

56. **Thygesen, Uffe Høgsbro.** (1998). *Robust performance and dissipation of stochastic control systems.* 185 pp.

57. **Hintz-Madsen, Mads.** (1998). *A probabilistic framework for classification of dermatoscopic images.* *xi* + 153 pp.

58. **Schramm-Nielsen, Karina.** (1998). *Environmental reference materials methods and case studies.* *xxvi* + 261 pp.

59. **Skyggebjerg, Ole.** (1999). *Acquisition and analysis of complex dynamic intra- and intercellular signaling events.* 83 pp.

60. **Jensen, Kåre Jean.** (1999). *Signal processing for distribution network monitoring.* *xv* + 199 pp.

61. **Folm-Hansen, Jørgen.** (1999). *On chromatic and geometrical calibration.* *xiv* + 238 pp.

62. **Larsen, Jesper.** (1999). *Parallelization of the vehicle routing problem with time windows.xx* + 266 pp.

63. **Clausen, Carl Balslev.** (1999). *Spatial solitons in quasi-phase matched struktures.* *vi* + (flere pag.)

64. **Kvist, Trine.** (1999). *Statistical modelling of fish stocks.* *xiv* + 173 pp.

65. **Andresen, Per Rønsholt.** (1999). *Surface-bounded growth modeling applied to human mandibles.* *xxii* + 125 pp.

66. **Sørensen, Per Settergren.** (1999). *Spatial distribution maps for benthic communities.*

67. **Andersen, Helle.** (1999). *Statistical models for standardized toxicity studies.* *viii* + (flere pag.)

68. **Andersen, Lars Nonboe.** (1999). *Signal processing in the dolphin sonar system.* *xii* + 214 pp.

69. **Bechmann, Henrik.** (1999). *Modelling of wastewater systems.* *xviii* + 161 pp.

70. **Nielsen, Henrik Aalborg.** (1999). *Parametric and non-parametric system modelling.* *xviii* + 209 pp.

71. **Gramkow, Claus.** (1999). *2D and 3D object measurement for control and quality assurance in the industry.* *xxvi* + 236 pp.

72. **Nielsen, Jan Nygaard.** (1999). *Stochastic modelling of dynamic systems.* *xvi* + 225 pp.

73. **Larsen, Allan.** (2000). *The dynamic vehicle routing problem.* *xvi* + 185 pp.

74. **Halkjær, Søren.** (2000). *Elastic wave propagation in anisotropic inhomogeneous materials.* *xiv* + 133 pp.

75. **Larsen, Theis Leth.** (2000). *Phosphorus diffusion in float zone silicon crystal growth. viii* + 119 pp.

76. **Dirscherl, Kai.** (2000). *Online correction of scanning probe microscopes with pixel accuracy.* 146 pp.

77. **Fisker, Rune.** (2000). *Making deformable template models operational. xx* + 217 pp.

78. **Hultberg, Tim Helge.** (2000).*Topics in computational linear optimization. xiv* + 180 pp.

79. **Andersen, Klaus Kaae.** (2000).*Stochastic modelling of energy systems. xiv* + 191 pp.

80. **Thyregod, Peter.** (2001). *Modelling and monitoring in injection molding. xvi* + 132 pp.

81. **Schjødt-Eriksen, Jens.** (2001). *Arresting of collapse in inhomogeneous and ultrafast Kerr media.*

82. **Bennetsen, Jens Christian.** (2000). *Numerical simulation of turbulent airflow in livestock buildings. xi* + 205 pp + Appendix.

83. **Højen-Sørensen, Pedro A.d.F.R.** (2001). *Approximating methods for intractable probabilistic models: - Applications in neuroscience. xi* + 104 pp + Appendix.

84. **Nielsen, Torben Skov.** (2001). *On-line prediction and control in nonlinear stochastic systems. xviii* + 242 pp.

85. **Öjelund, Henrik.** (2001). *Multivariate calibration of chemical sensors. xviii* + 184 pp.

86. **Adeler, Pernille Thorup.** (2001). *Hemodynamic simulation of the heart using a 2D model and MR data. xv* + 179 pp.